Controlling surface segregation and tuning silver ion release of reactively sputtered Ag/TiO_x nanocomposites

Dissertation
zur Erlangung des akademischen Grades
Doktor der Ingenieurwissenschaften
(Dr.-Ing.)
der Technischen Fakultät
der Christian-Albrechts-Universität zu Kiel

Jian Xiong

Kiel, Germany

2014

Supervisor	Prof. Dr. Franz Faupel
Second reviewer	Prof. Dr. Lorenz Kienle
Date of oral examination	08. July 2014

致我亲爱的家人和爱人

To my family & Luying He

Who have given me their love & support throughout my life

Abstract

Reactively sputtered Ag/TiO_x nanocomposite coatings show high potential for antibacterial applications. However, previous studies on such coatings showed unavoidable segregation of silver out to the surface, which results in direct exposure of the potentially harmful Ag nanoparticles (NPs) to the environment and could also lead to a rapid depletion of the Ag source. Moreover, potentially harmful silver NPs are directly exposed to the environment without encapsulation. Tailoring the silver ion release is thus highly promising for enhancing the antibacterial applications of reactively sputtered Ag/TiO_x coatings.

The present work is concerned with the influence of sputter parameters on the surface morphology and silver ion release properties of reactively sputtered Ag/TiO_x nanocomposite coatings. Since surface segregation of silver in such nanocomposites has not been investigated systematically, here we show under which conditions of the reactive sputtering process silver surface segregation occurs and how it can be controlled to obtain Ag/TiO_x nanocomposites with a defined morphology. Silver NPs were embedded in or coated on TiO_x thin films for 3D and 2D system purposes. Titanium oxide is known for its biocompatibility, transparency, low coat and good dielectric properties. DC reactive magnetron sputtering is selected because it not only provides controllable structures, sizes and morphologies, and allows formation of films with controllable stoichiometry, but it is also straightforward to implement in industrial-scale production with relatively high deposition rates and large area coatings.

A series of titanium oxide thin films containing different silver filling factors were synthesized by a DC reactive magnetron co-sputtering method at different total pressure and oxygen conditions. The aim was to minimize Ag oxidation in conjunction with controlled surface segregation. We present an investigation about the influence of total pressure, silver filling factor, and titanium oxide barriers on the surface morphology evolution. Furthermore, the relation between the morphology of the nanocomposites and their optical properties is presented. To gain additional

insight into the role that oxygen and plasma conditions played in silver surface segregation, 2D layer-by-layer structures were deposited and the silver surface segregation behavior was investigated by x-ray photoelectron spectroscopy (XPS) as well. The potential of silver ion release is studied by immersion samples in water for several different periods of time. Atomic absorption spectroscopy (AAS) is used to measure the concentration of silver ion in water. Different approaches to tailor the silver ion release are studied in this work. Tuning silver ion release by varying the total gas pressure, oxygen flow rate, silver concentration, barrier deposition rate and barrier thickness is presented. In addition, the kinetics of silver ion release in Ag/TiO_x nanocomposites is discussed as well.

Declaration of authenticity

I, the undersigned, **Jian Xiong**, declare that this dissertation is my original work, gathered and utilized especially to fulfill the purposes and objectives of this study, and has not been previously submitted, in whole or in part, to any other university for any academic degree. Except where otherwise indicated, this thesis is my own work.

Signature

Place and date

Declaration of co-authorship and co-contribution: Papers and publications incorporated in thesis

I, **Jian Xiong**, declare here the nature of my contribution to the work in the following publications:

1. Paper entitled, ' *Controlling surface segregation of reactively sputtered Ag/TiO_x nanocomposites* ', **Jian Xiong**, Muhammad Zubair Ghori, Bodo Henkel, Thomas Strunskus, Ulrich Schürmann, Lorenz Kienle, Franz Faupel, reused in Chapter 4 with permission from (Acta Materialia **74** : 1-8), copyright (2014), Elsevier.

I prepared all the samples, performed the characterization measurements using SEM, XRD, UV-Vis, XPS, sample preparation for TEM, all data analysis, figures, and wrote most of the text as a first author.

2. Paper entitled, ' *Tuning silver ion release properties in reactively sputtered Ag/TiO_x nanocomposites* ', **Jian Xiong**, Muhammad Zubair Ghori, Bodo Henkel, Thomas Strunskus, Ulrich Schürmann, Mao Deng, Lorenz Kienle, Franz Faupel, submitted to , used in Chapter 5.

I prepared all the samples, performed the characterization measurements using SEM, XRD, UV-Vis, XPS, and AAS, sample preparation for TEM, all data analysis, figures, and wrote most of the text as a first author.

3. Paper entitled, ' *A critical evaluation of the 0-3 approach for magnetoelectric nanocomposites with metallic nanoparticles* ', Gojdka, B.; Hrkac, V.; **Xiong, J**.; Gerken, M.; Kienle, L.; Strunskus, T.; Zaporojtchenko, V.; Faupel, F, Journal of Applied Physics Vol. 112 Issue 4 (2012) 044303.

I measured the SEM/EDX for samples and helped in writing the results and discussion part.

4. Paper entitled, ' *Highly versatile concept for precise tailoring of nanogranular composites with a gas aggregation cluster source* ', Gojdka, B.; Zaporojtchenko, V.; Hrkac, V.; **Xiong, J**.; Kienle, L.; Strunskus, T.; Faupel, F, Applied Physics Letters Vol. 100 Issue 13 (2012) 133104.

I measured the SEM/EDX for samples and helped in writing the results and discussion part.

Acknowledgments

I would like to express my sincere thanks to Prof. Dr. Franz Faupel for giving me the opportunity to work here and to do my doctorate research under his kind guidance. I thank him profusely for his sympathetic attitude towards my work and personal matters. I have had a very nice experience here in the past three years and it is a great pleasure to be a member of his group.

I am deeply thankful to Dr. Vladimir Zaporojtchenko who passed away in August 2012, for his guidance at all stages of my work. He was a brilliant scientist and always shared his ideas and experience with me. I could not have started and finished my PhD work without his encouragement and instructions. I will miss him forever.

I express my heartfelt gratitude to Dr. Thomas Strunskus for supervising me and for our fruitful discussions when I had problems. When things went wrong, I could ask him for help. I still remember the day that Thomas waited together with me for my landlord when I had just arrived in Kiel and had nothing but fear of a new environment. His kind help let me feel comfortable and gave me a good impression of Kiel.

I am also very grateful to Prof. Dr. Klaus Rätzke for his wise counsel, whether in professional or private matters. I will never forget the course about thin films he gave me in the first year I came here.

Special thanks to Dipl.-Ing. Stefan Rehders for his technical assistance during my PhD work. In addition, I am also very thankful to Christoph Ochmann for his kind help in solving technical problems. Besides, I would like to thank Rainer Kloth and Peter Sommer for their distinct computer skills. I wish all the best for Rainer's recovery.

The TEM studies presented in this work were conducted by Prof. Dr. Lorenz Kienle and Dr. Ulrich Schürmann and I would like to thank them for their support.

Many thanks to Ralf Abel and Frank Lehmann who are working at Universitätsklinikum Schleswig-Holstein for helping me to do the AAS measurements in this work.

I am also very grateful to Muhammad Zubair Ghori for his support in my experimental work and the very nice and pleasant cooperation between us. I wish him all the best in his PhD position search and further academic work.

I am extremely thankful to my colleagues (Tommi Hrkac, Björn Gojdka, Tilo Peter, Christina Pakula, Kerstin Meurisch, Amit Kulkarni, Bodo Henkel, Nisreen Alissawi, Sri Wahyuni Basuki, Christian Ohrt, Tönjes Koschine, Viktor Schneider, Dr. Oleksandr Polonskyi, Amir Mohammad Ahadi, Sebastian Zabel, Alexander Hinz, Xin Jin, Mao Deng and others) in the chair for Multicomponent materials and Faculty of Engineering. My special thanks to Bodo Henkel for all his help and encouragement in my experiments and daily life in Kiel, I hope we can meet in China one day in the future.

Part of this work was funded by the German Federal Ministry of Education and Research (BMBF) through project #03X0083E "Nanopurification". I kindly acknowledge the financial support for me by the China Scholarship Council (CSC).

Finally, I would like to give my very special thanks to my wife and my family. I am very obliged to my wife for her overwhelming support and encouragement during my life in Kiel. She is wonderful and makes my life colorful and full of happiness. I am so proud to be my mom's son and a younger brother to my sister; I am so thankful for their endless love and care. I love them so much.

Jian Xiong

May 2014

Kiel

List of initials and acronyms

2D	Two dimensional
3D	Three dimensional
AAS	Atomic Absorption spectroscopy
Abs.	Absorbance
Ag	Silver
Ag^+	Silver ion
Ag NPs	Silver nanoparticles
DC	Direct current
DI	Deionized
FCC	Face-centered cubic
NPs	Nanoparticles
PVD	Physical vapor deposition
QCM	Quartz crystal microbalance
RF	Radio frequency
ROS	Reactive oxygen species
sccm	Standard cubic centimeter per minute
SEM	Scanning electron microscopy
Si	Silicon
TEM	Transmission electron microscopy
UV-Vis	Ultraviolet-Visible light spectroscopy
XRD	X-ray Diffraction
XPS	X-ray photoelectron spectroscopy

Table of contents

Chapter 1

Introduction

Bacterial contamination on various surfaces of medical devices, wound dressings, and food packaging is of serious global concern, and poses great threat to device efficiency and lifetime [1]. Generally, bacteria adhere to these surfaces followed by growth under suitable environmental conditions to form so-called biofilms; the only effective way to remove the biofilm-induced contamination/infection is to discard the contaminated devices and replace with new ones, which is extremely inconvenient and costly. Therefore, it is highly desirable to design high-performance antibacterial materials which can strongly resist and kill bacteria.

Nanosilver is the most promising antibacterial material which has exhibited a much greater antibacterial effect compared to bulk silver material due to its large surface area and size/shape-dependent physicochemical properties [2]. Moreover, silver nanomaterials have a broad spectrum of antibacterial activity to kill a variety of bacteria existing in everyday life. However, it is still unclear how to fabricate silver-containing coatings with strong antibacterial effects and good biocompatibility and environmental safety. Aggregation of silver NPs, uncontrollable release of silver ions significantly reduce antibacterial effects of nanosilver [3]. Titanium oxide, with great durability and biocompatibility, has pronounced potential to retard silver aggregation and form homogeneous silver NP distribution in coatings on various substrates. Besides, silver/titanium oxide nanocomposites can also tune the release of silver ions for long-lasting antibacterial effects and reduce cytotoxicity. In addition, titanium oxide can serve as an antibacterial material even after all the silver NPs have been released. Therefore, it is profitable to combine silver NPs and a titanium oxide matrix

to form multifunctional composites for various applications. The applications of silver/titanium oxide nanocomposites as promising antibacterial materials have also been studied intensively, however, how the nanocomposite morphology (silver NP size, shape, distribution and concentration) affects the mechanism of silver ion release and the study of controlled silver ion release has not been investigated systematically.

Silver/titanium oxide nanocomposites can be synthesized with various approaches, such as chemical synthesis, ion implantation and magnetron sputtering [4–6]. Magnetron sputtering has been widely used due to its flexibility, its simplicity in combining materials, and its ability to tailor the size distribution. Considering the relatively low deposition rate and the complex production of titania targets used for RF magnetron sputtering, DC reactive sputtering from a metallic titanium target appears to be much more attractive. It not only provides controllable structures, sizes, and morphologies, and also allows formation of films with controllable stoichiometry, but it is also straightforward to implement in industrial-scale production where relative high deposition rates and large area coatings are required.

However, previous studies on silver/titanium oxide nanocomposite coatings have always showed strong segregation of silver towards the surface [7]. This would lead to abundant silver ion release in short time with the possibility of removal of silver NPs directly from the surface, preventing an exact tuning of the desired silver ion release properties. Moreover, the oxygen interaction with the silver NPs would cause formation of Ag_2O or AgO oxide layers, which should be avoided for many applications [8]. Considering these effects, preparing silver NPs in their metallic state and preventing segregation of silver at the surface will be the key point in the preparation of well-defined silver based nanocomposites.

Silver surface segregation is not only observed in magnetron sputtering preparation, but was also observed for silver/titania nanocomposites prepared in other ways. Yet, the factors influencing silver surface segregation in reactively sputtered nanocomposite thin films have not been investigated previously. In this work, a series of titanium oxide thin films containing different silver filling factors was synthesized by a DC reactive magnetron co-sputtering process at different total pressure and oxygen conditions. The aim was to minimize silver oxidation in conjunction with

controlling the surface segregation. An investigation on the influence of total pressure, silver filling factor, and titanium oxide barriers on the surface morphology evolution is presented. To gain additional insight into the role that oxygen and plasma conditions play in silver surface segregation, 2D layer-by-layer structures were deposited and the silver surface segregation behavior was investigated using X-ray photoelectron spectroscopy (XPS) as a surface sensitive method. It was observed that silver surface segregation depends on the silver filling factor of the composite and that it is largely independent of the oxygen partial pressure used in the sputtering process. At high total pressure, even sputtering of pure TiO_x barriers is - different from non-reactive sputtering of TiO_x - not sufficient to prevent the strong surface segregation effect. Surface segregation is only thoroughly suppressed by reduction of the total pressure during reactive sputtering, allowing the formation of a dense composite film. Based on this principle, silver surface segregation can be further reduced by deposition of TiO_x barriers with very high sputtering rates. Furthermore, the relation between the morphology of the nanocomposites and their optical properties is presented.

Additionally, silver ion release kinetics from 2D/3D nanocomposites consisting of different silver concentration was investigated. It was observed that the silver ion release rate has a strong relationship to the total pressure: the coatings prepared at lower pressure present a lower but long-lasting release behavior. The much dense structure produced under these conditions reduces the transport of water molecules into the coating. In addition, the influence of microstructure and thickness of titanium oxide barriers on the silver ion release were investigated intensively. Moreover, tailoring silver ion release for the coatings prepared at high total pressure was also developed; stable and long-lasting silver release can be achieved by depositing a barrier at a high rate. Nanocomposites produced under these conditions show a perfectly controllable silver ion release property for applications as antibacterial coatings.

Characterization of nanocomposites was performed in terms of the release of silver ions and the control of the surface segregation of the 2D/3D nanocomposite systems by using a combination of different analytical techniques such as Scanning

electron microscopy (SEM), Transmission electron microscopy (TEM), UV-visible spectroscopy (UV-Vis), X-ray photoelectron spectroscopy (XPS), X-ray diffraction (XRD) and atomic absorption spectroscopy (AAS). A strong correlation was found among the results obtained by the different techniques.

The dissertation is composed of six chapters. The first one gives an introduction to the subject of the silver/titanium oxide nanocomposite and the silver ion release process. Chapter two deals with the theories associated at various stages of this work. Chapter three presents the experimental set up and characterization techniques which were employed in this work. Chapter four demonstrates the synthesis of 2D/3D silver/titanium oxide nanocomposite thin films and the investigations on the surface segregation of nanocomposites. Chapter five shows the silver ion release properties of 2D/3D silver/titanium oxide nanocomposite thin films and the discussion about the kinetics of silver ion release. Finally, chapter six summarizes the whole work and gives an outlook for the future.

Chapter 2

Theory

2.1 Ag/TiO_x nanocomposite

Nanocomposite materials based on metal NPs (guest) in/on oxide matrices (host) have attracted great attention due to their intriguing chemical and physical properties, which can be tuned as a function of metal NP size, shape, distribution and mutual interactions [9]. As a matter of fact, the novel characteristics and functional performances of such nanocomposites are not only derived from interfacial metal NPs/matrix interactions, but also largely depend on the composition gradients, the presence of defects and roughness. In addition, the surface microstructure and chemical composition of metal NPs may result in an unstable state due to their high reactivity and energy, leading to undesired changes of the system properties such as segregation phenomenon on the surface. Therefore, a thorough understanding of the instability and general properties of nanocomposite systems becomes the key issue in the study of their microstructure, morphology, chemical composition and advanced use in various fields.

The NPs based on 11th group metals (Cu, Ag, Au) have fascinated people's research interests for centuries; in particular, silver is known for its water and air purifying ability, for use in vases, pottery and other ornaments. Nowadays, the biological activity of Ag NPs make it a suitable candidate for applications in industry and medical instruments as an antibacterial material compared to the corresponding bulk counterparts.

For the supporting matrices, metal oxides have received increasing attention due to their unique structures and different characteristics. Among the various oxide hosts, TiO_2 has been thoroughly studied owing to its novel features, such as optical transparency in the visible range, perfect dielectric property, thermal stability and weak interactions with metal NPs. As a consequence, Ag-TiO_2 nanocomposites have stimulated significant research interest in various areas such as photocatalysis, gas sensing, optical devices, solar cells and antimicrobials [10–14].

2.1.1 Titanium oxide thin films

Titanium oxide has been extensively studied by researchers as a stable and harmless material for many promising applications such as optical coatings, photocatalysts, sensors, solar cells, pigments, sunscreens, paints, etc. [15–26]. The majority of research on titanium dioxide is based on amorphous and three crystalline phases (anatase, rutile and brookite), as well as in various forms (thin films, NPs, nanowires, etc.) [27–30]. An exponential growth of research activities has been reported in enhancing the crystalline quality of titanium dioxide, especially focusing on anatase and rutile phases [31–34]. However, recent research has placed much emphasis on understanding the structure and morphology properties of amorphous titanium oxide, which is a less processed and much cheaper material [35–41].

TiO_2 thin film coatings are useful for many applications because the promising properties of high refractive index, durability, biocompatibility, high hardness, low absorption, etc. [42,43]. Many methods have been employed to prepare TiO_2 thin films, such as sol-gel [44–46], chemical vapor deposition (CVD) [47–49], hydrothermal [50–52], pulse laser deposition [53,54], atomic layer deposition (ALD) [55–57] and magnetron sputtering [58–60]. Among these techniques, magnetron sputtering is the most attractive and common method because it is an industrial process applicable to large scale and wide area deposition, and high quality and high deposition rates can be achieved under proper conditions. Only amorphous, anatase and rutile phases have been found in the deposited films, and these different phases can be controlled by the sputtering parameters, such as oxygen partial pressure, total

pressure, substrate temperature, target-substrate distance, bias, deposition rate and some assistant-combined devices [20,61].

Strong correlation has been observed between the total pressure and the crystalline phases of titanium dioxide, and it was found that the energy of the deposition particles in the sputtering process is responsible for the microstructure and the crystalline phase of titanium oxide [19,20,62–64]. M. Yamagishi [65] produced a rutile/anatase mixture TiO_2 crystalline structure at a very low total pressure (0.3 Pa), and it was proven that the sputtered Ti atoms and the high energy oxygen gas particles are able to deposit on the substrate without collisions because of the relative longer mean free path at low total pressure, forming a highly oriented crystalline phase. Another item contributing to the formation of rutile phase of TiO_2 is related to the density of ionic Ti^{4+}, O^{2-} in the plasma process which increased with decreasing total pressure [66]. As depicted in Figure 2.1, the kinetic energies of both Ar neutrals and oxygen negative ions become almost zero when the total pressure increased to 3 Pa, indicating no bombardment of high-energy particles during film deposition growth. The average kinetic energy of the Ar^0 or O^{2-} impinging on the substrate can be estimated from the Kevin-Meyer equation [65]:

$$E_{kAr^0} = (E_{iAr^0} - k_B T)\exp\left[N \ln\left(\frac{E_k}{E_i} \right) \right] + k_B T \qquad (2\text{-}1)$$

where E_i and E_k are the initial and kinetic energies of Ar^0 or O^{2-}, respectively. T is the temperature of sputtering process and N is the collision number.

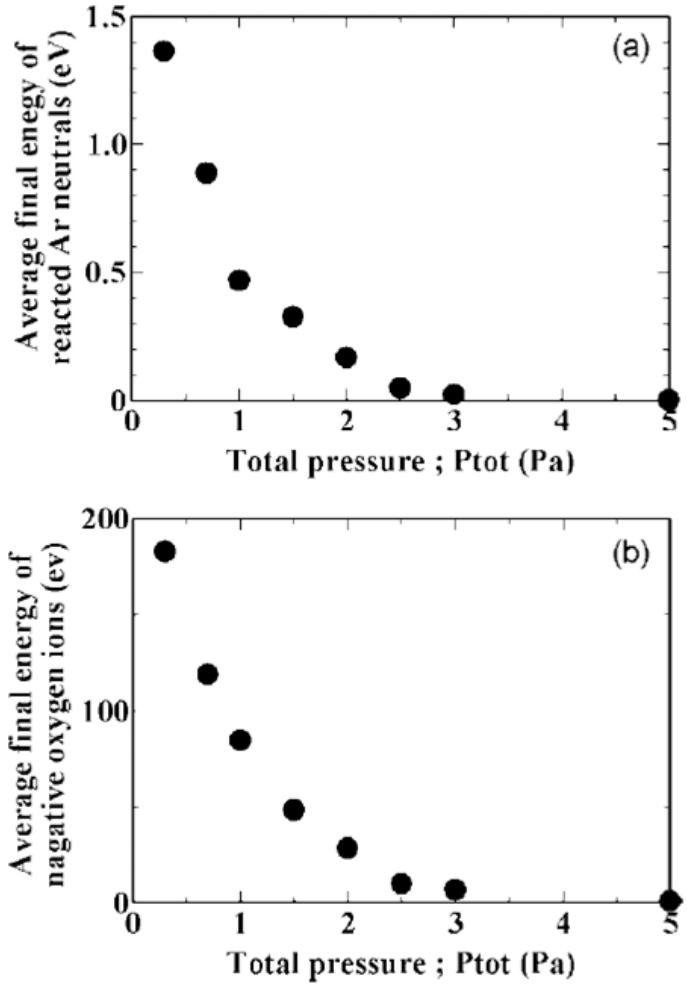

Figure 2.1 The calculated average kinetic energies of (a) Ar neutrals recoiled at the target and (b) negative oxygen ions (O^{2-}) accelerated in the cathode sheath reaching the growing film surface as a function of the P_{tot}. Elastic collisions are assumed in the gas mixture of 70% Ar and 30% O_2. Reprinted from [65], Copyright (2003), with permission from Elsevier.

Oxygen partial pressure is considered to be related to the discharge parameters, such as discharge voltage, deposition rate and plasma potential. With increasing oxygen partial pressure, the deposition rate of titanium oxide and plasma potential drop, and discharge voltage increases [67]. In addition, as the oxygen partial pressure increases, the deposition rate of titanium oxide decreases drastically due to the increasing compound coverage on the surface of the target. The composition of

deposited films are changing from metallic to titanium sub-oxide mixture and pure titanium dioxide [68] .

Considering the energy of the nucleation sites is a function of temperature, the crystalline phase of titanium oxide thin films also can form through substrate heating. Basically it is insufficient to form the rutile phase at room temperature, and the mixture structure of anatase/rutile phase can be formed when the substrate temperature rises up to 300 ℃. However, the grain size of titanium oxide increases with increasing substrate heating temperature, due to a thermal effect by the reaction between Ti particles and oxygen atoms on the substrate [69]. Besides, the post annealing process has the same effect on the phase change of titanium oxide films at various temperature [70].

Moreover, in order to expand the application fields of TiO_2 thin films, development of the surface modification such as doping metal elements is necessary [71–77]. For example, doping of noble metal elements into TiO_2 coatings has attracted intense research interest due to their promising antimicrobial use for biomedical applications [78–80].

2.1.2 Silver NPs and ions

Ag NPs are clusters of silver atoms that range from 1 to 100 nm and are attracting research interest due to their many innovative properties which are associated with their enhanced functional characteristics [81–84]. Owing to their antimicrobial properties, Ag NPs are the most commonly used engineering nanomaterials for use in a broad array of medical applications [85–88]. Silver nitrate ($AgNO_3$) has been used since the 17th century as an essential medical product, and nowadays silver-containing agents are used in coatings on medical devices, food packaging, water disinfectants and textiles [89,90].

Metallic silver NPs can strongly affect silver's bioavailability towards any biological systems because silver can be oxidized and result in the release of silver

ions. In the presence of oxygen and moisture, metallic silver NPs are oxidized, which results in the release of Ag ions. In the study of Liu et al. [91] the purpose was to clarify the kinetics of silver ion release from Ag NPs. The results indicated that the silver ion release is a cooperative oxidation process involving protons and dissolved oxygen. In solutions containing no other oxidants or reductants, the global reaction stoichiometry should be:

$$2Ag_{(s)} + \frac{1}{2}O_{2(aq)} + 2H^{+} \Leftrightarrow 2Ag^{+}_{(aq)} + H_2O_{(I)} \tag{2-2}$$

where ΔG^{0}_{rxn} value is $-91.3 KJ/mol$ at room temperature. From this equation, one can see in the presence of dissolved oxygen, silver ion release is enhanced when the pH value is decreased, demonstrating the importance of protons and oxygen. In addition, a decreasing pH environment would increase the dissolution of metallic silver NPs [92]. The surface charge of Ag NPs is negative at a neutral pH value; if the surface charge of Ag NPs is neutralized as a function of pH, aggregation occurs. Silver ion release increases with temperature and decreases with increasing pH value or addition of humic or fulvic acids.

Silver oxidation is a slow reaction which strongly depends on the Ag NPs properties [93], therefore in many studies the dissolution of the silver NPs was found to be size-dependent, as the ion release rate increases exponentially as the particle size decreases [94,95]. Smaller particles were found to be more toxic due to the larger surface area of the same mass of silver which could facilitate faster dissolution and silver ion release. Classically, a modified form of the Kelvin equation, also known as the Ostwald-Freundlich equation, is used here to describe the size dependent solubility of NPs.

$$\frac{S}{S_0} = \exp\left(\frac{2\gamma V}{RTr}\right) \tag{2-3}$$

where S is the solubility(mol/Kg) of spherical particles with radius r , S_0 is the solubility of the bulk, V is the molecular volume(m^3/mol), γ is the surface tension in mJ/m^2 , R is the gas constant and T is the temperature. According to equation (2-3), the solubility of NPs increases exponentially as the particle size decreases; the

most significant enhancement in the solubility is expected for extremely small particles, i.e. particle sizes less than 5 nm [96]. In addition, metal particles of small sizes around 5 nm present electronic effects, which are defined as changes in the local electronic structure of the surface because of size. These effects are supposed to enhance the reactivity of metal particles [97].

However, in other studies, no correlation between particle size and dissolved silver ions were found after Ag NPs were coated in different ways [98,99]. For instance, Yang et al. [98] reported that the dissolved silver ions from the Ag NPs with larger size was twice that of smaller NPs, because the coatings and interactions with biomolecules can influence silver ion release rate, as ionic species in solution can affect the sizes and size distribution of Ag NPs.

Additionally, it has been shown that ion release rate is facet dependent because of the presence of facets with specific crystallographic orientations, which is related to the percentage of surface atoms and activity [96]. Morones et al. [100] reported that the reactivity of Ag NPs is favored by high atom density facets such as {111} and caused a strong interaction with the surface of bacterial membrane.

Since Ag NPs are unstable in suspension and easily aggregate with each other, different kinds of coatings and capping agents are used to decrease aggregation and speed up dissolution of Ag NPs [101–104]. Aggregation occurs when the attractive forces between NPs are greater than the repulsive forces. If the repulsive forces are larger than attractive forces, an energy barrier for particle aggregation will be created and aggregation will not happen. The stability of silver NPs has strong influence on their antimicrobial ability, because silver ions are considered to be one of the main silver toxicity factors. Furthermore, different coatings and capping agents may result in different surface charges, which could significantly influence Ag NPs interaction with microbial system [105]. Usually, capping agents and coatings are used to enhance the Ag NP colloidal stability and the choice of capping material used to protect or passivate the NP surface. Furthermore, if Ag NPs were completely covered by sorption of organic compounds, van der Waals attractive force would be shielded, which would prevent NPs aggregation. These sorbed agents would modify the surface characteristics of particle surfaces and change the interactions of NPs with the

medium. For instance, sorption of hydrophobic groups may promote destabilization of the NPs, while hydrophilic agents could slow down aggregation of NPs [106].

The behavior of Ag NPs in different aqueous media is difficult to conclude due to the complex environment of Ag NPs in these solutions. The most important things for the behavior and effects on bio-organisms include aggregation and oxidation of Ag NPs, subsequent dissolution to dissolved Ag ions, solubility of silver ions in solutions and reactions changing the reactivity of Ag metal NPs [107–109] . Factors such as media composition, ionic strength, pH value, dissolved organic matter, humidity of the environment, dissolved oxygen concentration, temperature and their concentration would all influence the transformation of Ag NPs in the solutions [106,110–116] .

To evaluate the fate of Ag NPs in aqueous solutions, the dissolution or release of silver ions and the stability of Ag NPs with regard to their size and colloidal dispersion. With decreasing size of Ag NPs, the potential for silver ion release increases and moves from the silver sulphide extreme (minimum release) toward silver nitrate extreme (maximal release) [117]. Very small Ag NPs can be transported with the water and easily interact with bio-organisms. However, if the size of Ag NPs is larger due to aggregation, they become less mobile and will tend to slow down the ion release process.

From the equation (2-3), silver ion release is supposed to be dependent on the presence of oxygen. Release can be promoted by methods to pre-establish the chemisorbed oxygen complex and inhibited by scavenging reactive oxygen intermediates from the surrounding medium [116]. The presence of ligands for silver ions may lead to increased dissolution of Ag NPs by formation of Ag^{+} complexes [118].

In addition, the conditions of storage environment such as relative humidity have a great impact on Ag NPs transformation. As observed by Glover et al. [119] new Ag NPs were formed near the parent ones when stored under ambient and dark conditions at relative humidity larger than 50%. The authors proposed a three-stage model for new particles formation (Figure 2.2). First, the surface of Ag NPs becomes oxidized in the presence of water and oxygen, producing silver ions in the absorbed

water layer. Second, these dissolved silver ions diffuse away from the parent Ag NPs as a result of the strong concentration gradients around the parent particles. Finally, new smaller metallic Ag NPs are reformed through reduction of the silver ions on the surface. Both chemical and photo-reduction seemed to be crucial for the last step of the process. Additionally, it was found that light also had a great influence on the extent of Ag NPs degradation and reformation (photo-reduction process). The parent particles exposed to a 100% relative humidity chamber but held in ambient light condition showed significant degradation, while the sample held in darkness showed little degradation.

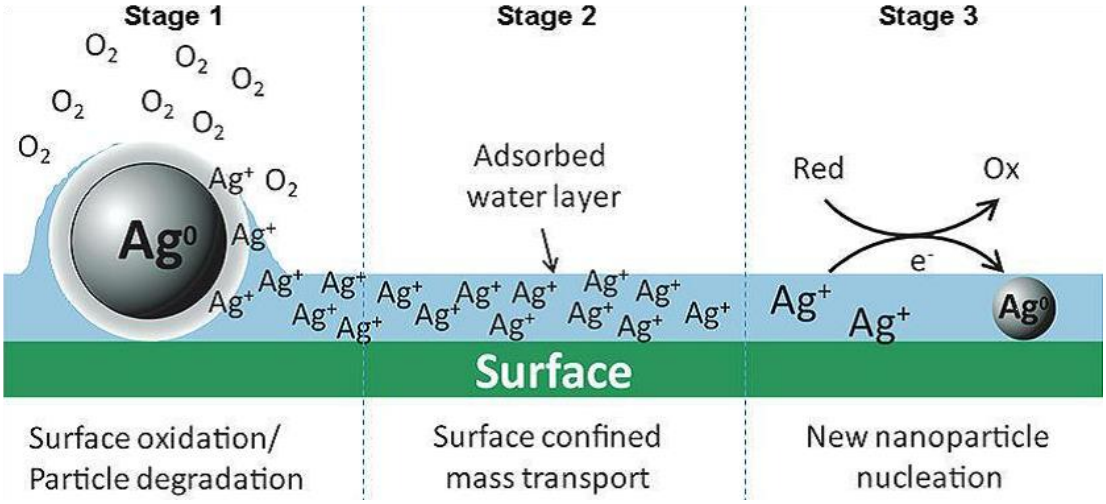

Figure 2.2 Proposed pathway for new particle formation away from parent Ag NPs. Reprinted with permission from [119]. Copyright (2011) American Chemical Society.

Despite the promising advantages of using Ag NP based applications, the potential human health and environmental concerns are heightened due to the widespread use of Ag NPs in washing machines and similar usages, which can cause direct Ag ions release into environmental or biological systems. The rapid consuming of Ag NPs in commercial products leads to an estimated 270 tons released per year into the environment [120]. This release could be toxic to human cells and other organisms in different concentrations [121–123]. For instance, Braydich-Stolle et al. [124] found that silver concentration between 5 μg/mL and 10 μg/mL could induce toxicity to mouse spermatogonial stem cells. Moreover, the silver NPs are found to be

toxic to mammalian cells at concentrations higher than 60 mg/L, while ionic silver retains its cytotoxicity even at 1 mg/L [125]. Thus the silver ion release potential or silver ion tuning becomes a key issue in silver nanomaterial products. The release potential of different silver materials can be distributed between the silver sulfide and silver nitrate extremes (Figure 2.3) [117]. One can easily find that bulk silver metal releases silver ions to a very small extent, and the potential for silver ion release increases as the size of silver metal decreases from bulk to nanosized particles. This may be due to the solubility and dissolution kinetics of silver that varies as a function of size as the silver metal size decreases. However, silver-ion materials and silver salts still have higher release potential, even as silver-ion release ability improves with smaller silver particle size [126].

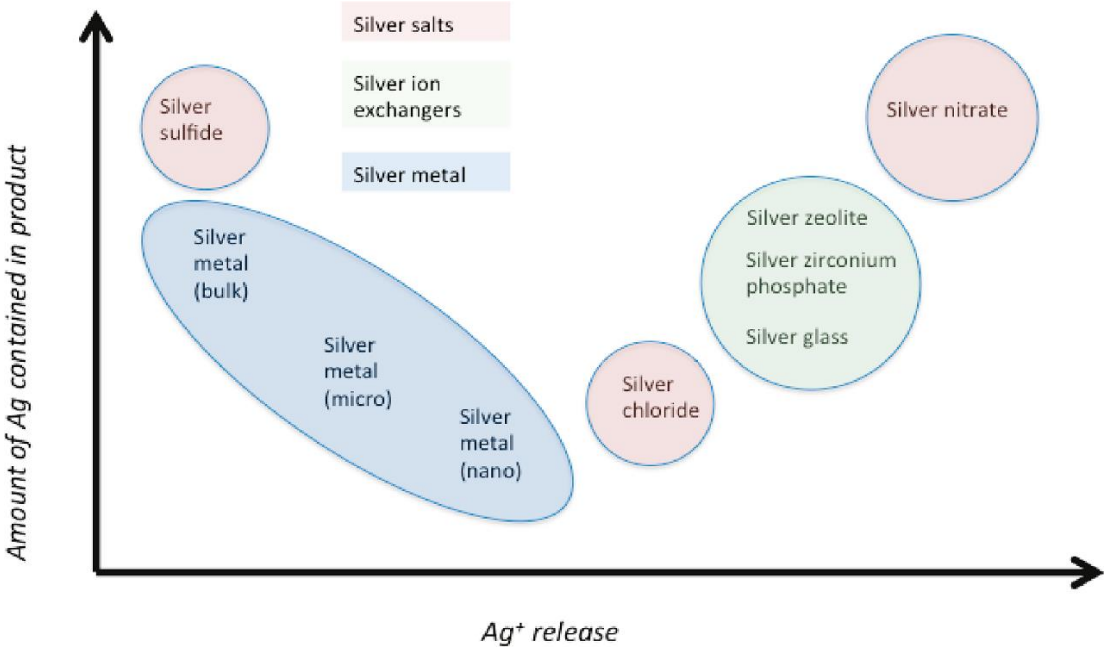

Figure 2.3 Silver release and amount of silver required in products for different silver formulations. Reprinted with permission from [117]. Copyright (2011) American Chemical Society.

In addition, silver ion release from titanium oxide nanocomposites has shown different properties [127,128]. For silver ion release in an aqueous solution, firstly, water molecules are required to enter the matrix to oxidize the metallic silver NPs; the diffusivity of water molecules through the titanium oxide pores and slits is related with the surface morphology, microstructure and hydrophilicity property of the

titanium oxide matrix [129,130]. Secondly, the oxidation of metallic silver NPs to silver ions would occur to a great extent when a larger total surface area of Ag NPs is exposed to water molecules. Lee et al. [131] found the fact that the oxidation of zerovalent Ag into silver ions at the surface of the NPs is the rate-limiting step and that the diffusion of silver ions out of the matrix is a very fast process compared to the ionization process. Silver ionization and release are dependent on water uptake and the morphology of the Ag NPs. Akahavan [128] found that the durability of the 3D nanocomposite Ag-TiO_x films was at least 11 times higher than the 2D films; silver ion release presented a slower but long-lasting property in the 3D nanocomposites compared to the 2D structure, which may be attributed to the inter-diffusion of water, the Ag NP size and shape distribution, degree of particle aggregation and interaction of silver surface with the titanium dioxide host.

2.1.3 Silver oxide forms

Silver is always covered with an adsorbed atomic oxygen overlayer which prevents the further oxidation of the metal even under ambient conditions, and therefore the metal is strongly resistant to corrosion [132,133]. The occurring oxide thickness on silver exposed to ambient conditions is in the range 10-20 Å. The oxidation mechanism of silver in atomic oxygen is essentially linear-parabolic as postulated and experimentally confirmed [134]. The thermodynamical equilibrium of silver bulk and oxygen at standard temperatures and pressures

$$2Ag + \frac{1}{2}O_2 \rightarrow Ag_2O \tag{2-4}$$

lies, as will be calculated, at the right-hand side of the chemical reaction. However, the equilibrium constant K_p for the above reaction can be expressed as

$$K_p = \partial_p (\partial_{Ag})^{-2} (P_{O_2})^{-1/2} \tag{2-5}$$

where ∂_p and ∂_{Ag} are the activities of Ag_2O and Ag respectively (both values are unity), P_{O_2} is the equilibrium partial pressure of oxygen. Then substitution of K_p into the standard free energy equation yields

$$\Delta G_T = \frac{1}{2} RT \ln P_{O_2} \tag{2-6}$$

where T is the absolute temperature and R is the universal gas constant. For $T = 298K$, then the change of free energy in this reaction (2-4) is $\Delta G_{298K} = -11.2KJ.mol^{-1}$, where Ag_2O can be formed.

Several observations related to the mechanism of the oxidation process are reported and should be taken into account for silver metal exposed to oxygen, such as the oxidation process depends on the temperature and the silver oxide growth is parabolic with time at constant temperature, etc. As oxygen diffusion is a temperature-related process, the silver oxidation rate will vary exponentially with the temperature because the oxygen diffusion coefficient increases exponentially with the temperature. The silver oxidation rate $\frac{dy}{dt}$ can be expressed by the following Arrhenius equation:

$$\frac{dy}{dt} = Ae^{-E/(RT)} \tag{2-7}$$

where A is the pre-exponential factor, E is the activation energy, T is the absolute temperature and R is the universal gas constant.

The oxidation model reported by A. Rooij [135] pointed out that the transport of oxygen through the silver oxide layer is controlled by micro-pores at low temperature while dominated by Fickian diffusion at higher temperature. The oxygen diffusion is inversely proportional to the thickness of the silver oxide layer in the Fickian diffusion. And the oxygen diffusion is inversely proportional to the length of the micro-pore while at room temperature. However, a high oxidation rate at room temperature indicates a different oxidation process, which is known as gas flow through micro-pores. The oxygen flow through micro-pores depends on the dimensions of the pores and the mean free path of oxygen molecule collisions. In addition, the mean free path of oxygen molecules varies with pressure. At low pressures (free-molecular regime), the collisions between oxygen atoms are less frequent than the wall collisions and the mean free path of an oxygen molecule is larger than the dimensions of the pores; at higher pressures (viscous flow), where the

collisions with other molecules are frequent, the behavior of an individual oxygen molecule is determined by the motion of gas molecules. The oxygen atoms reaching the silver metal surface will form silver oxide films at room temperature, and this reaction is usually linear and with an oxygen flux of:

$$F = \frac{dy}{dt} n_{O_2} \tag{2-8}$$

where $\frac{dy}{dt}$ is the rate of silver oxidation, n_{O_2} is the gas density of oxygen. The interfacial reaction between oxygen atoms and silver metal results in a linear-parabolic oxidation with flux and time.

In the case of smaller silver NPs, the extremely small size (nm) results in the particles having a very large surface to volume ratio, and a negative shift in standard electrode potential which can enhance the interaction with oxygen molecule or atoms and are more easily oxidized than silver bulk [136]. Hence, it is very important to find the silver NPs oxidation process to optimize silver nanomaterials for various applications. Park et al. [137] proposed a "shrinking core" model for explaining the nanoparticle oxidation process based on his observation of Al particles; the major approximation for this model is the assumption that the NPs are spherical. The "shrinking core" model supposed that the metal oxidation process is dominated by three steps:

Step 1: diffusion of oxygen through the outside film surrounding the particle to particle surface.

Step 2: diffusion of oxygen through the oxide shell to the surface of particle core.

Step 3: chemical reaction of oxygen with metal at unreacted core surface.

The oxidation rate is slowed down with thickness increase of the oxidized layer covering the particle surface. Moreover, since the smaller size of silver NPs means a large surface to volume ratio and thus a higher surface energy than the silver bulk, the oxidation rate of smaller size particles is indeed faster than those of larger particles, which are also observed in Al and Si NPs [138,139].

Moreover, silver exhibits a high photosensitivity, which seems to be related to the oxidation state of the silver NPs. Concerning the intense interest of silver

antimicrobial activities, it was found that partially oxidized silver NPs appeared with preferential antibacterial ability because of silver-ion release [8,140–142] . It is reported that Spatial Modulation Spectroscopy (SMS) [143] is introduced to observe silver NP photoaging process and to avoid oxidation by the electron beam of transmission electron microscopy (TEM). The related optical measurement performed under nitrogen, argon or vacuum environments indicated that these oxygen-free atmospheres could prevent the oxidation of silver NPs [144–146]. However, a shell of lower contrast and some smaller particles surrounding the parent silver NPs was observed; the reduction of the silver NPs size may be attributed to overheating and a chemical modification under illumination in the ambient atmosphere [147–150]. The oxidation process clearly indicates a photochemical reaction at the metal-oxygen interface, involving native oxygen and UV light. The thin oxidation shell surrounding the silver metal core corresponds to a metal part where the density of free electrons is reduced due to the high chemical surface sensitivity of silver NPs [151,152]. The chemisorption of oxygen occurring at the silver NPs surface

$$Ag + O_2 \rightarrow Ag^+ + O_{2(ads)}^- \tag{2-9}$$

leading to the morphology and resonance wavelength change of silver NPs by a charge transfer from silver metal to the surroundings.

This photo-oxidation process not only happened on spherical silver NPs but was also observed for other shapes of silver NPs [153]. The oxidation process in nanocubes is slower and less homogeneous than in spherical silver NPs, and an irregular oxide shell of low contrast is formed around the silver metallic cube ore which presents rounded corners and edges, which can be explained by the enhancement of electromagnetic field on edges and corners.

Additionally, the effects of various surfactant stabilizers on the photo-oxidation process have been studied [142,153,154]. PVP exhibits a remarkable effect of slowing down the photo-oxidation process of silver NPs, whereas the citrate stabilizer is unable to protect silver NPs from oxidation because of its shorter carbon chain. Thus a dense shell of silica could prevent the silver metal core from oxidation for a very long period [155].

Silver oxide (Ag_2O) also plays an crucial role for morphological changes of silver nanoclusters [156]. A bimodal size distribution of silver cluster sizes is exhibited after oxygen exposure, with some clusters increasing in size while others decrease. In addition, a slight increase in silver cluster density was observed, indicating that the cluster redispersion simultaneously occurs with Ostwald ripening. It is well known that silver cluster growth can proceed by two processes. First, silver clusters can migrate on the substrate surface until they collide with each other, resulting in coalescence; secondly, silver clusters could grow by intercluster transport (Ostwald ripening), which is dependant on capillarity force. However, silver atoms or clusters are mostly stable under ultra high vacuum conditions, thus the formation of Ag_2O in an oxygen gas environment could be the reason for silver growth, and the equilibrium oxygen partial pressure can be calculated to be 1.23×10^{-4} atm (0.094 Torr). Since oxygen ions have an important effect on inducing Ag_2O aggregation, a high oxygen flow rate should be avoided in the reactive sputtering process.

Furthermore, it has been found recently that energetic oxygen ions with sufficient energy can modify the structure of Ag-TiO_x nanocomposites and induce the diffusion of Ag to the surface of the titanium oxide matrix during reactive sputtering [157]. It is clear that in reactive sputtering processes of metal oxides, a huge number of oxygen ions are created at the target surface, which could be sputtered toward the growing film with energies often reaching the full cathode voltage. Therefore, it was assumed that such energetic oxygen ions strongly destroy the structure integrity of the nanocomposites and result in the diffusion of Ag atoms with oxygen ions onto the surface to minimize the surface energy of the system [158–161].

2.1.4 Surfaces segregation

Surface segregation refers to the enrichment of a material constituent at a free surface. Constituent atoms of small surface free enthalpy in a multicomponent system have the tendency to accumulate at the surface to reduce the total free enthalpy of the system, thereby causing a localized enrichment of this material on the surface [162]. The surface segregation was first predicted by Gibbs [163] who pointed out that the reduction of the surface energy is the driving force. The free energy of surface segregation can be given by

$$\Delta G_s = \Delta H_s - T\Delta S_s \tag{2-10}$$

where ΔH_s is the enthalpy of surface segregates, T is the temperature and S is the entropy of surface segregates.

The formation of segregation could happen at a surface, an interface, a dislocation and a grain boundary in metal alloys and composites. The segregation can be divided into two types: equilibrium segregation and non-equilibrium segregation. The equilibrium segregated state is the lowest energy state in a system and the extent of the segregation effect decreases with increasing temperature. However, non-equilibrium segregation has only been observed in grain boundary regions during the quenching process, and the magnitude of non-equilibrium segregation increases with increasing temperature [164].

In the case of equilibrium segregation, the diffusion models for segregation to a free surface starting from a homogeneous bulk distribution system has attracted extensive investigation [165,166]. However, the solution to most conventional diffusion models based on Fick's first law could not provide a reasonable surface concentration profile for the segregating materials, e.g. the linear relationship derived between the surface concentration of the segregation part and $(Dt)^{1/2}$, where D is the diffusion coefficient and t is the time, then the surface concentration is unlimited at $t \to \infty$.

Since Fick's first law is no longer applicable when the concentration is very low, very high or the particle motion changes suddenly in a short distance, it needs to be

modified for the segregation to a free surface, where the particle motion is anisotropic [167]. The diffusion model was discussed in-depth by Cao [168].

Previous studies on Ag/TiO_x nanocomposite coatings showed strong segregation of silver towards the surface. This originates from the driving force of silver to diffuse to the surface to reduce the interfacial and strain energies. This behavior contrast sharply to the behavior of metal NPs in polymers [169]. Here even embedding of metal NPs deposited on polymer surfaces was observed and attributed to the reduction of the high surface energy of the metal NPs. There is a driving force for embedding of metal clusters, the Gibbs free energy of a metal particle in the polymer is smaller than that of the particle at the surface. This is related to the relative high cohesive energy of metals which gives rise to a high Gibbs free energy of metal particles. The surface Gibbs free energy of metal particles can be reduced by embedding if the surface tension of the metal particles γ_M exceeds the sum of the interfacial tension γ_{MP} and the polymer surface tension γ_P:

$$\gamma_M > \gamma_{MP} + \gamma_P \tag{2-11}$$

Since the cohesive energy of metal particles is typically 2 orders of magnitude higher than that of polymers, the embedding of metal particles should require long−range chain mobility, and the polymer can easily accommodate the stress associated with the embedding process. However, the growth of silver NPs in the ceramic TiO_x matrix is expected to give rise to large stress, which would cause large silver clusters favorably grown at the surface.

It is reported [170] that the efforts towards suppressing the surface segregation in Ag/TiO_x nanocomposite systems were successful by depositing 20 nm of TiO_x continuously after switching the silver source in a non-reactive sputtering process. No large Ag NPs can be grown on the surface because the thickness of the 20 nm barrier is larger than the depth of the depleted zone and thus silver atoms from the bulk could not reach the surface.

However, controlling surface segregation of Ag/TiO_x nanocomposite systems in reactive sputtering processes is more complicated because reactive gas is involved.

What is happening during reactive sputtering process and why it is happening are still not clear and need to be investigated systematically.

2.2 Physical Vapor Deposition

Numerous techniques have been developed for the deposition of thin films, including sol-gel and hydrothermal methods, chemical vapor deposition (CVD) and physical vapor deposition (PVD). PVD is a variety of vacuum deposition used to deposit thin films by the condensation of a vaporized form of the desired film material onto various substrates. Typical PVD techniques include thermal evaporation, cathodic arc deposition, pulsed laser deposition and sputtering processes. In evaporation, atoms are removed from the source by thermal means, whereas in sputtering they are ejected from the solid target (source) surface through collisional impact of gaseous ions, which are then transported through a vacuum environment to the substrate. From among the different physical vapor deposition techniques, sputtering is clearly used extensively in both the scientific community and industrial plants to deposit a wide variety of thin film materials. Here we focus on sputtering processes and divide them into four categories: (1) dc, (2) RF, (3) magnetron, (4) reactive.

2.2.1 DC sputtering

DC sputtering is also known as diode or cathodic sputtering. Already in 1852, Grove observed the deposition of a metal thin film opposite the cathode of a dc glow discharge. Figure 2.4 depicts the common DC sputtering system configuration. Initially the system is pumped down to 10^{-4} –10^{-5} Pa for purity, and then the gas molecules are ionized and energized by collisions; eventually they will have enough energy to cause ejection of atoms from the cathode surface. However, at low pressures, the cathode sheath is wide and ions are produced far from the target, their chances of being lost to the chamber wall are great. The mean-free electron path between collisions is large, and electrons collected by the anode are not replenished by ion-impact-induced cathode secondary emission. Therefore, ionization efficiencies are low and only a small fraction of the gas is converted to ions, and self-sustained discharges cannot be maintained below about 1.3 Pa. But if the pressure is too high,

the sputtered atoms undergo increased collisional scattering and are not efficiently deposited, leading to a poor film quality.

The major limitation of DC sputtering

• DC sputtering is only effective for sputtering conductive samples.

• The deposition rate is quite low.

• In case of high resistivity of the target, running an appreciable current through would require an impossibly large voltage (~10^{12} V).

• The lack of a current will extinguish the plasma and stop the process.

• This practically limits DC sputtering to materials of a resistivity less than 10^{6} Ω.cm (no insulators).

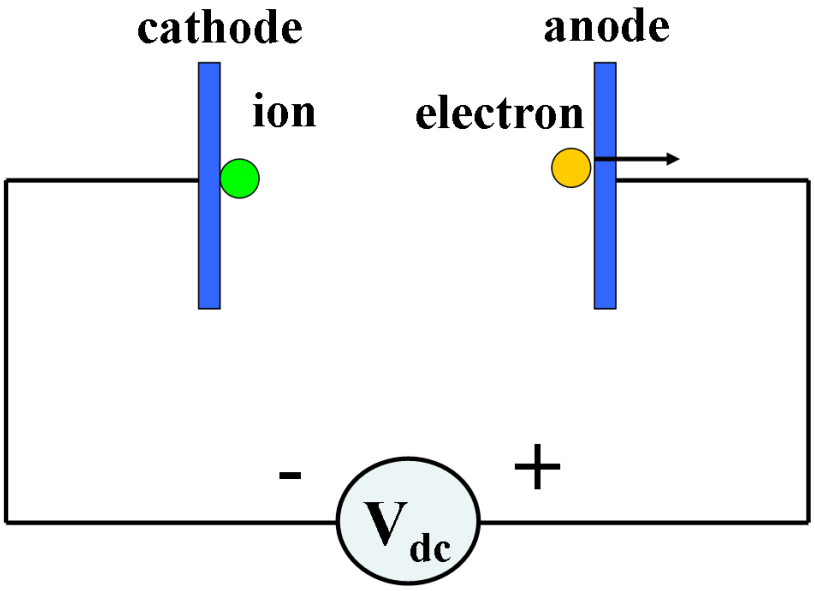

Figure 2.4 depicts the common DC sputtering system configuration.

2.2.2 RF sputtering

RF sputtering was invented as a means of depositing insulating thin films. Typical RF frequencies employed range from 5 to 30 MHz, however, 13.56 MHz has been reserved for plasma processing by the Federal Communications Commission and International Telecommunications Union. The basic configuration of RF sputtering is shown in Figure 2.5 (a).

RF sputtering essentially works because the target self-biases to a negative potential. Once this happens, it behaves like a dc target where positive ion bombardment sputters away atoms for subsequent deposition as depicted in Figure 2.5 (b). On the positive cycle, electrons are attracted to the cathode, creating a negative bias; on the negative cycle ion bombardment continues. The mobility disparity between the ions and the electrons is that the target will automatically tend to bias itself more negatively than the anode. This is because the highly mobile electrons enable a larger electron flow through the anode while the more sedentary ions provide a lower current to the cathode. This asymmetry creates a negatively biased current through the plasma. Normally the RF peak to peak voltage is around 1000 V, electron densities are around 10^{9}-10^{11} cm^{-3}. On the positive cycle, electrons are attracted to the cathode, creating a negative bias; on the negative cycle ion bombardment continues.

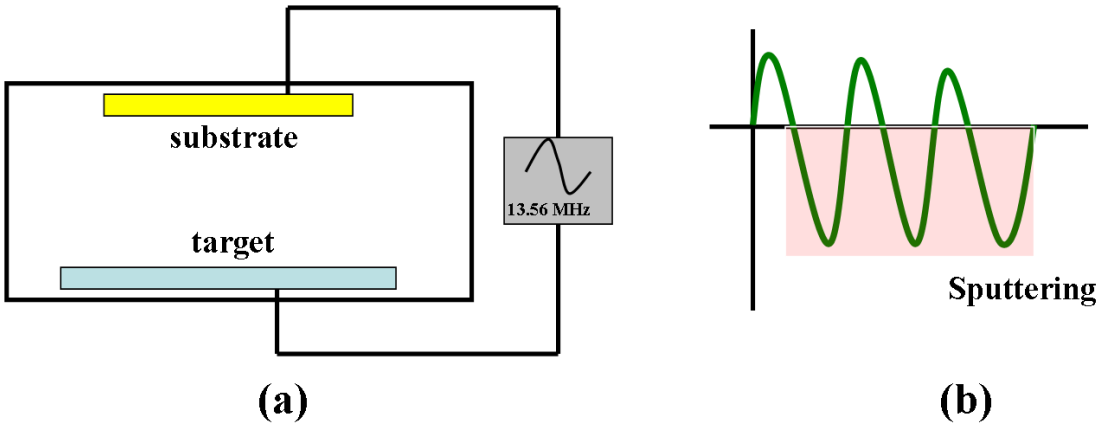

Figure 2.5 (a) The basic configuration of RF sputtering device; (b) The working principle of RF sputtering.

One can realize that both the target and substrate should sputter due to the reason that ac electricity is involved. This can be overcome by making the target area small compared to the substrate. Since capacitive reactance is inversely proportional to the capacitance or area, more voltage will be dropped across the capacitor of a smaller surface area. Therefore, for efficient sputtering the area of the target electrode should be small compared with the total area of the other electrode. It has been shown that the ratio of voltage across the sheath at the small capacitively coupled electrode (v_t) to that across the large directly coupled electrode (v_s) is given by

$$\frac{v_t}{v_s} = \left(\frac{A_s}{A_t}\right)^4 \qquad (2\text{-}12)$$

where A_s and A_t are the respective electrode areas [171].

Although any type of film can be RF sputtered, deposition rates are still low. In addition RF power is not so simple, power supplies are expensive and additional circuitry is needed. The primary disadvantage of the use of RF power supplies, in addition to expense and reliability is the inherently low deposition rate. This is because magnetron sputtering, which relies on a closed electromagnetic trap at the target is fundamentally a dc concept. The RF field alternately opens and closes the trap, allowing electrons to escape when the trap is open and forcing electrons to cross magnetic field lines, and hence drop power in the discharge, which decreases the available power at the target when it is closed. The deposition rate for a given applied target power decreases with both increasing frequency [172] and increasing magnetic field [173].

2.2.3 Magnetron sputtering

The original idea of magnetron sputtering goes back to Penning in 1936, who already achieved extremely high deposition rates in a cylindrical magnetron [174]. At this time, the potential of the magnetron for high-rate and large-area depositions was not yet recognized. The introduction of balanced magnetrons in the early 1970s [175,176] was an important step in overcoming the limitations of the basic sputtering process. However, it was the development of the unbalanced magnetron in the late

1980s [177–181] that transformed the capabilities of this technique, and has subsequently been responsible for its rise in importance.

A schematic diagram of a magnetron sputtering deposition device is shown in Figure 2.6 (a). It is a plasma-assisted deposition process, where the plasma is confined in front of the target surface, which has to be deposited, by magnetic confinement of the electrons. One can see in Figure 2.6 (b) the magnets are arranged in such a way that one pole is positioned at the central axis of the target and the second pole is formed by a ring of magnets around the outer edge of the target. Trapping the electrons in this way substantially increases the probability of an ionizing electron-atom collision occurring. The increased ionization efficiency of a magnetron results in a dense plasma in the target region. This, in turn, leads to increased ion bombardment of the target, giving higher deposition rates at the substrate. Target erosion by sputtering occurs with this electron race track because ionization of the working gas is most intense above this region. In addition, the increased ionization efficiency achieved in the magnetron mode allows the discharge to be maintained at lower operating pressures (typically, 10^{-3} mbar). In contrast to the electrons, the ions and neutral particles are almost not influenced by the magnetic field.

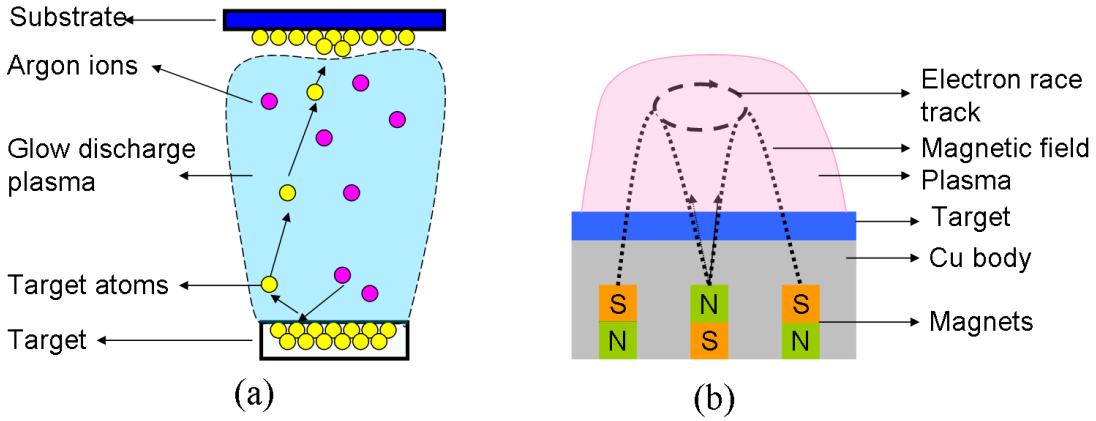

Figure 2.6 (a) The basic scheme of magnetron sputtering; (b) The inner configuration of a sputtered target in magnetron sputtering.

In a balanced magnetron sputtering, the plasma is strongly confined close to the target region. A region of dense plasma typically extends 60 mm from the target

surface. If the substrate is placed within this region, it can strongly influence the morphology and properties of the growing film on them. While substrates positioned outside this region, however, will lie in an area of low plasma density and subsequently insufficient ion current draw at the substrates cannot influence the properties of the film.

However, it can be a distinct advantage to deliver more energy to the substrate to achieve high adhesion films in some cases. A possible solution is "unbalancing" the magnetron configuration, or changing the magnetic field strength of the inner versus outer magnets. In an unbalanced magnetron device the outer ring of magnets is strengthened relative to the central pole. In this case, not all the field lines are closed between the central and outer poles in the magnetron, but some are directed towards the substrate, and some secondary electrons are able to follow these field lines. Consequently, the plasma is no longer strongly confined to the target region, but is also allowed to flow out towards the substrate. Thus, high ion currents can be extracted from the plasma without the need to externally bias the substrate.

By modifying the magnetic field strength balance between the outer and inner magnets, one can tune the electron flux, and hence the ion flux, incident at the substrate. One way to characterize the magnet balance is the ratio K between the magnetic flux through the outer and the inner magnets,

$$K = \frac{\Phi_{out}}{\Phi_{in}} = \frac{\int_{S_{out}} B_{\perp out} dS_{out}}{\int_{S_{in}} B_{\perp in} dS_{in}} \tag{2-13}$$

$B_\perp$ represents the magnetic field strength perpendicular to the magnet, and S is the area of the magnet [182].

Researchers have subsequently shown that substrate ion current densities of 5 mA/cm^2 and greater, i.e. approximately an order of magnitude higher than for a conventional magnetron, can be routinely generated when using an unbalanced magnetron [183–185]. However, for the opposite case where the central pole was strengthened relative to the outer pole, the magnet field lines which do not close in on themselves are directed towards the chamber walls and the plasma density in the substrate region is low, therefore this case is not commonly used because the ion currents are low at the substrates.

2.2.4 Reactive sputtering

In reactive sputtering, compounds are deposited on substrates by sputtering from metallic targets in the presence of a reactive gas (e.g. Nitrogen, Oxygen), usually mixed with the inert working gas (normally Argon). By simply adding a gas that reacts with the metallic target, which can achieve a high sputtering rate and desired stoichiometry of the deposited film, it is possible to form a wide variety of functional compound thin film coatings.

However, the addition of the reactive gas to the sputtering influences the deposition process in several ways and may cause some processing stability problems. An overly high supply of the reactive gas will cause target poisoning which could reduce the deposition rate significantly, while an insufficient supply of the reactive gas will lead to an understoichiometry compound thin film. Therefore there may exist optimum conditions where both desired stoichiometry film composition and high deposition rates can be achieved. Some aspects of the reactive sputter deposition processes are discussed in this part.

The main issue that must be faced in the reactive sputtering process is that the reaction not only occurs on the surface of substrate, but also takes place on the surface of target materials and chamber walls. A model proposed by Berg et al. [186] provides an in-depth discussion of reactive sputtering. As depicted in Figure 2.7, we assume a target (area A_t) in front of a substrate surface (area A_s) in a sputtering chamber. Since there is reactive gas present, the reactions between metallic target atoms and the reactive gas will cause a fraction ψ_t of the target to consist of compound molecules. Then the remaining part $(1-\psi_t)$ of the target surface consists of metallic non-reacted target atoms. The compound fraction at this surface area of the substrate is denoted ψ_s. Normally the sputtering rate for the compound that forms on the metallic target is significantly lower than the rate of pure metallic target material, thus the deposition rate of target decreases as the coverage degree of target compound increases. When the whole target surface is covered with the compound material, then the target poisoning happens and the rate of deposition decreases to a very low value.

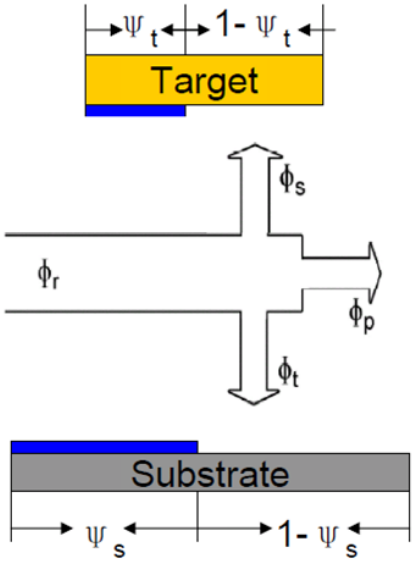

Figure 2.7 Flows of reactive gas during reactive sputtering process.

If the addition of the reactive gas into the chamber is increased, initially the partial pressure of the reactive gas in the chamber remains very low as is shown in Figure 2.8 (a) for the reactive sputtering of titanium–oxygen systems. The oxygen partial pressure remains at a very low value at the initial stage because most of the gas reacts with the sputtered metallic titanium and is being getter pumped. When the flow of the reactive gas reaches a sufficiently high level, in this case at point A at about 10.3 sccm, the partial pressure of the reactive gas suddenly increases to point B. This substantial change in the partial pressure is an effect of target poisoning. Once the TiO_x compound forms on the target surface, the partial pressure increases because less sputtered titanium target material reacts with the oxygen gas. Any further increase in the reactive gas flow past point B just leads to a linear increase in its partial pressure because of the constant pumping speed. However, when the gas flow of the oxygen is decreased from point B, the partial pressure of the oxygen does not return immediately to its previous low value. Instead the partial pressure remains high as the flow is decreased compared to when the flow was increasing until the compound layer on the surface of the target is removed at point C. At this point, the flux of the sputtered titanium material increases rapidly due to its higher sputter yield compared with TiO_x, which results in a higher gettering rate for the oxygen and a

reduction in its partial pressure to point D. The region ABCD denoted the width of "hysteresis loop", which is demonstrated extensively by Sproul and Berg [186,187].

The hysteresis behavior shows two stable states of the reactive sputtering process with a rapid transition region between them. The transition region (A-B) is triggered by compound formation on the surface of the titanium target. It is desirable to control the deposition in this transition region between the metallic mode and compound mode of the target to obtain a high deposition rate and optimum stoichiometry compound of thin films. But this is not easy in most cases by flow control of the reactive gas due to the unstable condition.

It is reported that some groups [188,189] demonstrated that it is possible to control the partial pressure of the reactive gas directly during reactive sputter deposition to circumvent the hysteresis effect. Each group controlled the reactive gas partial pressure based on a different feedback signal: optical emission spectrometer (OES) signal, mass spectrometer and cathode voltage.

The biggest advantage of controlling the partial pressure of the reactive gas during a reactive sputtering process is that there is no forbidden region between the metal and poisoned states of the target, and an operating point can be chosen that optimizes both the desired film properties and the deposition rate. Figure 2.8 (b) shows the hysteresis shape for the reactive sputtering of metallic titanium in an argon/oxygen mixture atmosphere using oxygen partial pressure control of the oxygen. The transition region between the metallic state and the poisoned state is continuous. As the partial pressure of the reactive gas is increased, the amount of oxygen in the film increases, and the deposition rate decreases. There is an optimum operating point along this curve that maximizes both the deposition rate and the desired property of the deposited film.

Additionally, the hysteresis in the deposition rate and target erosion rate are shown in Fig 2.9. The target erosion rate and deposition rate have a significant decrease when the flow of the reactive gas reaches a sufficiently high level; however, when the gas flow of the oxygen is decreased, the target erosion rate and deposition rate do not return immediately to their previous values.

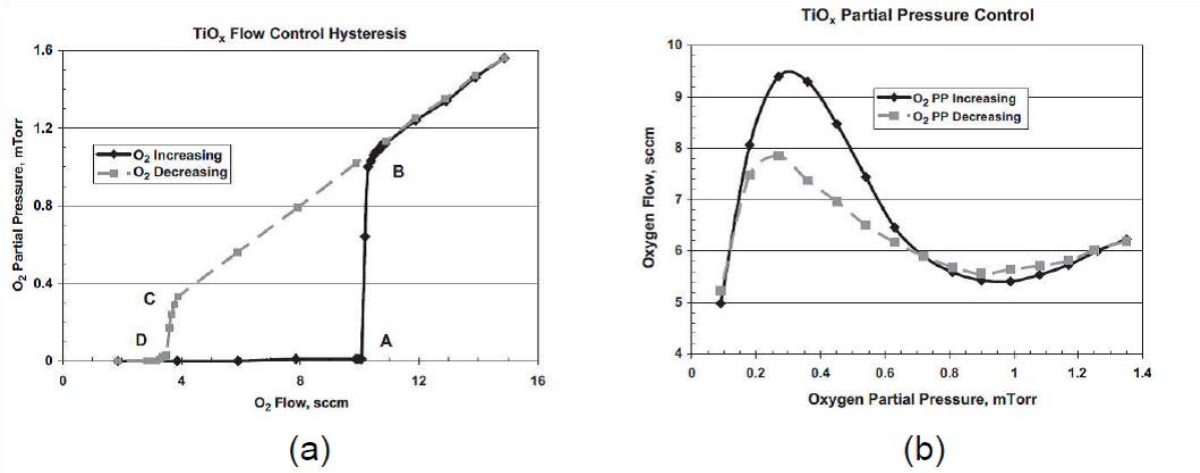

Figure 2.8 Typical experimental curves for a reactive sputtering process. (a) Oxygen partial pressure versus oxygen flow rate; (b) the hysteresis shape for the reactive sputtering of metallic titanium in an argon/oxygen mixture atmosphere using oxygen partial pressure control of the oxygen. Reprinted from [190], Copyright (2005), with permission from Elsevier.

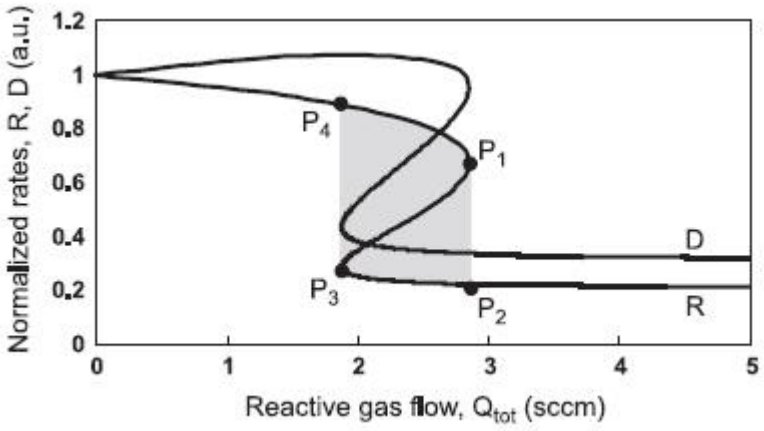

Figure 2.9 Calculated target erosion rate R and deposition rate D vs. total supply rate of reactive gas. Reprinted from [186], Copyright (2005), with permission from Elsevier.

The hysteresis in the cathode voltage is more complicated. First, when constant power is applied to the cathode (target), the change in cathode voltage is quite different depending on the control method of the reactive gas. For the reactively sputtered TiO_x system, the cathode voltage as a function of the oxygen flow when oxygen flow is the controlling variable is shown in Figure 2.10 (a). The cathode voltage initially increases as the oxygen flow rate is increased, but there is a

significant increase in the cathode voltage followed by a sharp decrease after 10 sccm, which points out that the target becomes poisoned. The cathode voltage remains high even when the flow is reduced after that. It is not decreased until the titanium oxide compound layer on the target surface is gradually removed, and then the cathode voltage returns to lower values corresponding to the metallic deposition mode.

However, in Figure 2.10 (b), the plot of cathode voltage as a function of the reactive gas partial pressure is quite different from the Figure 2.10 (a). The cathode voltage increases as the partial pressure increases for the TiO_x system, when the oxygen partial pressure is reduced, the cathode voltage also decreases, and the initial and final voltage values are nearly the same.

Secondly, for the different target material, the behavior of cathode voltage changing as a function of reactive gas partial pressure is also different. For a titanium-oxygen system, the cathode voltage increases as oxygen partial pressure increases. However, for the reactive sputtering of Al in an argon/oxygen atmosphere, the cathode voltage decreases as the partial pressure is increased.

Since the ion-induced secondary electron emission coefficient is usually much higher for compound mode than for metals, and Ohm's law suggests the plasma impedance is effectively much lower in poisoned mode than metallic mode, this effect is reflected in the lower cathode voltage when the target become poisoned. But Lewis [191] reported that an increase in the reactive gas partial pressure in the plasma could actually reduce the plasma density due to a subsequent reduction in the ionization collision cross section, which leads to an increase in the target voltage.

In the titanium-oxygen reactive sputtering process, the cathode voltage initially increases with increasing oxygen partial pressure, but as the oxygen continues to increase the cathode voltage falls. This indicates that initially there is a reduction in plasma density as the dominating factor controlling cathode voltage. As the reactive gas partial pressure continues to increase, the plasma density increases, and the increase in secondary electron emission for the titanium oxide compound takes over and thus lowers the cathode voltage; this phenomena is also confirmed by the experimental result of Mohamed et al. [62].

One very positive advantage for cathode voltage is that an arc can be detected by sensing a drop in the cathode voltage. When the compound forms on the surface of target, it can charge up and cause an arc. Arcs usually result in droplets being ejected from the target surface, and these droplets obviously degrade the deposited film quality. Nowadays, pulse dc power is used most frequently to overcome arc in reactive sputtering by using a voltage reversal at the cathode to offset charge build up on the target surface during a negative pulse, which is the mode for sputtering, while during the positive pulse, electrons from the plasma are attracted to the target to discharge any charged regions. However, the film can eventually cover all surfaces in the chamber with pulsed dc reactive sputtering and cause a disappearing anode. This happens because this insulating compound film makes the electrons from the plasma not able to return to the power supply and thus the plasma will finally extinguish.

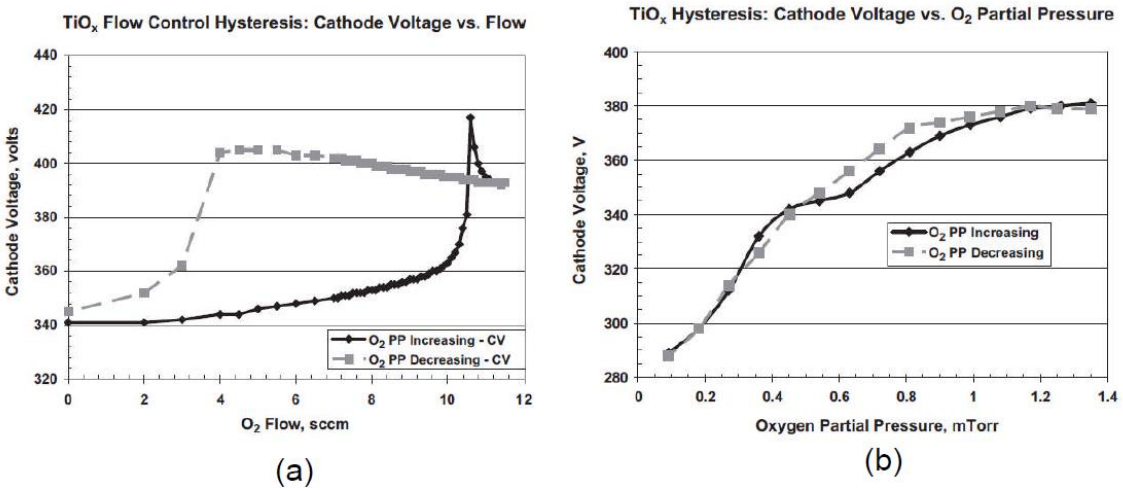

Figure 2.10 For the reactively sputtered TiO_x system. (a) The cathode voltage as a function of the oxygen flow when oxygen flow is the controlling variable; (b) The cathode voltage as a function of the oxygen partial pressure when oxygen partial pressure is the controlling variable. Reprinted from [190], Copyright (2005), with permission from Elsevier.

Moreover, Okamoto [192] showed in 1986 that it is possible to change the shape of the reactive gas flow/partial curve by increasing the pumping speed of the system. The hysteresis effect is reduced until eventually there is no hysteresis as the pumping speed of the system is increased, but it comes at a very high cost for the extra pumps to achieve this high pumping speed. In addition, the hysteresis can also be eliminated

by simply reducing the size of the target sputter erosion zone [193] , or using conductive substoichiometric targets [194] for which only a low amount reactive gas flow is required.

Chapter3
Experimental

3.1 Experimental system

In the work presented here, a high-vacuum (HV) system was constructed and used in order to enable highly flexible magnetron-based deposition of 2D and 3D nanocomposite coatings.

As depicted in Figure 3.1, the HV system consists basically of a main deposition chamber and some other affiliated parts. The main chamber is pumped via turbo molecular pump (Pfeiffer TMU 260) backed-up by an oil-free scroll pump (Varian SH-110). The pressure of the main chamber is measured by MKS Baratron capacitance manometer. The base pressure in the main chamber is less than 10^{-6} Pa for all deposition experiments. The main chamber houses the sample holder and DC magnetron for Ti and RF magnetron for Ag as shown in Figure 3.2.

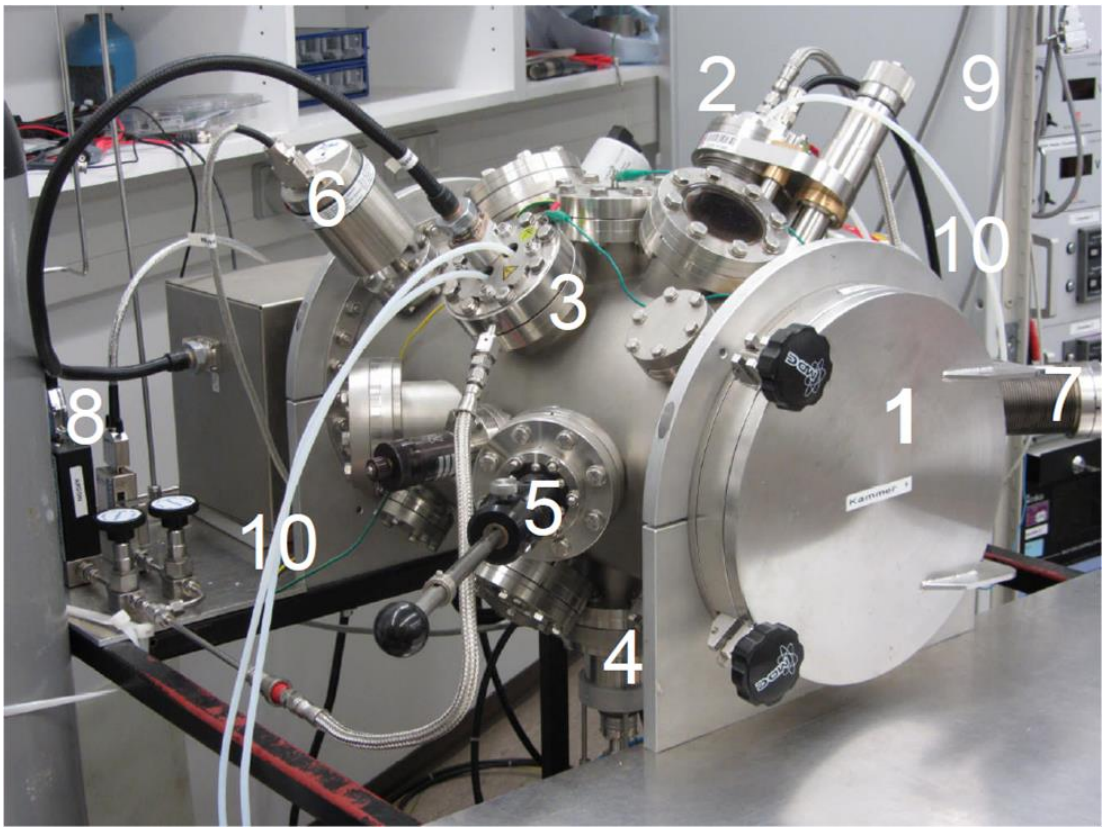

Figure 3.1 Deposition system constructed in the course of the presented work.

1- main chamber	5- sample shutter	9- electronics rack
2- DC magnetron	6- Baratron (MKS)	10- water cooling tubes
3- RF magnetron	7- QCM transfer rod	
4- sample holder	8- gas flow controllers	

The sample holder is rotatable to ensure uniform deposition and it is mounted electrically disconnected to the chamber. Therefore, deposition can be conducted with the sample being either grounded or biased. The substrate plate (35 mm diameter) can be heated up to 1000K by a resistively heated Ti filament.

The angle of magnetrons were 50 ^{o}for both the Ti source and Ag source, and the distance between the Ti source and the substrate and the Ag source and the substrate were 6 cm and 12 cm, respectively. The DC magnetron for Ti source here is mounted on a manipulator which allows for variation of the target-substrate distance, increasing the flexibility of the system. In case of the desired morphology of Ag/TiO_x nanocomposites, this deposition geometry ensures the homogenous growth of 2D and

3D models. The process gas Ar and O_2 can be introduced into the chamber via a four-channel gas flow controller (MKS) at flows of $\phi_{Ar} = 2 - 200$ sccm and $\phi_{O_2} = 0.4 - 20$ sccm.

Additionally, a quartz crystal microbalance (QCM200 controller with crystal oscillator, Stanford Research Systems) can be used in the main chamber in order to monitor the TiO_x deposition rate. The operation temperature of the QCM is stabilized by water cooling to prevent errors due to thermal drift of the oscillator's resonance frequency. DC and RF magnetrons are water-cooled with an autonomous water-air chiller.

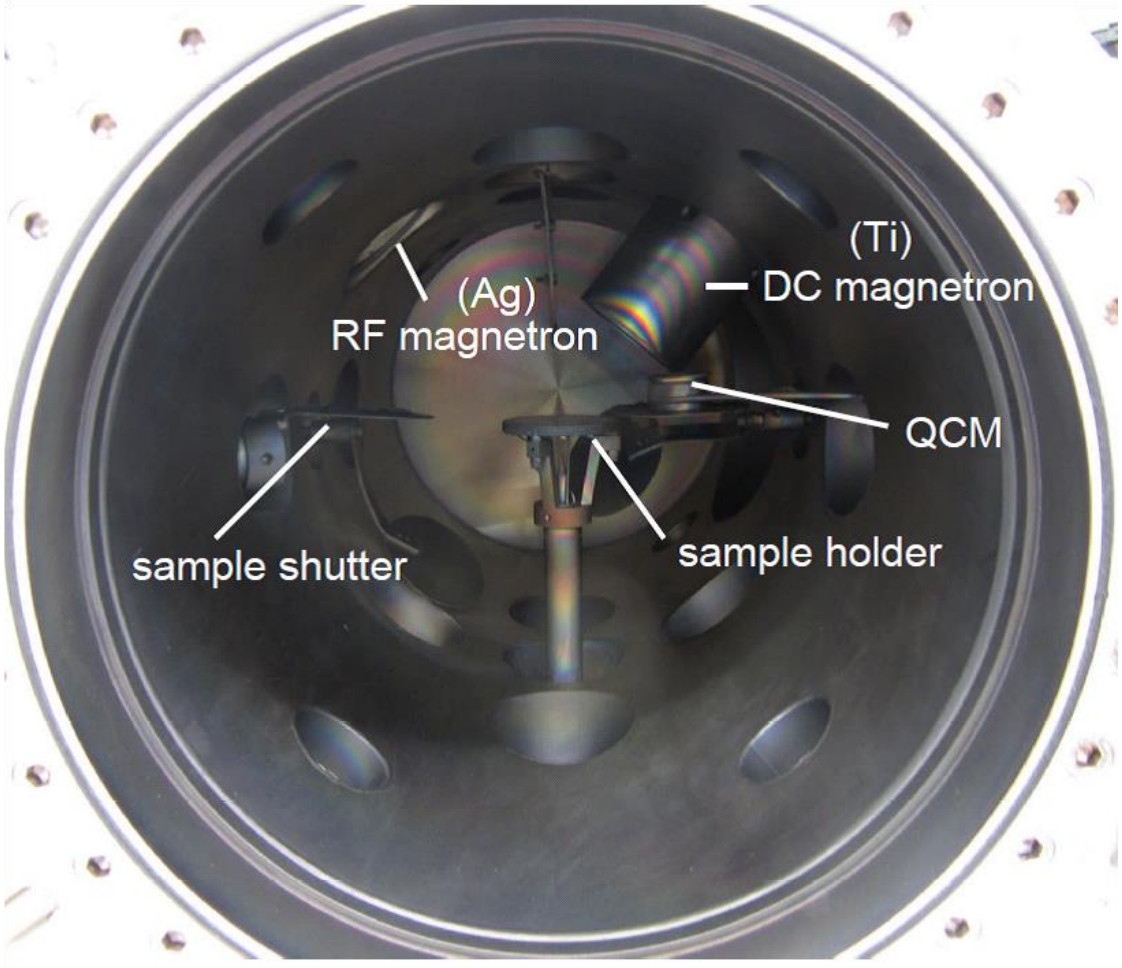

Figure 3.2 Front view of the open main chamber

3.2 Sample preparation

3.2.1 3D nanocomposite thin films

The nanocomposite coatings were prepared on flat quartz (1 cm x 1 cm) and silicon (0.5 cm x 0.5 cm) substrates, as well as on carbon-coated copper TEM grids in a home-made deposition vacuum chamber by reactive co-sputtering from a Ti target (99.99%, Goodfellow GmbH) and a Ag target (99.99%, Goodfellow GmbH) from two independent magnetron sources. The deposition chamber was evacuated to a pressure of 10^{-6} mbar prior to deposition. Pumping was done by a rotary pump (Varian SH 110) in combination with a turbo molecular pump (Pfeiffer TMU 260). Gas mixture of argon and oxygen was injected with constant flux ratio of 60:1, corresponding to total pressure of 1.17 Pa (2 sccm O_2), 0.45 Pa (0.75 sccm O_2) and 0.15 Pa (0.25 sccm O_2), respectively. Ti target was sputtered by a DC planar magnetron source (ION'X 2UHV, Thin Film Consulting) and the Ag target by a RF magnetron source (ION'X 2UHV, Thin Film Consulting). The input power of Ti magnetron varied from 25 W to 90 W and the input power of Ag magnetron was in the range of 6 W to 30 W. The distance between the Ti source and the substrate and the Ag source and the substrate were 6 cm and 12 cm, respectively. The angles of incidence were 50 ^{o} for both of Ti source and Ag source. Both continuous and independent monitoring of the deposition rates of the Ag and TiO_x were done in situ by using the two quartz-crystal monitors. The deposition rates were monitored independently for Ag and Ti with quartz-crystal microbalances and by variation of the power applied to the magnetron sources the silver metal volume fraction (MVF) was controlled. The sample holder was rotated throughout the deposition process to achieve uniform and homogenous deposition on all the samples mounted on the sample holder. First, a titanium oxide buffer layer with a thickness of 10 nm was deposited to increase adhesion strength and relax the stress between substrate and coatings [195]. After that, the silver containing titanium oxide nanocomposite (30 nm in thickness) was fabricated with the rotation rate of a substrate holder at a constant

rate of 9 rpm. Note that thicker films of around 200 nm were also prepared and showed the same surface morphology. The deposition rate of TiO_x matrix always remained around 6 nm/min, and the Ag deposition rate varied for different MVF. For further study on barrier thickness, a varied titanium oxide in different thickness (0 nm-60 nm) with different deposition rates were produced for adjusting silver ion release and morphology. The process is referred to as in-situ method and is depicted in Figure 3.3. The thickness of the coating was determined by using a surface profilometer (Dektak 8000) on a silicon substrate. Considering elevated temperature would risk increasing the Ag particle size and cause agglomeration, the experiments were all performed at room temperature conditions.

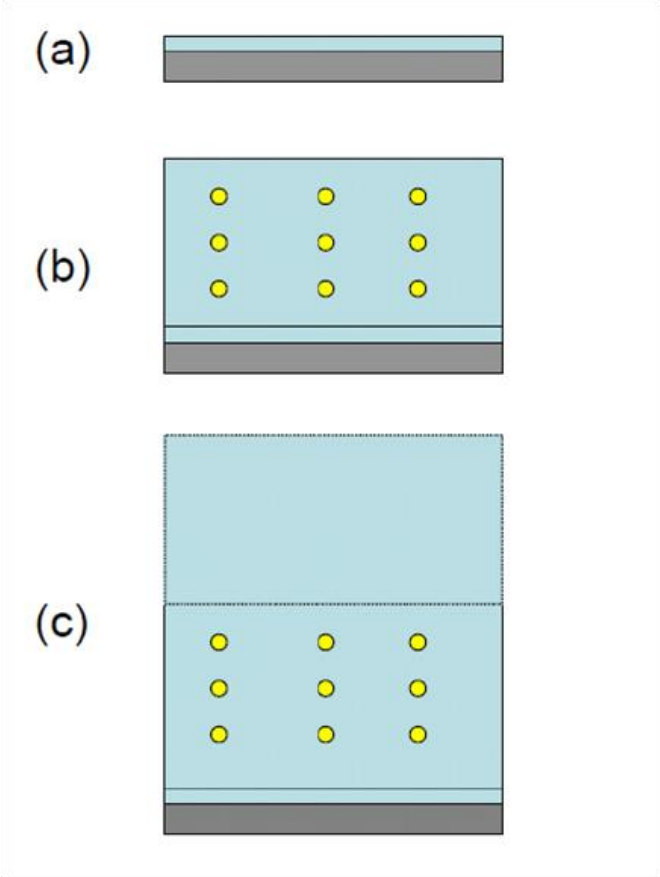

Figure 3.3 Schematic representation of the fabrication of 3D silver-containing nanocomposite. (a) deposited a TiO_x buffer layer on Si/quartz substrate; (b) co-sputtered 3D Ag/TiO_x nanocomposites; (c) then cover with a TiO_x barrier.

3.2.2 2D nanocomposite thin films

The 2D models were prepared by a discontinuous process named ex-situ method. The chamber was evacuated to a low base pressure (about $4*10^{-6}$ mbar), then10 nm titanium oxide buffer layer were prepared by DC reactive sputtering as already described above. After that, 2 nm Ag layer were deposited by RF sputtering technique on the buffer layer in pure Ar atmosphere(120 sccm Ar, 1.15Pa) with 10 W power(around 1 nm/min). Later on, the 2 sccm oxygen flow was introduced again to produce 10-50 nm capping layer with different deposition rate to investigate the surface segregation and silver ion release property. The process is referred to as ex-situ method and is depicted in Figure 3.4.The deposition rate was calibrated and the thickness of the film was monitored by a quartz-crystal microbalance and profilometer.

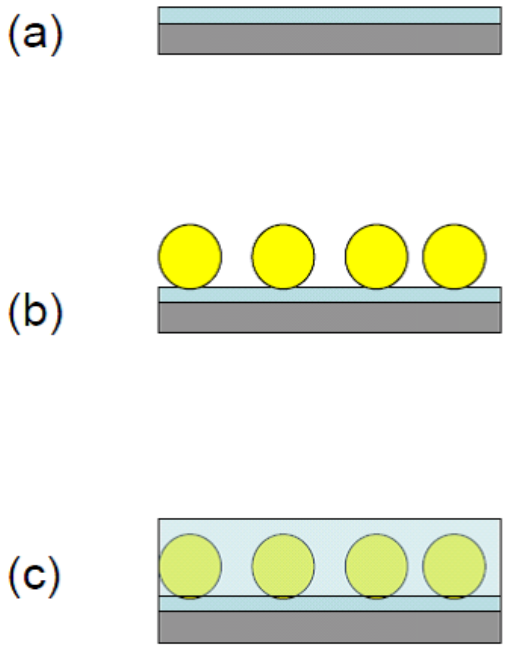

Figure 3.4 Schematic representation of the fabrication of 2D silver-containing nanocomposite. (a) Deposited a TiO_x buffer layer on Si/quartz substrate; (b) deposited 2 nm nominal Ag nanoparticle layer with pure Ar; (c) then cover with a TiO_x barrier.

3.3 Sample characterization

3.3.1 Scanning electron microscopy (SEM)

SEM is a type of electron microscope that produces images of a sample by scanning it with a highly focused beam of electrons. The electrons interact with atoms in the sample, producing various signals that can be detected and that contain information about the sample's surface topography and composition and other properties. The electron beam is generally scanned in a raster scan pattern, and the beam's position is combined with the detected signal to produce an image. However, SEM also presents many other advantages over traditional light microscopy such as improved resolution capacities, high depth of focus and simplified interpretation of the images and preparative work, etc.

When the primary electron beam scans the sample surface, depending on the material and acceleration voltage, secondary species are created in a so-called interaction volume that can be used for imaging and analysis. The signal used most frequently for the creation of images are the secondary (SE), backscattered electrons (BSE) and X-rays as well as depicted in Figure 3.5. The SE signal is most commonly used for imaging mode and derives its contrast primarily from the topography of the sample. These electrons have low energy and are easily influenced by voltage fields. The BSE signal is caused by the elastic collision of a primary beam electron with a nucleus within the sample.

In addition, materials are often identified by using the generated X-rays that are analyzed using a combined energy dispersive X-ray spectrometer (EDX). X-rays are emitted which are characteristic in energy for the constituent chemical elements. A histogram of the X-ray intensities versus their energy called an X-ray spectrum enables not only the identification but also the quantification of the chemical elements present in the specimen. EDX has served as a powerful tool for the determination of the metal-volume-fraction (MVF) and the local atomic concentration of metal atoms in the composite thin films. This has been done by comparing it with a standard

metallic film of the known comparable thickness. In this work, SEM measurements were performed using SEM (Zeiss Supra 55VP).

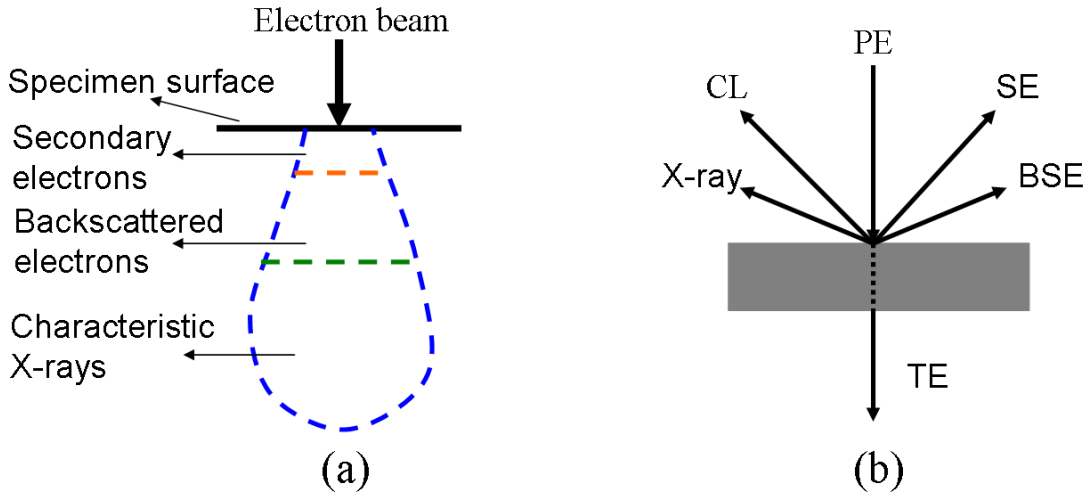

Figure 3.5 Schematic representation of the electron-specimen interaction in a SEM. (a) the tear-drop model of the electron interaction volume and the volume/depth from which the different signals originate; (b) Various signals generated as a result of electron beam interaction with a solid (left panel).

3.3.2 Transmission electron microscopy (TEM)

TEM is an electron microscopy technique whereby a beam of electrons is transmitted through an ultra-thin specimen, interacting with the specimen as it passes through. An image is formed from the interaction of the electrons transmitted through the specimen. TEM consists essentially of three parts, the electron gun where the beam is generated, electromagnetic lens system, sample holder and imaging system. The electron gun emits almost monoenergetic electrons with small wavelengths that are directly correlated with the spatial resolution. Therefore, specimens have to be thin enough to allow for transmittance of electrons. While the electron transparency is a function of electron energy and atomic number of the sample, the sample is

typically required to be thinner than 100 nm. For atomic resolution imaging, a specimen thickness even below 10 nm might be necessary.

The image quality depends on the imaging mode, which could be divided into bright field and dark field. In the bright field imaging, an aperture is placed in the back focal plane of the objective lens that allows only the direct beam to pass, then the image results from a weakening of the direct beam by its interaction with the sample. By using the occlusion and the absorption of the electrons, contrast is formed in the sample image. Regions with lower diffracted potential appear dark in this bright field imaging depending on the structure factor of the specimen. Thick areas or areas in which heavy atoms are enriched and crystalline areas appear with dark contrast. In dark field imaging, one or more diffracted beams are allowed to pass the objective aperture because the direct beam is blocked by the aperture. Since diffracted beams have strongly interacted with the specimen, enough information about particle sizes, stacking faults and planar defects can be obtained.

In addition to real-space imaging, the short wavelength allows for crystallographic investigations by electron diffraction. An advantage of TEM compared to other diffraction techniques, such as XRD, is the ability to probe a specimen's crystallography locally, down to the nanometer range. Accordingly, one refers to selected area electron diffraction (SAED), which is a useful tool here to figure out the chemical form of silver NPs. The same advantage holds for nanoprobe EDX which can be performed by TEM with lateral resolution in the nm-range.

All TEM measurements and analyses presented in this thesis were performed by U. Schürmann from the group of Prof. Kienle. The investigation was conducted with a Tecnai F30 G2 STwin. For the study of the individual Ag NPs, carbon-coated Cu-microgrids (S160-3, Plano) were analyzed using a Tecnai F30 G^2 microscope working at an accelerating voltage of 300 kV. Scanning (S)TEM images displaying atomic number dependent (Z)-contrast were recorded with a high angle annular dark field detector. For cross-sectional TEM investigations, lamellae specimens were prepared by focused ion beam (FIB) milling using a lift-out method with a FEI Helios

Nanolab system. The lamellae produced by FIB cutting were characterized via TEM using a Tecnai F30 STwin microscope (300 kV, field emission gun (FEG) cathode, spherical aberration coefficient C_s=1.2 mm). For EDX analysis, a Si/Li detector (EDAX System) was used. In addition, crystallography was probed locally by selected area electron diffraction (SAED).

3.3.3 X-ray photoelectron spectroscopy (XPS)

XPS is the most common technique for quantitative chemical state analysis of surface because of its relative simplicity in use and data interpretation [196]. It was developed in the research group of Kai Siegbahn for the chemical analysis of gas molecules and is also known as Electron Spectroscopy Chemical analysis (ESCA). With the development of ultra high vacuum (UHV) technology, XPS became suitable for the analysis of solid surfaces. XPS spectra are obtained by irradiating a material with a beam of X-rays while simultaneously measuring the kinetic energy and number of electrons that escape from the top 1 to 10 nm of the material being analyzed. It can detect all elements with an atomic number of 3 (lithium) and above. The reason it cannot detect hydrogen and helium is the binding energy of these electrons is quite small compared to the excitation energy of the x-ray photon and hence the absorption efficiency is very small.

Basically, when a solid surface is irradiated with X-rays, photon electrons are emitted due to the photoelectric effect, hence the energy spectrum of these electrons yields information about the initial state of those electrons and therefore about the chemical composition of the irradiated solid as shown in Figure 3.6. The core electron is excited by photon with energy hν, if the excitation energy is great enough; the electron is ejected from the atom with a well defined kinetic energy E_k. The atom is left in an excited, ionized state with a hole in its electron shell, thus the binding energy E_B of the electron can be calculated with respect to the Fermi level by

$$E_{B=} \text{ hν } -E_{k-} Ø \qquad (3\text{-}1)$$

where h is Plank constant, v is frequency of the radiation, E_k is the kinetic energy of the electron as measured by the instrument, Ø is the work function of the spectrometer (not the material).

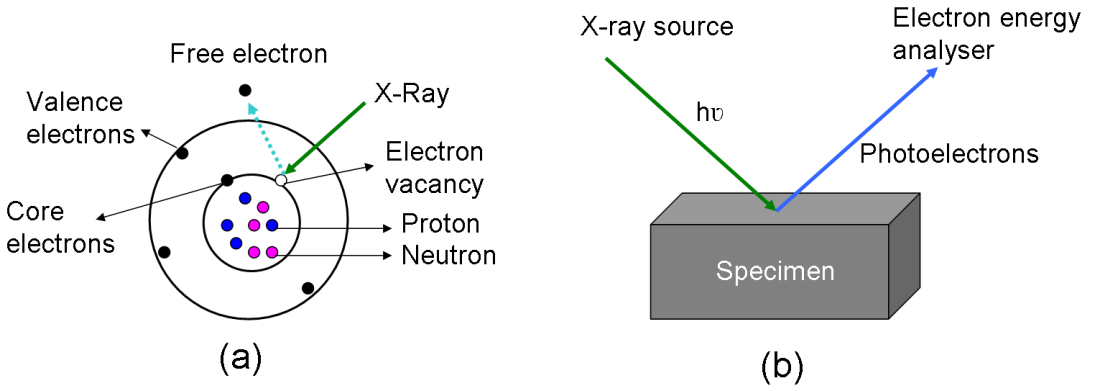

Figure 3.6 (a) The interaction of X-ray and irradiated atom when XPS works; (b) schematic illustration of XPS.

The binding energies can be determined from the line positions and the elements present in the sample identified; the plot has characteristic lines for each element found in the surface of the sample. Besides the photoelectron lines we can find the lines in the electron energy spectra which are due to the Auger effect; when the core electron leaves a vacancy, an electron of higher energy will move down to occupy the vacancy while releasing energy by photons or Auger electrons, each Auger electron carries a characteristic energy that can be measured. The exact binding energy of an electron depends not only upon the level from which photoemission occurs, but also upon: (1) the formal oxidation state of the atom and (2) the local chemical and physical environment. These give rise to small shifts (< 5 eV) in the peak positions in the spectrum, so-called chemical shifts. Usually species with a higher electron density or valence state are shifted towards lower binding energy. And an increase in oxidation state causes the binding energy to increase due to a decrease in the screening of the bound electron from the ionic core. The ability of XPS to determine oxidation states is used extensively in catalysis research.

All XPS measurements here were performed with XPS full lab (Omicron Nanotechnology GmbH), under ultra high vacuum analytical chamber of a vacuum about 10-9 mbar. Our XPS setup consists of a magnesium/aluminum twin anode X-ray source (VG Microtech XR3E2), hemispherical electron analyzer (VSW Instruments EA 125, a detection system and a data analyzer. The Al anode was operated at a typical power of 266 W (14.8 kV, 18 mA). The line position and intensity of the elements (Ag, Ti and O_2) in XPS spectra were measured and compared by other typical spectra shown in the handbook of X-ray photoelectron spectroscopy [197].

3.3.4 X-ray Diffraction (XRD)

XRD is an analytical method used for determining the atomic and molecular structure of a crystal, in which the crystalline arrangement of the atoms cause a beam of X-rays to diffract into many specific directions. English physicists Sir W.H. Bragg and his son Sir W.L. Bragg developed a relationship in 1913 to explain why the cleavage faces of crystals appear to reflect X-ray beams at certain angles of incidence (θ) [198]:

$$n\lambda=2d\sin\theta \quad (3\text{-}2)$$

where *d* is the distance between atomic layers in a crystal (lattice planes), and λ is the wavelength of the incident X-ray beam; n is an integer. This observation is an example of X-ray wave interference, commonly known as X-ray diffraction as depicted in Figure 3.7.

By measuring the angles and intensities of these diffracted beams, a crystallographer can produce a three-dimensional picture of the density of electrons within the crystal. From this electron density, the mean positions of the atoms in the crystal can be determined, as well as their disorder, chemical bonds and various other information.

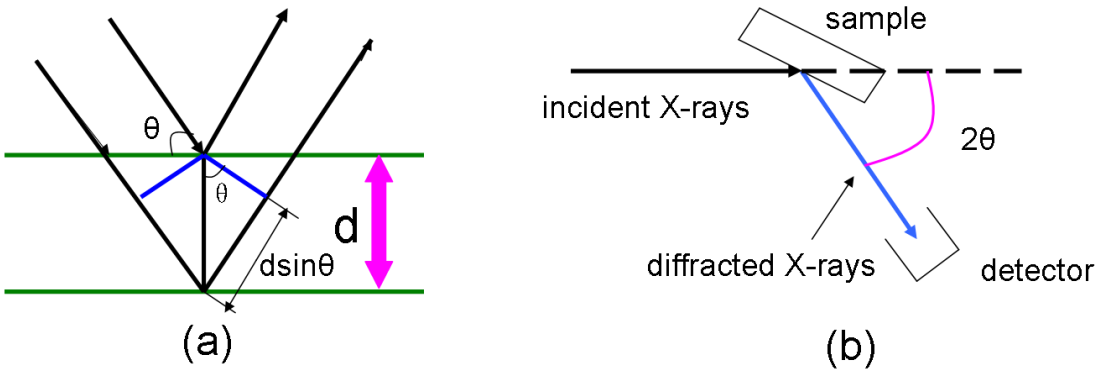

Figure 3.7 (a) X-ray wave interference; (b) principle and illustration of XRD

However, X-ray diffraction measurements of "thin" (1-1000 nm) films using conventional θ/2θ scanning methods generally produce a weak signal from the film and an intense signal from the substrate. One of the ways to avoid intense signal from the substrate and get stronger signal from the film itself is to perform a 2θ scan with a fixed grazing angle of incidence, popularly known as GIXRD. The fixed angle is generally chosen to be slightly above the critical angle for total reflection of the film material. It is used to study surfaces and layers because wave penetration is limited. Distances are on the order of nanometers. Below (typically 80%) the critical angle of the surface material studied, an evanescent wave is established for a short distance and is exponentially damped. Therefore Bragg reflections are only coming from the surface structure. An advantage of GIXRD is that the electric field at the critical angle is amplified locally by a factor of four, making the signal stronger. A disadvantage is the limited in-plane spatial resolution.

In this thesis, crystallographic properties of thin films were investigated with a Seifert XRD 3003 in 2θ (20 º70 º) and grazing incidence angle (5 º). The x-ray source provides Cu-K_ radiation (λ= 1.54 Å). The determination of Miller indices for the observed diffraction peaks is based on the ICDD database PCDFWIN, v.2.1 (2000).

3.3.5 Profilometer

A profilometer is a measuring instrument used on a surface's profile, in order to quantify its roughness and film thickness. A typical profilometer can measure small vertical features ranging in height from 5 nm to 800 μm [110]. In this technique, a diamond stylus is moved vertically in contact with a sample and then moved laterally across the sample for a specified distance and specified contact force. The height position of the diamond stylus generates an analog signal which is converted into a digital signal which is stored, analyzed and displayed. The horizontal resolution is controlled by the scan speed and data signal sampling rate. In this work a DEKTAK 8000 was used for our measurements. The radius of the diamond stylus was 12.5 μm and the stylus tracking force was factory-set to 50 mg.

3.3.6 Quartz crystal microbalance (QCM)

A QCM is used for in situ monitoring of the thickness of films deposited by physical vapor deposition techniques. A crystalline quartz is piezoelectric and initially oscillates at its natural frequency, which is typically 5 MHz [113]; 265-3500 serial of quartz from MDC company (Hayward, CA 94545) were selected in our chamber. As a material is deposited on the substrate, it is also deposited on the sensor. Depending on the density and the amount of the deposited material, the sensor's frequency will drop from its initial frequency. The rate and thickness can be calculated from this frequency shift. A conventional STM−100/MF quartz microbalance monitoring system was used in this work for film deposition monitoring. The calibration procedure is affected by three different parameters: material density, material Z-Factor, and tooling factor. The tooling factor is a deposition system geometry correction (location of sensor relative to the substrate), while density (gm/cc) and Z-Factor are material factors. Rate computation is based on the rate of the change of thickness readings, updated four times per second, and then filtered for display. Also the raw measured frequency of the sensor crystal is available from the instrument [135].

3.3.7 UV-Vis/NIR Spectroscopy

An ultraviolet, visible and near infra red (UV-Vis/NIR) spectroscope is the instrument which is used to measure the intensity of light before and after passing through a sample; the ratio of one to the other is named transmittance and is expressed as a percentage, and absorbance can be calculated from the value of transmittance. The transmittance T can be defined as:

$$T = \frac{I}{I_0} \tag{3-3}$$

where I_0 is the intensity of the incident light and I is the intensity of the transmitted light. In parallel, the absorbance A can be described by the transmittance:

$$A = -\log_{10} T = -\log_{10} \frac{I}{I_0} = \varepsilon cd \tag{3-4}$$

where ε is the molar extinction coefficient, c is the concentration of the absorbing species, and d is the path length through the sample, this is also named Beer-Lambert law.

The typical spectral range of the spectroscope is generally from 185 nm to 3300 nm. Absorption measurements can be at a single wavelength or over an extended spectra range. Since there is a linear relation between absorbance and concentration of the absorbing molecules, this makes UV-Vis/NIR spectroscopy very useful for quantitative measurements of optical materials.

The minimum requirements of an instrument to study absorption spectra are shown below: the light source of radiation of appropriate wavelengths which is normally a deuterium lamp for UV measurements and a tungsten-halogen lamp for visible and NIR measurements; a monochromator and optical lens for isolating light of a single wavelength; sample handling for introducing the test sample into the light beam; a means of detecting and measuring the light intensity.

In this work, the optical properties of the Ag/TiO_x nanocomposites which were deposited on quartz substrates were characterized using Perkin Elmer Lambda 900 UV-Vis/NIR, with a deuterium lamp for UV measurements and a halogen lamp for visible and near infrared measurements and also two different detection systems: a photomultiplier in the UV and visible range and a lead sulfide detector for near infrared. Coatings are placed in a small masking apparatus in order to examine the specific area. It is important not to smudge or leave fingerprints on the curettes. This will cause scattering of the light and lead to erroneously high absorption values. Because silver NPs have strong surface plasmon resonances in the visible range of the electromagnetic spectrum, the absorption spectra of the Ag/TiO_x nanocomposites were recorded between 350-900 nm in absorption mode and pure quartz substrate was used as a reference sample to get rid of the effect of the substrate. Due to the small size of the silver NPs in our model system, the scattering was neglected and only absorption was considered.

3.3.8 Atomic absorption spectroscopy (AAS)

AAS is an analytical technique that measures the concentrations of elements. It uses the absorption of light to measure the concentration of gas-phase atoms. The analyte atoms or ions must be vaporized in a graphite furnace or flame, so the samples are usually liquids or solids. The atoms absorb ultraviolet or visible light and make transitions to higher electronic energy levels. Thus the technique makes use of the wavelengths of light specifically absorbed by an element. Consequently, an AAS needs the following three components: a light source; a sample cell to produce gaseous atoms; and a means of measuring the specific light absorbed. The concentration measurements are usually determined from a working curve after calibrating the instrument with standards of known concentration. Atomic absorption is so sensitive that it can measure down to parts per billion (ppb) of a gram in a sample. AAS can be used to determine over 70 different elements in solution or directly in solid samples employed in pharmacology, biophysics and toxicology

research. In this work, an AAS ZEEnit 600S (analytik jena AG) was employed with liquid samples at the Hygiene-Kiel trace analysis center/AAS Lab, University Hospital Schleswig-Holstein. The technique detection limit was μg/L for silver. All results are blank-subtracted averages of 3 replicate measurements. The analytical error as estimated from replicated sample measurements was less than 5% RSD (relative standard deviation) for silver concentration.

3.4 Silver ion release measurement

Since the Ag/TiO_x nanocomposite are quite sensitive to exposure to moisture and light as already mentioned before [119], all the prepared samples in the current experiments were stored in a vacuum and in a dark environment.

The silver-ion release measurements were performed by observing the ion concentration changes that occur as samples were immersed in 10 ml air saturated deionized water (PH=7, $\sigma = 0.06 \mu S/cm$ at 13 ℃) in small bottles made of high density polyethylene(HDPE) at room temperature for different time intervals. Samples which were deposited on Si were checked by XPS. Additionally, TEM measurements were carried out after immersion of the coated TEM grids in water for 7 days. The released silver ion concentration in water was checked by AAS. This was done by immersion of samples prepared on Si in deionized water and after a definite period (40min, 2h, 1d, 3d, 7d), 5 ml of the water was removed from the bottle to be analyzed by AAS and replaced with new 5 ml for the next measuring time point as shown in Figure 3.8. This procedure has been optimized as it has been found that removing all the water could affect the sample by exposure to atmosphere directly or could change the starting point conditions for the next time step as there were always saturated drops left on the sample surface or in the bottle. However, removing the sample from the water also has problems as this could damage the sample and the remaining drops coated on the surface would dry and change the surface conditions. The half-water removal method is a suitable method which already had been proven by my previous colleagues' work to protect the solution system; the system was not affected too much by manipulation and enough water solution to repeat the AAS

measurement several times. The calculation of cumulative ion concentration is mathematically straightforward since the remaining 5 ml water solution contained the same amount of silver ions as the 5 ml water that have been removed. One thing needs to be mentioned: the AAS could not distinguish Ag ions from Ag NPs, However, since our samples were immersed in pure deionized water with $PH = 7$, only oxidation of Ag is expected at this value [91]. Additionally, SEM and TEM images after immersion of samples in water for 7 days have shown that smaller Ag NPs disappeared from the surfaces and matrix, which indicates dissolution of the particles in water and thus ion release. No mechanical detachment of the Ag NPs is expected in our experiments due to this, which means larger Ag NPs would dissolve and disappear first instead of smaller particles in contrast to our observations and literature [119,199].

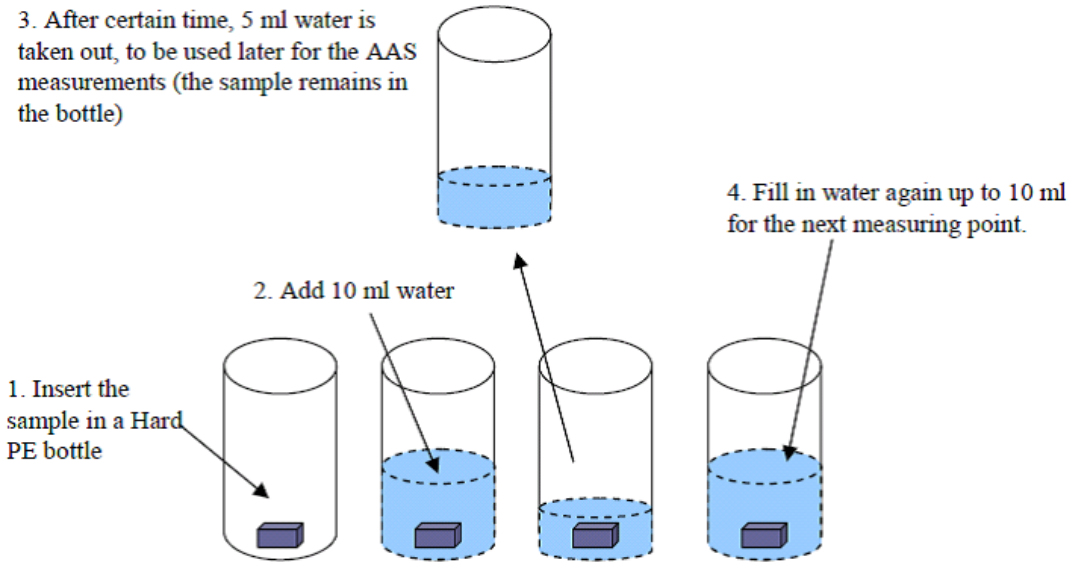

Figure 3.8 The performed half-water-change-method for AAS measurements.

Chapter 4

Surface segregation controlling in reactively sputtered Ag/TiO_x nanocomposites

In this chapter the silver surface segregation controlled by different deposition parameters in 2D/3D reactively sputtered nanocomposite coatings with varied filling factor and barrier thickness were investigated. The conditions were chosen to allow high deposition rates. Total sputtering pressures were selected above and below 1 Pa since similar pressures have been used frequently in typical reactive sputtering deposition processes. The study of the composites surface/bulk morphology was performed to understand the mechanism and kinetics of the surface segregation in these reactively sputtered films. The evolution of the silver NPs and the variation in the morphology of the 2D/3D nanocomposite coatings were examined by SEM, TEM and XPS. Moreover, the optical properties of the nanocomposites were studied by UV-Vis.

4.1 3D Ag/TiO_x nanocomposites

Magnetron sputtering has been widely used to prepare Ag containing nanocomposites due to its flexibility, simplicity in the combination of materials and tailoring in size distribution. Traditionally titania films have been prepared by non-reactively sputtering method (RF magnetron sputtering), however, considering the relative lower deposition rate, easy thermal-cracking and complex production of titania targets for RF magnetron sputtering, DC reactive magnetron sputtering has attracted intense interest since it not only provides controllable structures, sizes and morphologies, it also allows flexibility and forming films with controllable

stoichiometry. It is also straightforward to implement it in industrial-scale production for relative high deposition rates and large area coatings [200–202].

As described in previous content, constituent atoms of small surface free enthalpy in a multicomponent system have the tendency to accumulate at the surface to reduce the total free enthalpy of the system, therefore causing a localized enrichment of this material on the surface [162]. In the system of Ag/TiO_x 3D nanocomposites, Ag surface segregation can be understood due to the high cohesive energy of Ag NPs and the low silver-titanium oxide matrix interaction energy, which leads to high Ag atom mobility on the growing nanocomposite surface and thus to Ag aggregation whenever Ag atoms encounter each other [170]. Furthermore, recently it has been found that energetic oxygen ions with sufficient energy can modify the structure of the growing matrix during reactive sputtering of transition metal oxides, i.e. TiO_x. It can be attributed to the reactive plasma oxidizing the Ag NPs and results in the diffusion of silver atoms with oxygen ions onto the surface [157].

The surface/bulk morphology of Ag/ TiO_x 3D nanocomposite coatings is influenced by a wide range of deposition parameters. Therefore, suitable deposition parameters had to be chosen to produce the desired coating properties, the reactive sputtering process was developed in order to be compatible with co-deposition Ag/ TiO_x 3D nanocomposites. The total pressure, oxygen partial pressure and barrier deposition conditions have to be taken into account during the co-sputtering processes.

4.1.1 Total gas pressure

A series of SEM images in Figure 4.1 shows the surface evolution of Ag NPs in Ag/TiO_x 3D nanocomposite coatings prepared at 1.17 Pa (2 sccm O_2) flow rate as the amount of silver deposition is increased. Because of the higher secondary electron emission, silver will appear brighter than titanium oxide, therefore the white agglomerates on the surface are identified with silver. For (a) 9%, (b) 15% and (c) 30% silver containing nanocomposites, there was a clear tendency of Ag NPs size growth and aggregates as silver concentration increased, from tens of nanometers to several hundreds of nanometers when the Ag filling factor increased from 9% to 30%. Surface segregation is significantly reduced for silver filling factors below a silver

content of 9% in this 3D nanocomposite model. As more silver is deposited, the surface segregation become more severe, thus silver surface segregation is in particular important for high filling factors leading to the formation of very large particles.

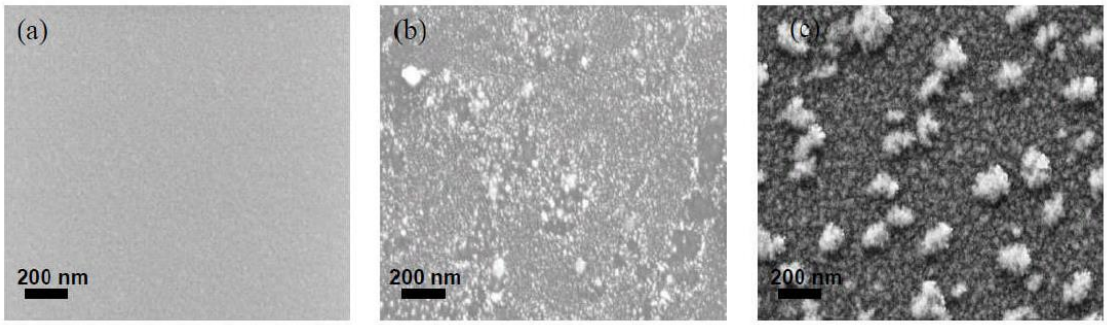

Figure 4.1 SEM images of the evolution of Ag nanoparticle distribution on the surface as the Ag filling factor is increased at 1.17 Pa (2 sccm O_2). (a) 9% Ag filling factor without barrier; (b) 15% Ag filling factor without barrier; (c) 30% Ag filling factor without barrier

Figure 4.2 shows that the X-ray photoelectron spectra of the evolution of Ag 3d core levels depends on the Ag filling factor during deposition at the surface (1.17 Pa, 2 sccm O_2). One can see clearly that the intensity of silver signal increased as the silver filling factor increased, which indicates more silver atoms diffused onto the surface leading to aggregation there. This is consistent with the results from the SEM images.

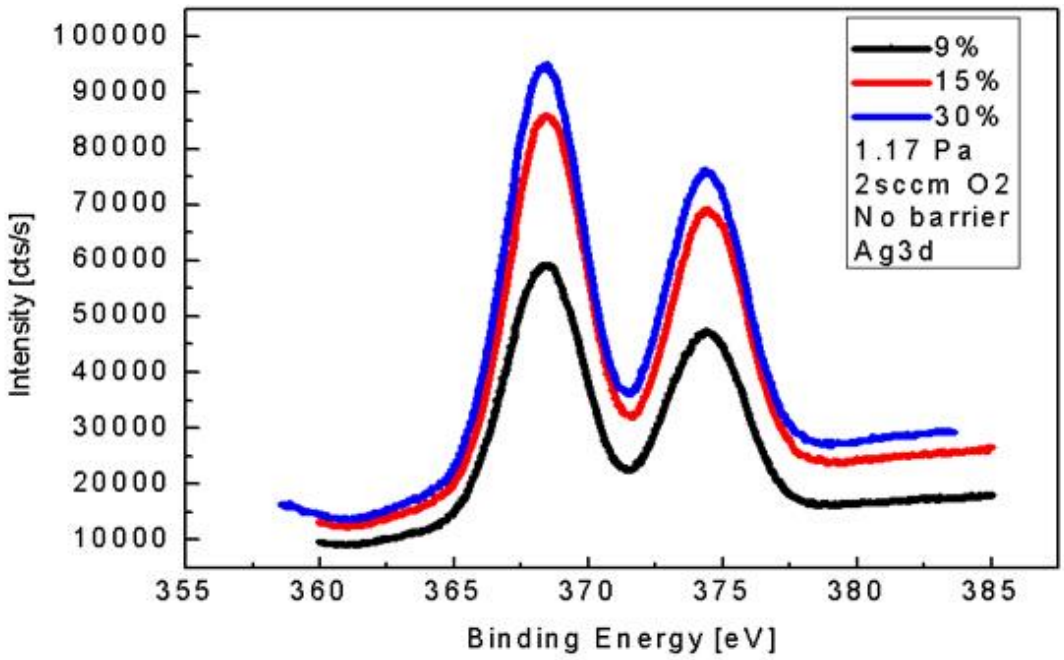

Figure 4.2 X-ray photoelectron spectra of the evolution of Ag 3d core levels depending on the Ag filling factor during deposition at the surface using 2 sccm O_2 at 1.17 Pa.

Figure 4.3 presents the STEM cross-sectional pictures and EDX measurement of the Ag NPs size distribution in the bulk with 9% and 15% Ag filling factor (1.17 Pa, 2 sccm O_2) which are consistent with the previous SEM results. One can see that most of the Ag NPs exist in the matrix for the 9% Ag containing nanocomposite from Figure 4.3 (a). The silver NPs hiding inside the bulk are rather small, all around 5-10 nm, and slight surface segregation is observed in this case; most Ag NPs are buried in the titania matrix as smaller sized NPs. However, very large and irregular Ag NPs can be found on the surface in the nanocomposite coating with 15% Ag filling factor from the Figure 4.3 (b), and more Ag NPs become aggregate in the matrix as the Ag concentration increased. A strong silver signal in the nanocomposite region and on the outer surface area is detected, which indicates that strong silver segregation to the surface occurred; the presence of a depletion zone is also detected. However, most of the silver is distributed within the matrix as very small sized NPs; even big clusters of around 40 nm diameter are formed near the outer surface. It is believed that the growth of the Ag NPs in the bulk would give rise to large compressive stress in the ceramic matrix, while on the surface the particles can grow unconstrained.

Furthermore, Figure 4.3 (b) shows the selected area diffraction pattern which has been indexed in agreement with the fcc lattice of the metallic silver state, as evidenced by the rings with diffuse intensity representing the various Miller planes.

(a)

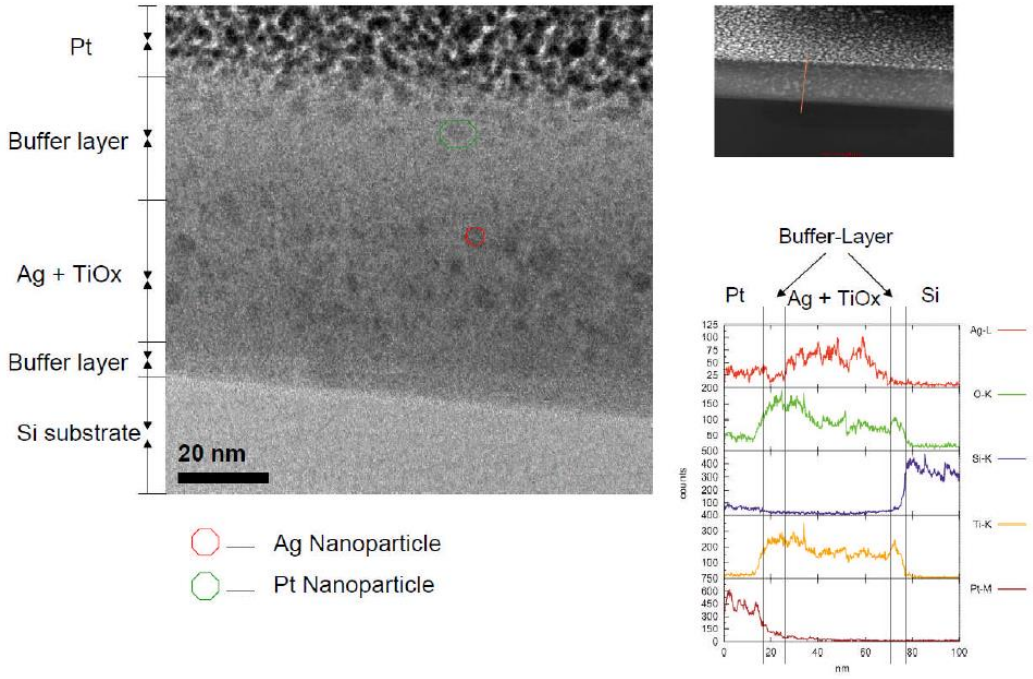

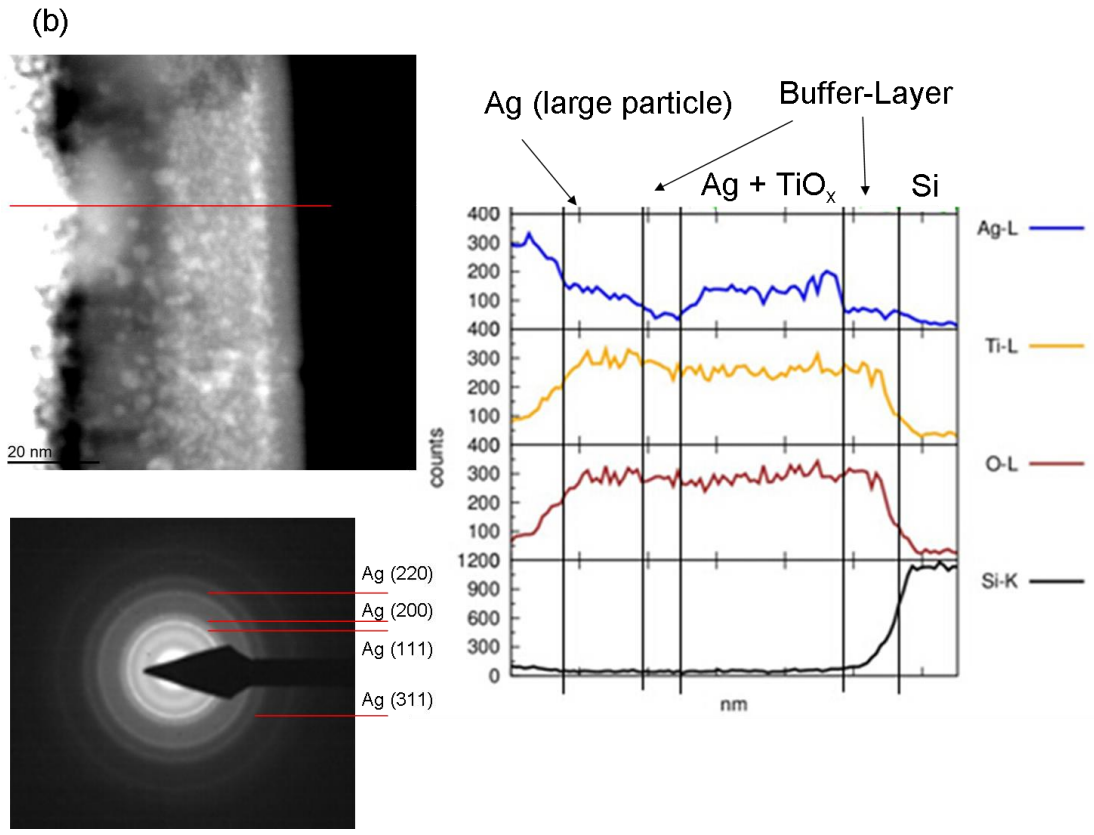

Figure 4.3 The STEM cross sectional images and EDX results of Ag NPs (black point we marked already) size distribution in the matrix and on the surface with different Ag filling factor (1.17 Pa, 2 sccm O_2). (a) 9% Ag filling factor; (b) 15% Ag filling factor

In addition, since the morphology and structure of the titanium oxide depends on the energy of deposited particles, more dense and rigid coatings can be expected by reducing the total gas pressure here. A series of SEM images in Figure 4.4 shows the surface evolution of Ag NPs in Ag/TiO_x 3D nanocomposite coatings prepared with 15% Ag filling factor as the total gas pressure is decreased. All the samples show surface segregation morphology even at 0.15 Pa, which is an extremely low total pressure. However, the Ag NPs distribution on the surface is quite different. A random and more agglomeration particle distribution existed on the surface when the total pressure is high (1.17 Pa), while a more regular round shape and smaller Ag NPs was on the surface when the total pressure is decreased to 0.45 Pa. Moreover, the density of Ag NPs on the surface was further reduced by decreasing the total pressure to 0.15 Pa, which indicated that the total pressure plays a very important role in

controlling the surface segregation in Ag/ TiO_x 3D nanocomposite coatings. Smaller size and well-distributed Ag NPs can be reached with very low total pressure, which is attributed to the much more dense titanium oxide matrix under the low total pressure [203]. An decrease in the total pressure would decrease the density of gas particles in the chamber and increase the cathode potential, which could strongly influence the probability of collisions and the acceleration of deposited particles and consequently the particle energy.

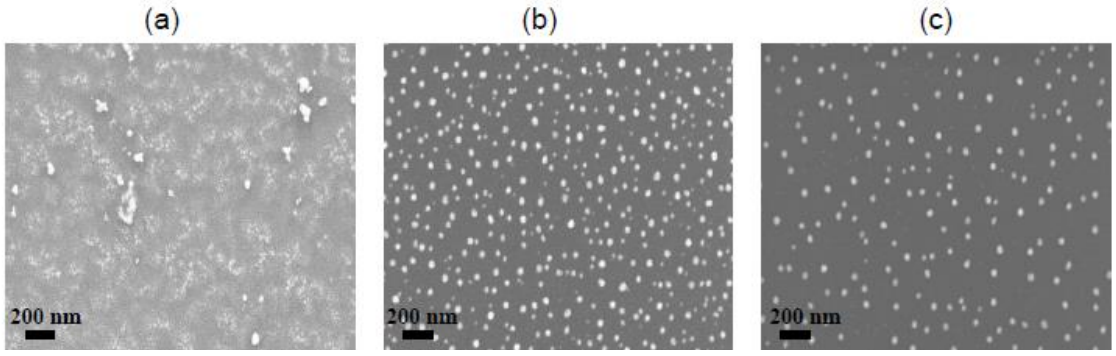

Figure 4.4 SEM images of the evolution of Ag NPs distribution on the surface of 15% Ag containing nanocomposites without barrier as the total gas pressure decreased. (a)1.17 Pa (2 sccm O_2); (b) 0.45 Pa; (c) 0.15 Pa

4.1.2 Oxygen flow rate

Because of the great influence of total gas pressure on the morphology of 3D nanocomposites, the influence of oxygen flow rate to the structure and surface morphology of 3D nanocomposites were also investigated at a relative high total pressure. However, oxygen flow rate was fixed as small as possible because silver oxide formation should be completely excluded in our case, because silver oxide could damage mammalian cells compared with metallic silver [127]. Therefore, one key point that should be noted in the reactive sputtering process is its influence on the chemical state of silver in the NPs formed inside.

Because the reactive sputtering process has oxygen admixed as a reactive gas, one point that needs to be addressed is its influence on the chemical state of the silver in the deposited nanocomposite. In the Grazing incident XRD image of Figure 4.5, it is clearly shown that the amorphous titanium oxide forms an fcc lattice structure of Ag NPs in the prepared nanocomposite coatings when the oxygen flow rate was fixed at 2 sccm (1.17 Pa). Even when the oxygen flow rate was increased to 19.2 sccm (Ar flow rate was still fixed at 120 sccm), no indication for Ag oxide formation is observed. It is reported that the formation of silver oxide is limited and only metallic silver NPs existed at the surface in reactive sputtering process due to the more stable thermodynamical state [204], and the diffusivity of titanium is 8-9 times higher than the diffusivity of Ag. Furthermore, Lai et al. [205] pointed out that Ag oxidation can only occur at oxygen partial pressure higher than 0.094 Torr at room temperature.

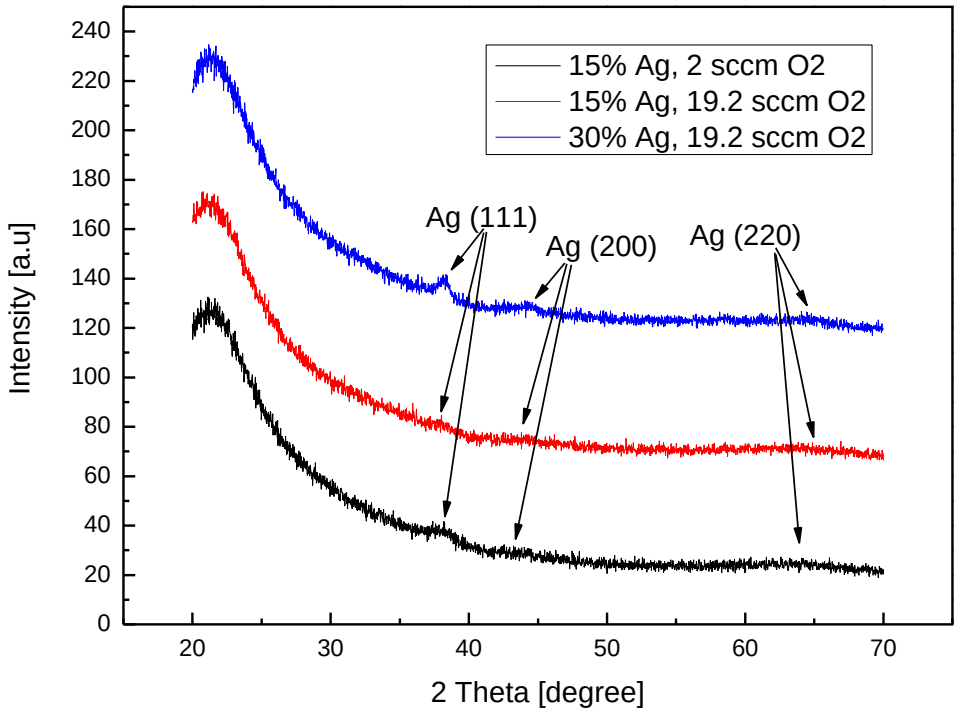

Figure 4.5 XRD patterns of 3D composites prepared at 2 sccm O_2 flow rate and 19.2 sccm O_2 flow rate, Ar flow rate were fixed at 120 sccm.

Figure 4.6 presents the SEM images of the evolution of Ag NPs distribution on the surface of 15% Ag containing nanocomposites without a barrier as the oxygen flow rate increased. In both micrographs it is clearly visible that Ag segregation onto the surface occurred, and larger aggregates can be seen on the surface, which was prepared in the 19.2 sccm O_2 atmosphere. The surface morphology evolution here indicates that the silver surface segregation can be induced under an excessive oxygen atmosphere. Recently it has been found that during the reactive sputtering of transition metal oxides, energetic oxygen ions with sufficient energy can modify the structure of the matrices; it can be assumed that the reactive plasma destroy the structure of silver film by oxidation of Ag and results in the diffusion of Ag atoms with oxygen ions [206–208].

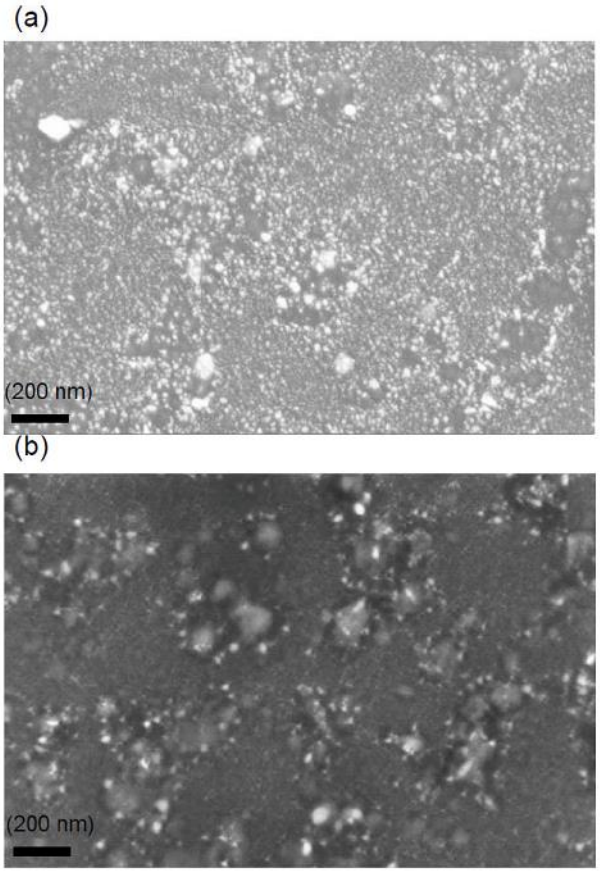

Figure 4.6 SEM images of the evolution of Ag NPs distribution on the surface of 15% Ag containing nanocomposites without a barrier as the oxygen flow rate increased. (a) 2 sccm O_2; (b) 19.2 sccm O_2

It is consistent with the result from Figure 4.7 which is the X-ray photoelectron spectra of the evolution of Ag 3d core levels depending on the oxygen flow rate during deposition at the surface. It clearly shows that the peak intensity of silver on the surface of nanocomposite film with 19.2 sccm O_2 is much stronger than the sample produced at 2 sccm O_2, which indicates that more silver atoms diffused onto the surface under the more oxygen-rich atmosphere, resulting in more silver surface segregation morphology.

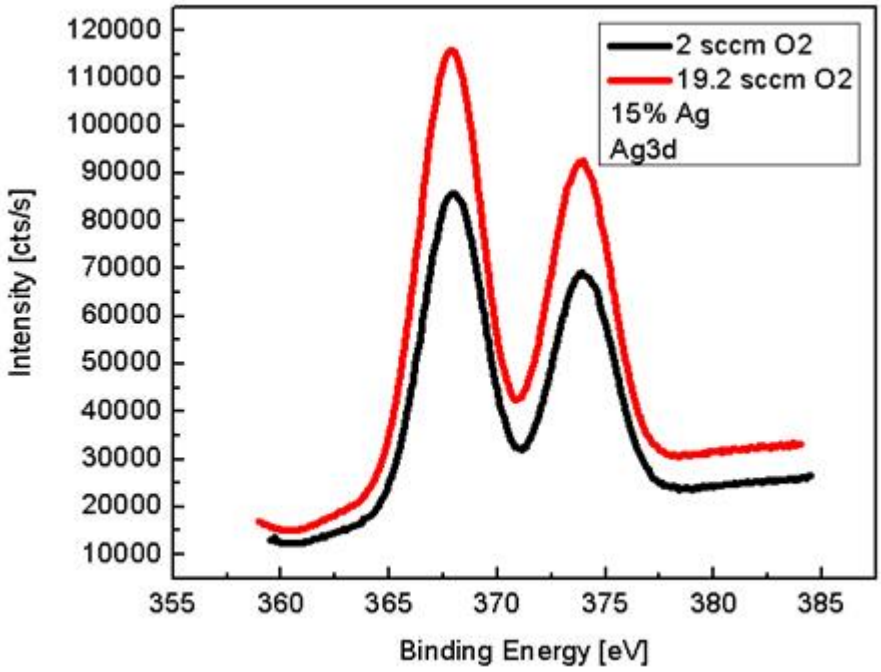

Figure 4.7 X-ray photoelectron spectra of the evolution of Ag 3d core levels depending on the oxygen flow rate during deposition at the surface

4.1.3 The barrier effect

Previous studies [209,210] suggested that Ag NPs segregation could be suppressed by depositing a capping layer of titanium oxide continuously via a RF sputtering method, and the Ag diffusion on the surface can be strongly retarded by a barrier thickness of some ten nanometers. However, we surprisingly found that coating a barrier at a moderate rate showed limited effect on suppressing the surface segregation at 1.17 Pa. This is totally opposite to the non-reactive method. Still, severe silver segregation happened on the surface even with a 60 nm barrier coating, and the particle size increased but the particle number decreased.

SEM images clearly show the surface morphology evolution barrier coated evenly at 1.17 Pa, in Figure 4.8. It is surprising to find that large surface segregation still existed even after a 30 nm and 60 nm barrier was coated, some silver clusters

become smaller and others become bigger, indicating that a titanium oxide barrier does not work to suppress the Ag segregation in reactive sputtering process.

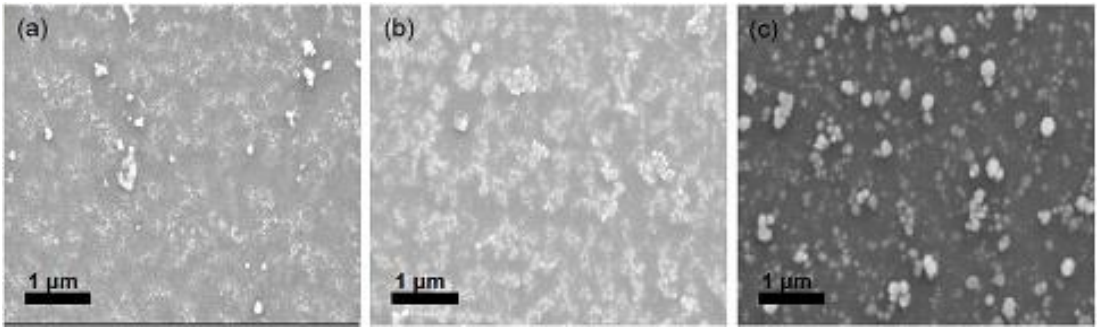

Figure 4.8 SEM images of the surfaces of nanocomposites prepared with the15% Ag filling factor and different thicknesses of TiO_x barriers at 1.17 Pa. (a) no barrier; (b) 30 nm barrier; (c) 60 nm barrier

Figure 4.9 shows the X-ray photoelectron spectra of the evolution of Ag 3d core levels depending on the barrier thickness during deposition onto the surface with a 15% Ag filling factor (1.6% O_2). The Ag intensity was decreased to 75% after a 30 nm titanium oxide layer was coated at a moderate rate, and only 44% intensity left after 60 nm TiO_x coated in the same way. This indicates that simply increasing the barrier thickness does not play a significant role in suppressing the Ag segregation on the surface; metallic silver still appears on the surface due to the Ag NPs diffusion and segregation that made different size Ag NPs with an associated decrease in the inter-particle distance and particle coalescence, which is consistent with the results that were observed from the SEM images in Figure 4.8.

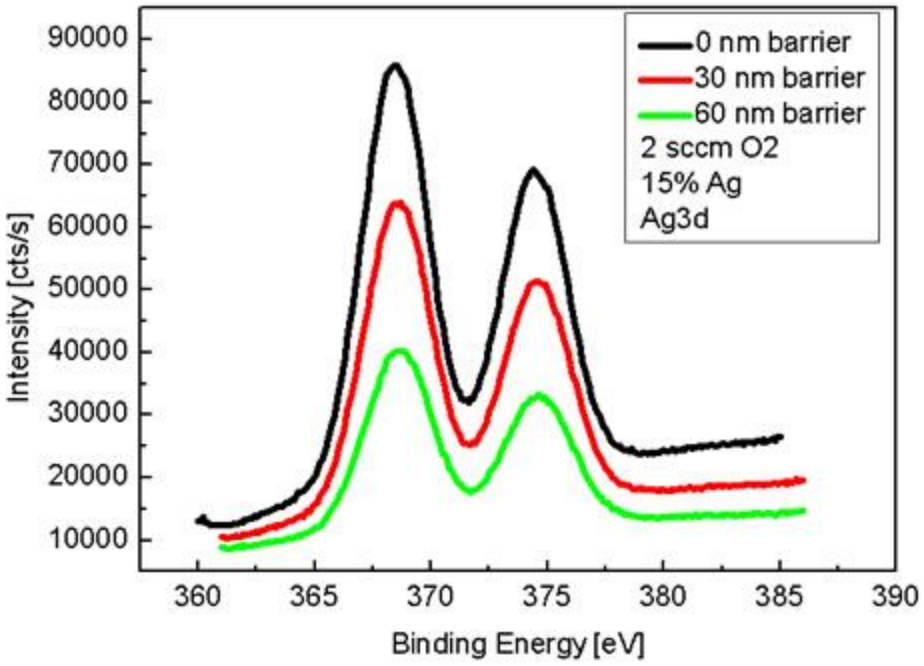

Figure 4.9 X-ray photoelectron spectra of the evolution of Ag 3d core levels depending on the barrier thickness during deposition at the surface at 1.17 Pa

Figure 4.10 shows the surface morphology evolution of nanocomposites with a 15% and 30% Ag filling factor that were prepared at 0.45 Pa. The surface segregation is still strong in both cases when no titanium barrier was coated but with more regular shape and size distribution compared with those produced at 1.17 Pa. However, the barrier layer shows a strong suppression effect in this case; we just switched off silver deposition and continued with reactive sputtering of titanium source, and no silver segregation on the surface after 30 nm barrier was coated, even when the Ag filling factor is 30%. Similar results are obtained when the total pressure was decreased to 0.15 Pa.

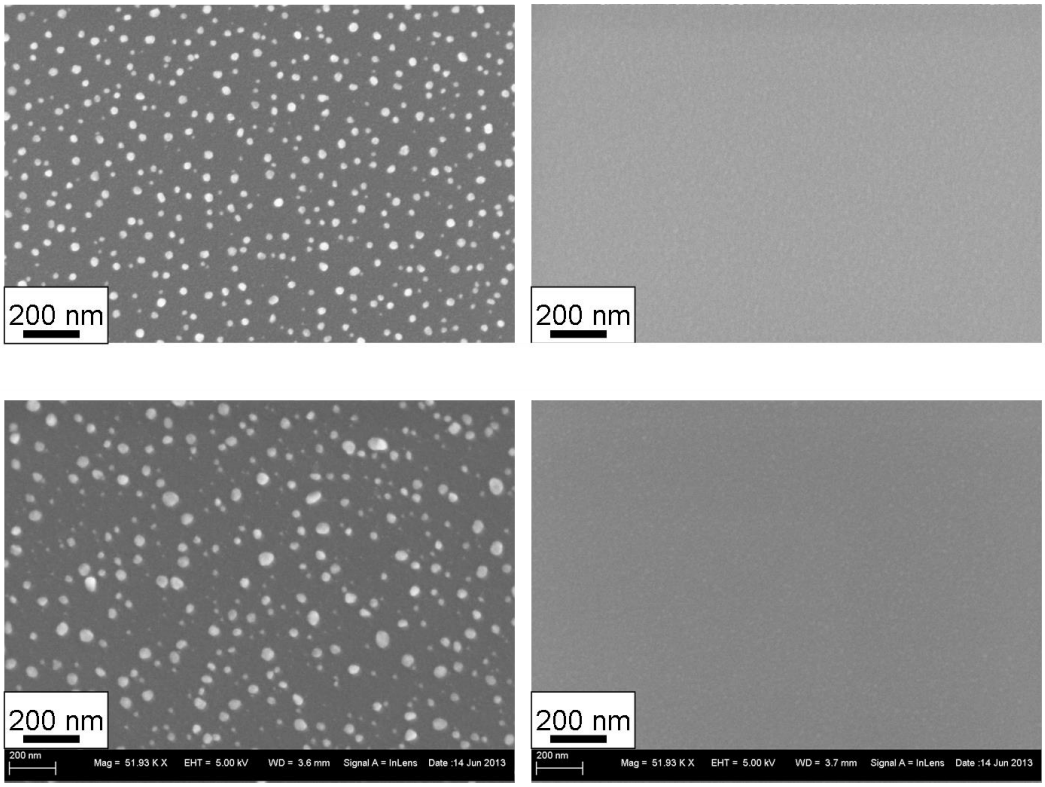

Figure 4.10 SEM images of the surface morphology evolution of nanocomposites produced at 0.45 Pa. (a) 15% Ag, no barrier. (b) 15% Ag, 30 nm barrier. (c) 30% Ag, no barrier. (d) 30% Ag, 30 nm barrier.

Figure 4.11 shows the X-ray photoelectron spectra of nanocomposite thin films with a 30% Ag filling factor coated with different barrier thicknesses at 0.45 Pa. One can see that the silver signals were not found at all above a 30 nm barrier coating, which indicated the titanium oxide barrier deposited at low total pressure has a perfect segregation controlling effect. We can find that only 3% silver signal was left after a 10 nm barrier was coated, and the intensity of silver signal on the surface reduced to 0.5% after depositing a 20 nm barrier; no silver signal was detected after a 30 nm barrier was coated.

In the reactive sputtering process, the microstructure and the surface morphology develop during the film growth, which is controlled mainly by the energy of depositing particles. When the energy of depositing particles decreases, the surface mobility decreases and the coalescence of crystals is limited. The depositing particles

are incorporated in the growing film at their impinging sites; high points on the growing surface receive more deposited material than valleys resulting in the formation of a more open microstructure and surface. An increase in the total pressure increases the density of gas particles in the chamber and decreases the cathode potential, which influences the probability of collisions and the acceleration of particles, and consequently the particle energy decreases. In contrast the oxygen partial pressure did not affect the surface morphology so markedly [203].

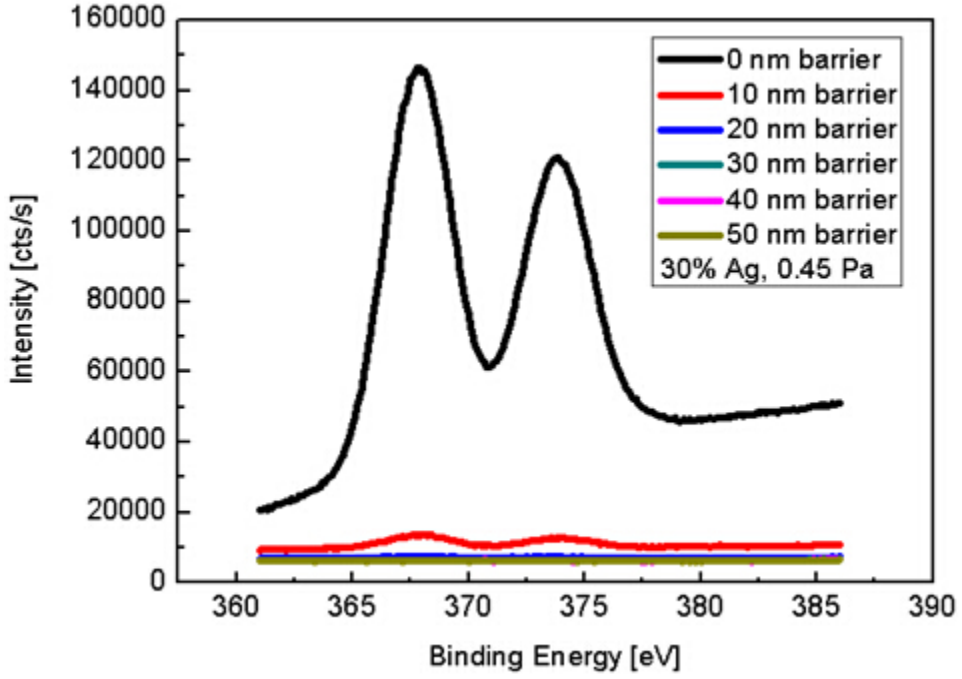

Figure 4.11 X-ray photoelectron spectra of the evolution of Ag 3d core levels depending on the barrier thickness during deposition at the surface using 30 % Ag filling factor and 0.45 Pa.

In addition, the influence of deposition rate for a titanium oxide capping layer was also investigated in this 3D model system at a relative high total pressure (1.17 Pa). Figure 4.12 shows the SEM images of the surface morphology evolution of 6% Ag containing nanocomposites coated with a 30 nm barrier produced at 1.17 Pa at high and moderate deposition rates. One can observe that the high deposition rate case (15 nm/min) in Figure 4.12 (a) presents a better surface segregation suppressing effect compared to the moderate deposition rate (6 nm/min) in Figure 4.12 (b),

indicating that a high deposition rate for a titanium oxide capping layer has a positive effect for suppressing silver surface segregation.

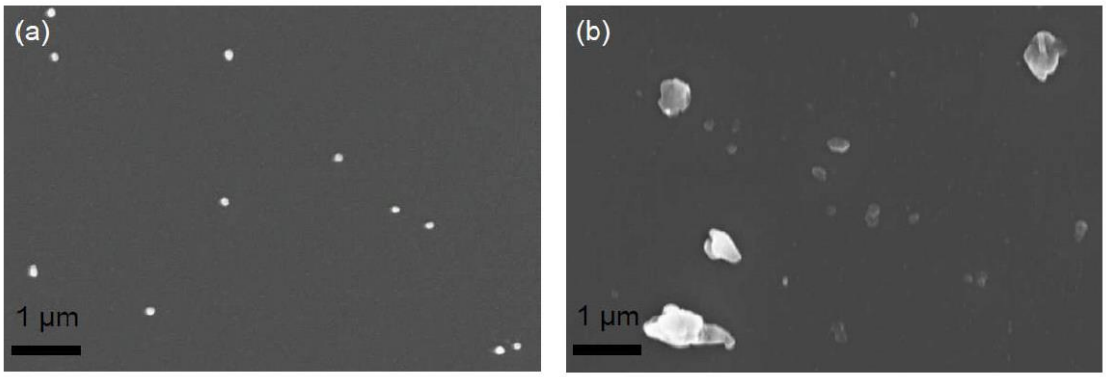

Figure 4.12 SEM images of the surface morphology evolution of 6% Ag containing-nanocomposites coated with 30 nm barrier produced at 1.17 Pa with different deposition rate. (a) High rate (HR). (b) Moderate rate (MR)

Figure 4.13 shows the TEM images of 6% Ag containing nanocomposites coated with a 30 nm barrier produced at 1.17 Pa with high and moderate deposition rates. One can see a more open structure of the titanium oxide matrix for the sample produced at a moderate deposition rate in Figure 4.13 (b) compared with the sample produced at a high deposition rate in Figure 4.13 (a). It is reported that the substrate temperature and deposition rate are among the chief variables affecting deposition rate. A lower deposition rate leads to a lower nucleation rate and an increase in the size of the critical nucleus. Also a discontinuous island structure is predicted to persist to a higher average coverage than at a high deposition rate. Therefore, it is clear that increasing the deposition rate for the titanium oxide capping layer results in smaller island structures which strongly changes the surface morphology evolution here [211].

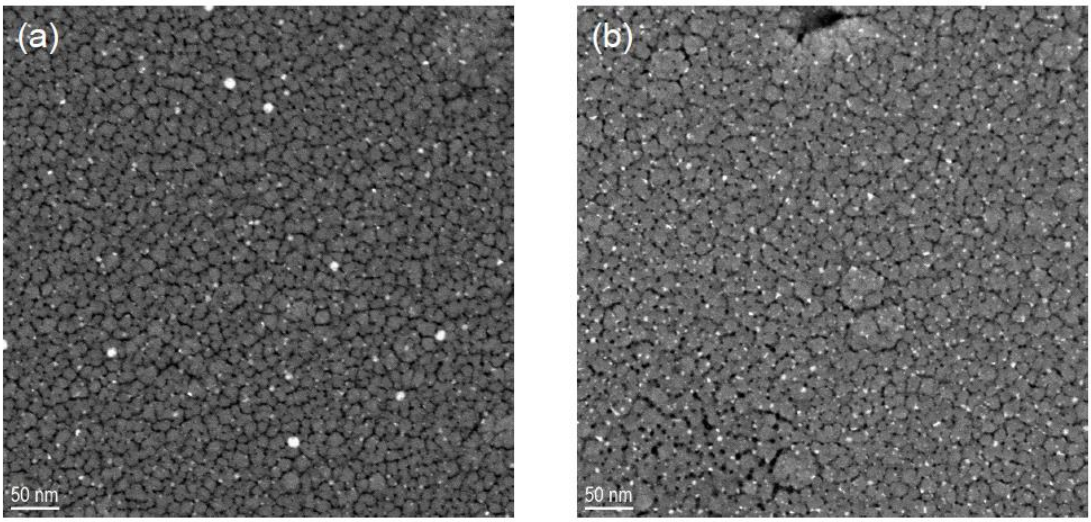

Figure 4.13 TEM images of 6% Ag containing- nanocomposites coated with 30 nm barrier produced at 1.17 Pa with different deposition rate. (a) High rate (HR). (b) Moderate rate (MR)

In Figure 4.14, the XPS result shows the silver surface segregation suppression effect when different deposition rates were applied. One can see that less silver signal was detected under the high deposition rate process when the barrier thickness was fixed at 30 nm. Only 44% silver signal was detected on the surface after a 30 nm barrier was coated at a high deposition rate, and this value increased to 65% when deposited at a moderated rate. Thus theoretically, silver surface segregation can be suppressed by a sufficiently high deposition rate.

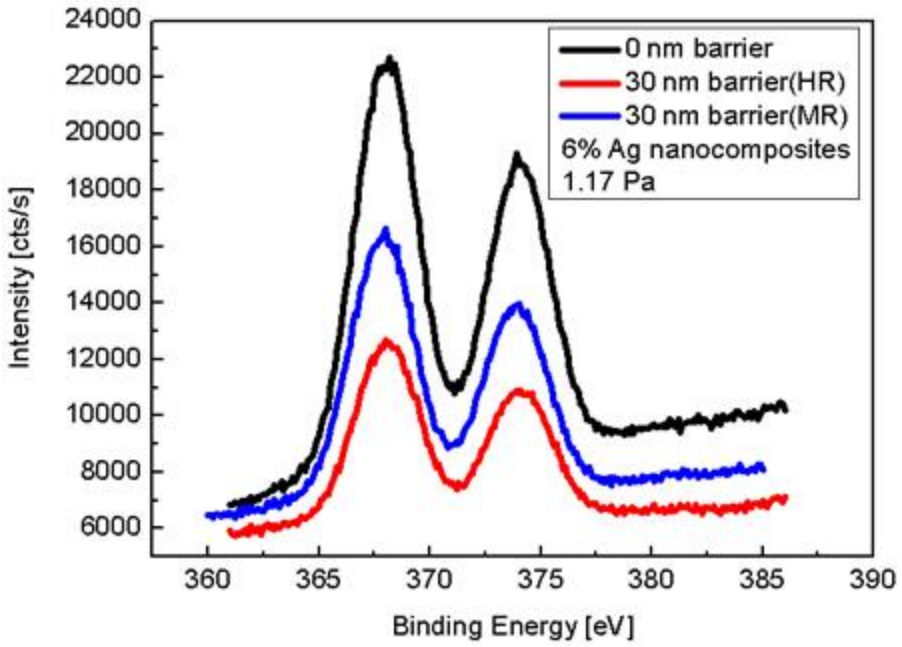

Figure 4.14 X-ray photoelectron spectra of the evolution of Ag 3d core levels depending on the barrier deposition rate during deposition at the surface using 6% Ag filling factor and 1.17 Pa

The optical responses from the nanocomposite coatings were also investigated. As shown in Figure 4.15, the 30% Ag containing nanocomposite without a barrier typically reveals a very broad bandwidth with a maximum absorption peak around 500 nm, which indicates a non-homogenous size distribution of Ag NPs due to the pronounced surface segregation. However, a much narrower and stronger plasmon absorption band is observed for the sample coated with a 50 nm barrier. Due to the absence of surface segregation, the average size of the Ag NPs is decreased resulting in an associated blue shift of the plasmon resonance [9]. The growth of larger Ag NPs in the nanocomposite was successfully suppressed as the surface segregation is eliminated by deposition of a thin barrier under low total pressure. Thus, surface segregation also strongly influences the optical properties of the nanocomposite, and controlling surface segregation represents a precondition for tuning the properties for its various applications.

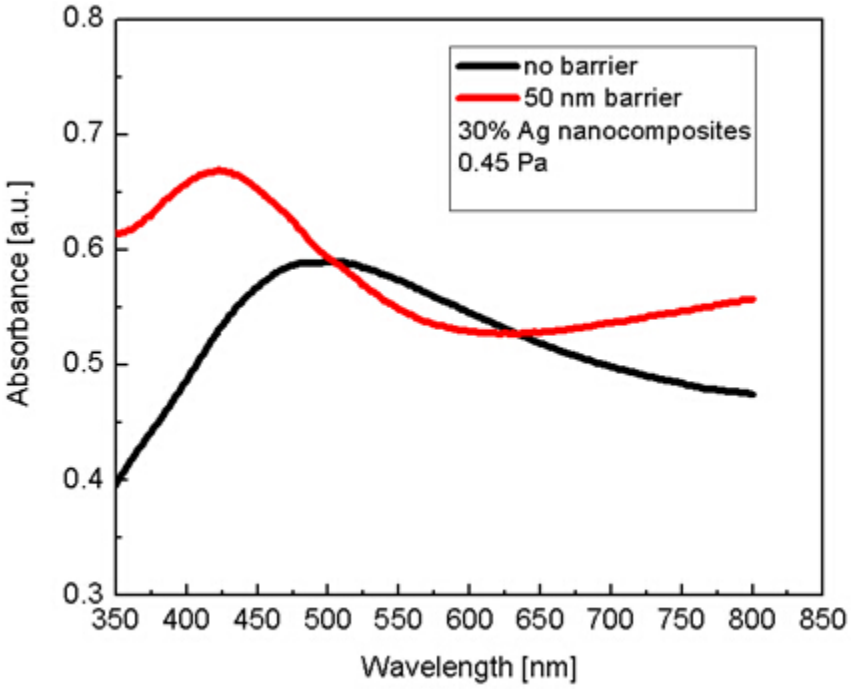

Figure 4.15 UV-Vis spectrum of the optical response from 30% Ag nanocomposite thin films with and without barrier produced at 0.45 Pa

4.2 2D Ag/TiO_x nanocomposites

To better understand the mechanism of Ag NPs diffusion on the surface at high total gas pressure, 2D model systems were prepared at 1.17 Pa. A set of samples with a Ag nanoparticle layer of 2 nm nominal thickness coated onto a 10 nm TiO_x was produced. TiO_x barrier layers with varying thickness were deposited on top with the same moderate rate (6nm/min) as used for TiO_x buffer layer. As shown in Figure 4.16, the SEM images indicate that silver still segregates to the surface even if the silver nanoparticle layer has been covered by a 50 nm TiO_x barrier layer in one step. More discontinuous and larger island structures formed on the surface as the barrier layer thickness increased at a moderate deposition rate.

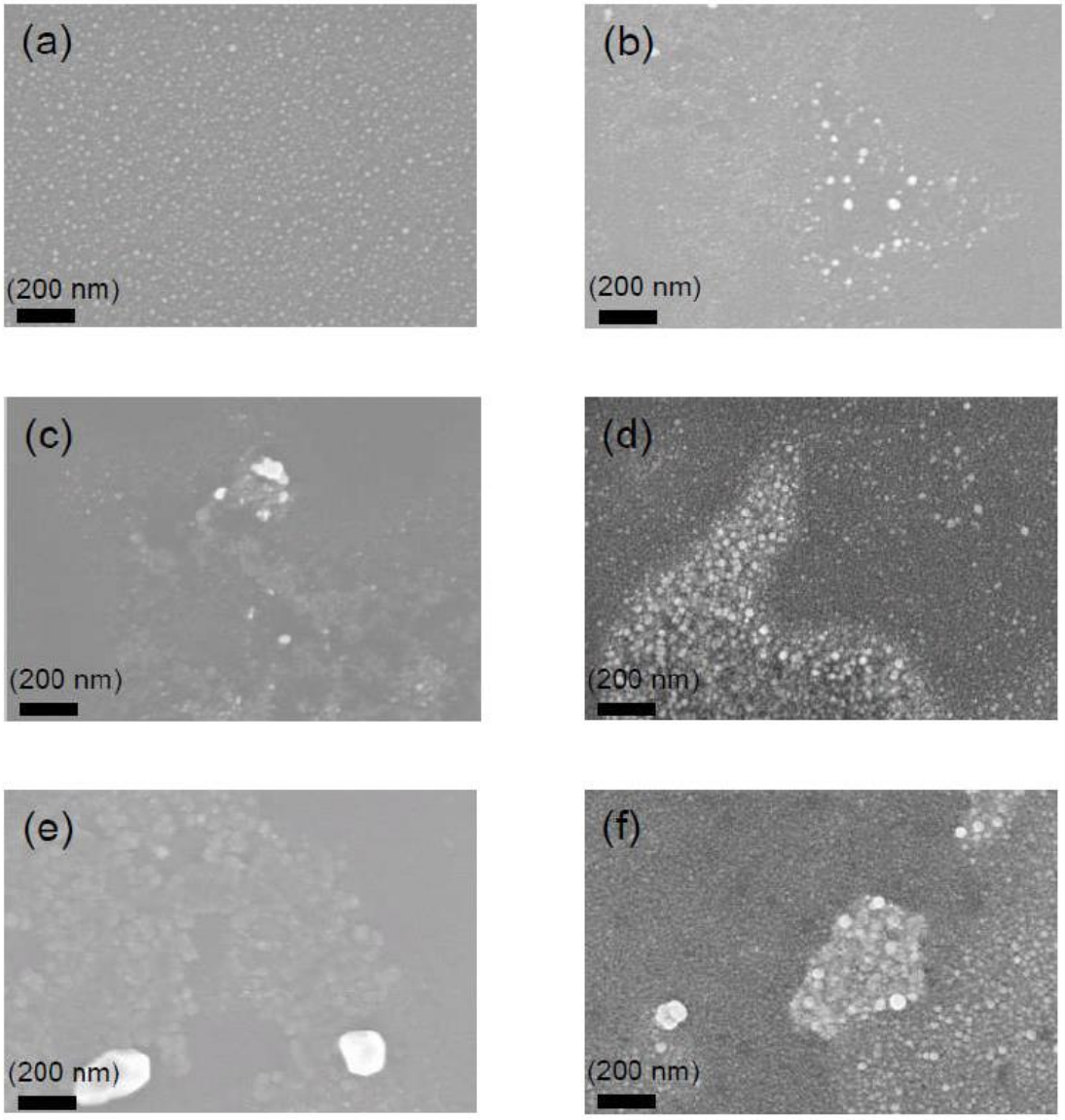

Figure 4.16 SEM images of the surface morphology evolution of 2 nm Ag layer coated with different barrier thicknesses produced at 1.17 Pa with moderate deposition rate. (a) no barrier (b) 10 nm barrier (c) 20 nm barrier (d) 30 nm barrier (e) 40 nm barrier (f) 50 nm barrier

Figure 4.17 shows the X-ray photoelectron spectra of the evolution of Ag 3d core levels depending on the barrier thickness at a moderate deposition rate during deposition at the surface using 2 nm Ag layer and 1.17 Pa. The silver signal detected from the surface only decreased gradually from 66% to 16% as the barrier thickness

was increased from 10 to 50 nm. This clearly demonstrates that a strong surface segregation effect also occurs for already pre-formed silver NPs at high total pressure during barrier deposition. Many researchers [212,213] have reported the Ag diffusion process during a reactive sputtering process. In this process it can be assumed that the reactive plasma together with oxygen destroy the structure of the silver atom layer and results in the silver atom diffusion onto the surface, and the Ag layer structure has possibly been attacked by oxygen ions and thus been modified. Romanyuk et al. [214] also confirmed that the formation of a very thin layer of Ag oxide in the interface between TiO_2 and silver when a pure silver layer was exposed to reactive plasma containing oxygen. The process involves two steps: formation of thin layer of silver oxide and subsequent growth of the TiO_2 thin films.

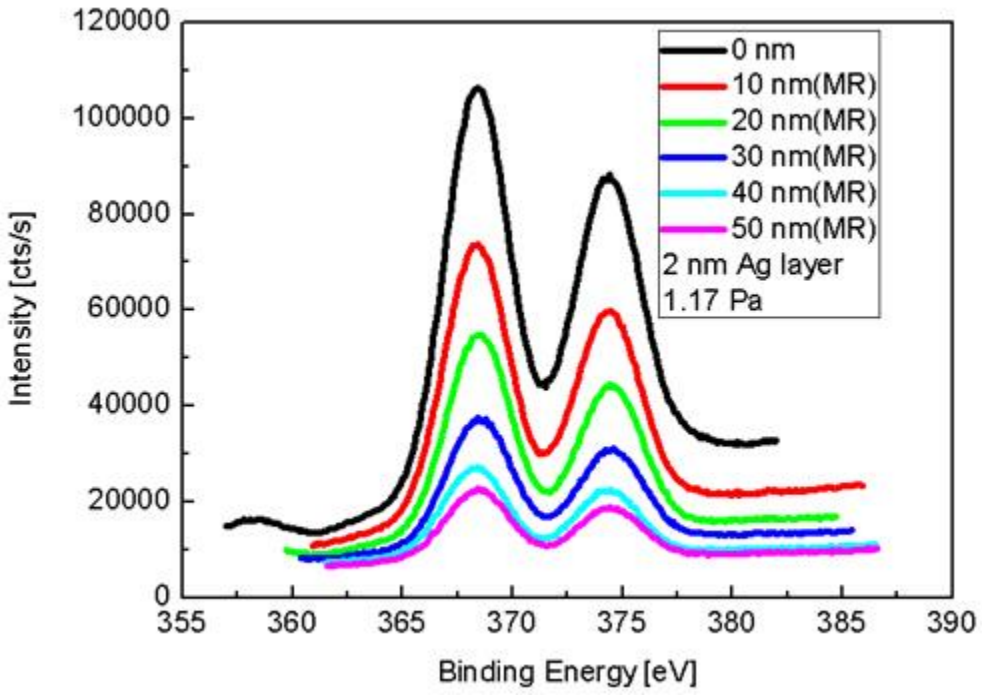

Figure 4.17 X-ray photoelectron spectra of the evolution of Ag 3d core levels depending on the barrier thickness at a moderate deposition rate during deposition at the surface using 2 nm Ag layer and 1.17 Pa.

However, as presented in Figure 4.18, the SEM images clearly show that the silver surface segregation can be further reduced by using a higher deposition rate for the titanium oxide capping layers. No significant silver surface segregation was observed for the samples coated with barriers with high deposition rate. We suppose this could be ascribed to a larger nuclei formation rate at the higher deposition rate, suggesting that a continuous film is produced. The effect of a high deposition rate to suppress the silver signal for the 2D model demonstrates another way to control surface segregation at high total sputtering pressure.

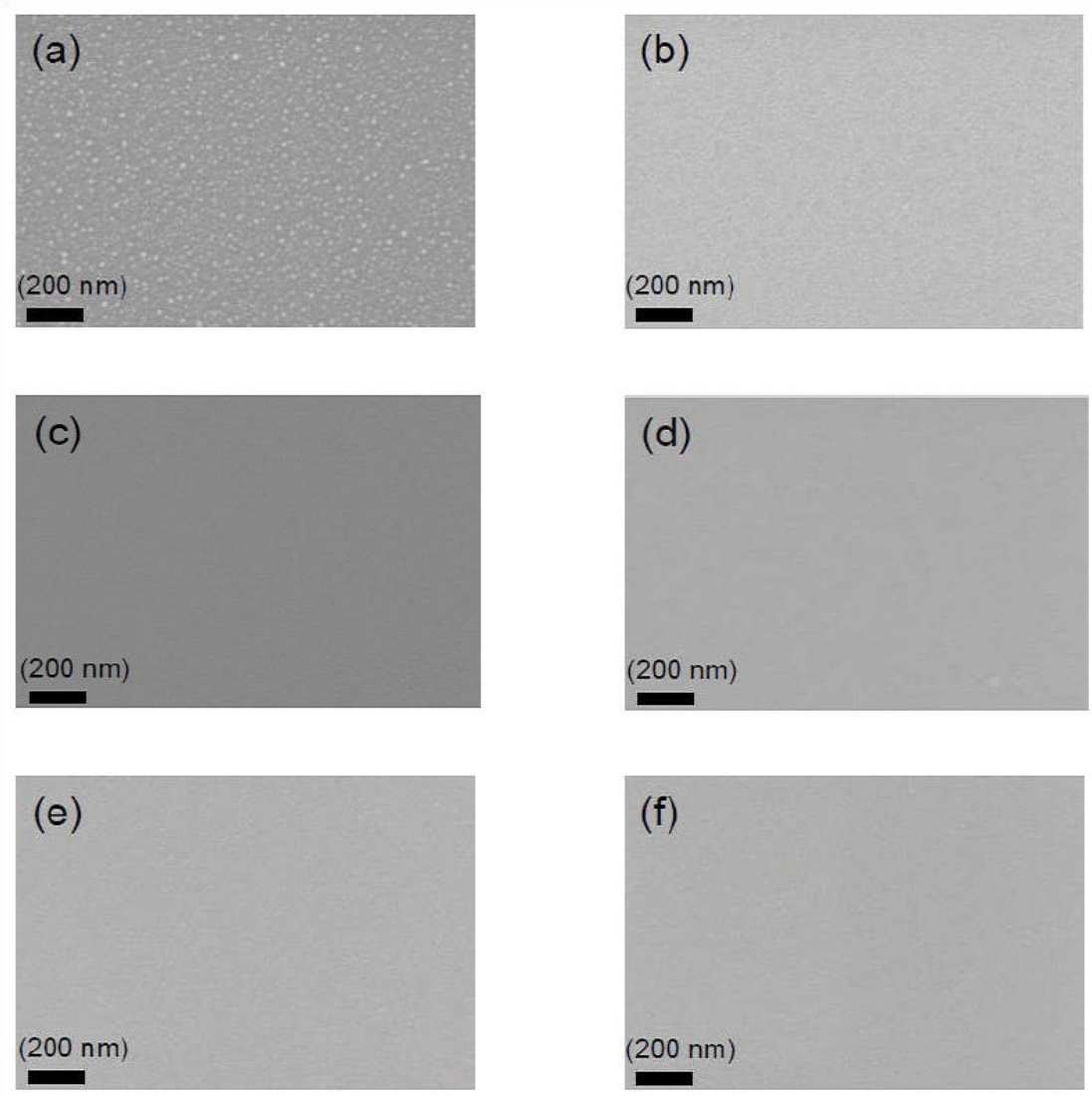

Figure 4.18 SEM images of the surface morphology evolution of 2 nm Ag layer coated with different barrier thickness produced at 1.17 Pa with high deposition rate. (a) no barrier (b) 10 nm barrier (c) 20 nm barrier (d) 30 nm barrier (e) 40 nm barrier (f) 50 nm barrier

The better surface segregation suppression effect by using a higher deposition rate is also confirmed by the X-ray photoelectron spectra in Figure 4.19. One can see that the silver signal intensity on the surface is much weaker than the same samples coated with barriers at a moderate deposition rate, which is showed in Figure 4.16. This indicates that the silver surface segregation can be substantially reduced by increasing the deposition rate for the barrier layers.

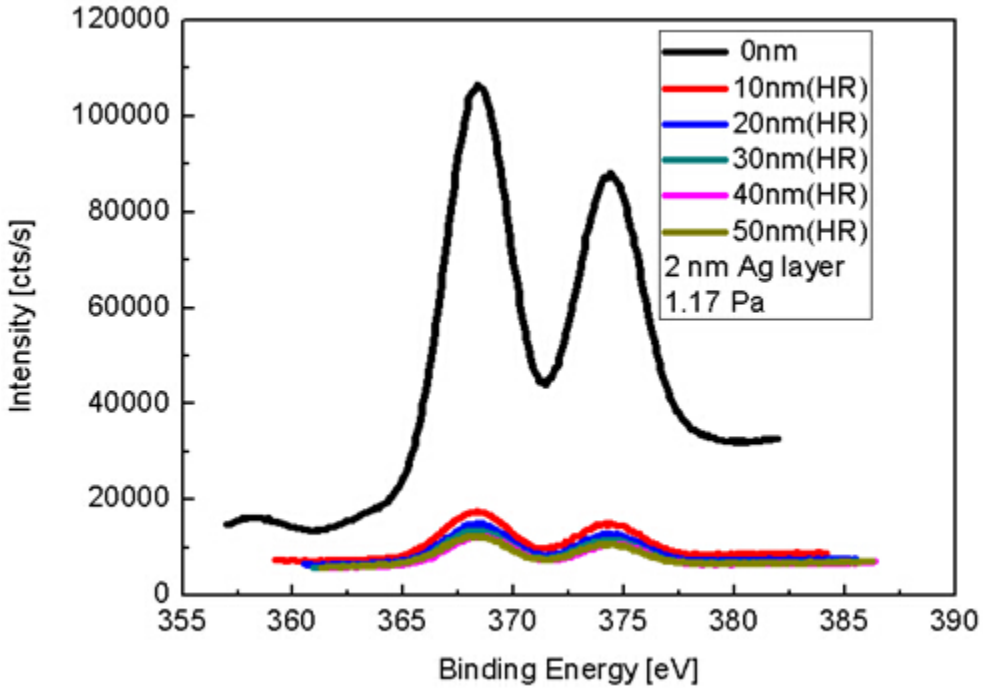

Figure 4.19 X-ray photoelectron spectra of the evolution of Ag 3d core levels depending on the barrier thickness at a high deposition rate during deposition at the surface using 2 nm Ag layer and 1.17 Pa.

Additionally, we deposited a 20 nm barrier on a similar 2 nm Ag nanoparticle layer with a discontinuous plasma process (10 nm gap after deposition of a 10 nm barrier) to compare it to a continuous plasma process where the barrier layers had been deposited in one step. All experiments were performed at a moderate deposition rate. Figure 4.20 shows the X-ray photoelectron spectra of this comparison. It is found that under moderate deposition, the discontinuously deposited barrier layer shows an intensity reduction only from 49% to 41% of Ag at the surface. This result indicates that the Ag surface segregation is a plasma-assisted oxygen-induced process and occurs as soon as the sample is exposed to activated oxygen. Another way to change the microstructure and morphology of the deposited thin film is to increase the deposition rate. As can be seen in Figure 4.20, the silver intensity on the surface is substantially decreased by increasing the deposition rate (HR, around 15 nm/min) of

the barrier. The silver signal on the surface is reduced to 9% under high rate conditions, and no change is observed for a high rate discontinuous process.

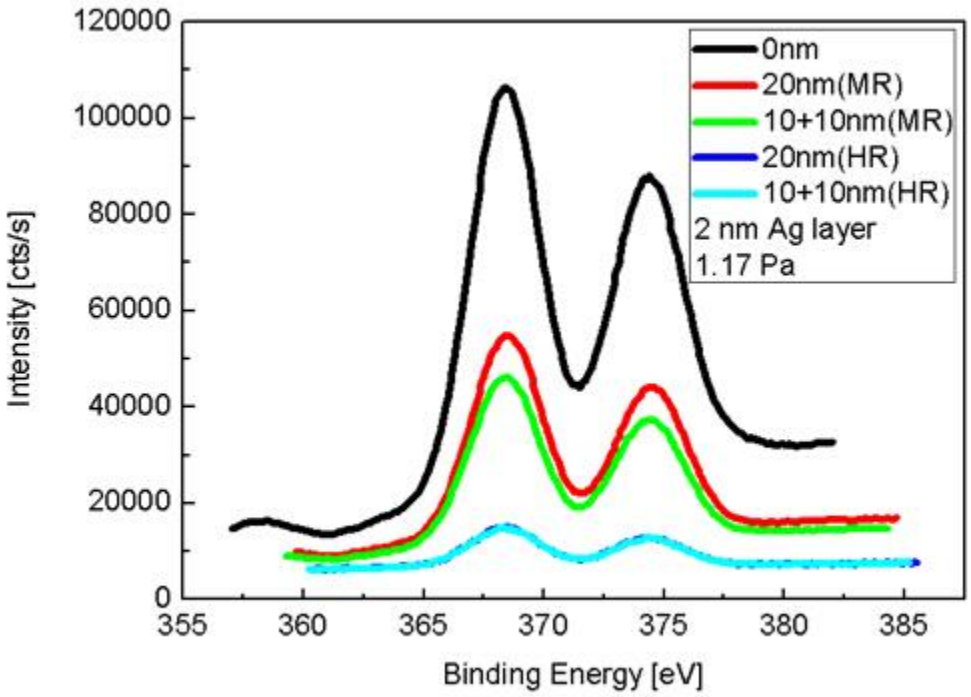

Figure 4.20 X-ray photoelectron spectra of the evolution of Ag 3d core levels depending on the plasma continuous and barrier deposition rate during deposition at the surface using 2 nm Ag layer and 1.17 Pa.

In a comparative study, 10, 30 and 50 nm pure metallic titanium non-porous barrier layers were deposited on a similar 2 nm Ag nanoparticle layer without oxygen admixture. As shown in Figure 4.21, the X-ray photoelectron spectra indicates that a 30 nm barrier layer is the critical size to cover all the silver NPs, and silver atoms diffusion onto the surface was stopped under pure Ar atmosphere, which further supports that Ag surface segregation is a plasma assisted oxygen induced process and occurs as soon as the silver atoms are exposed to activated oxygen.

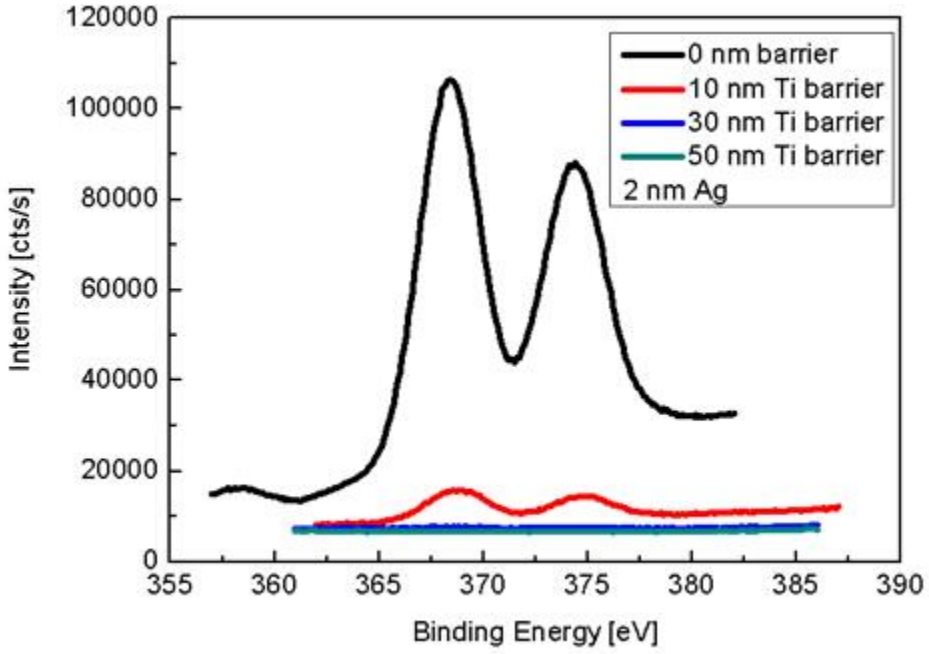

Figure 4.21 X-ray photoelectron spectra of the evolution of Ag 3d core levels depending on the titanium barrier thickness during deposition at the surface using 2 nm Ag layer and pure Ar atmosphere (120 sccm).

4.3 Conclusions

A systematic investigation of the silver surface segregation phenomenon in a reactive sputtering process for the preparation of 2D/3D silver/titanium oxide nanocomposites has been presented. 3D silver/titanium oxide nanocomposite coatings have the great advantage of offering long-lasting stable silver ion release with defined silver NPs size, shape and distribution, while more simple 2D layer structures with deposition of the Ag NPs on the surface of TiO_x buffer layer instead of 3D model made them directly accessible and easily investigatable regarding the geometrical arrangements of the Ag NPs and their morphology variations. It was found that the titanium oxide matrix is in an amorphous form and the silver NPs exhibit the fcc lattice structure of metallic silver for both chosen oxygen flow rates and total gas pressures. No silver oxide peaks were observed in either case.

It is clearly evident that silver surface segregation can hardly be avoided even with the use of barriers when a high total pressure is used in the sputtering process for both 2D and 3D nanocomposites. At high pressure the silver segregation can be only slightly reduced by the use of barrier layers. Under these conditions the silver segregation is influenced by the rate used for the deposition of the barrier layers and is much reduced for higher deposition rates. This is ascribed to the larger nuclei formation rate at this higher deposition rate and leads to a continuous barrier film to suppress the silver segregation.

Results showed that an effective decrease of silver surface segregation is only achieved when the total pressure during sputtering is reduced to 0.45 Pa or even 0.15 Pa. Here, the silver surface segregation can be already completely suppressed using a capping layer of 30 nm thickness. This is believed to be caused by a much more densely packed TiO_x layer formed at lower total sputtering pressure, whereas at higher total pressures, always porous TiO_x layers are formed. This was confirmed by the TEM investigations that a textured silver NP arrangement formed in the 3D nanocomposites due to the porous TiO_x matrix, while a more homogenous Ag NP distribution was observed after reducing the total pressure. Moreover, elimination of the surface segregation by coating with a 50 nm barrier results in a much more

homogenous size distribution of the silver nanoparticles in the nanocomposite giving rise to a much narrower plasmon absorption band with a blue shifted absorption peak maximum. These results indicated that the deposition conditions used for the preparation of reactively sputtered silver/titanium oxide nanocomposite thin films have a strong influence on the surface segregation behavior of the silver and thus on the morphology of the films produced. This is expected to have an important effect on the properties of the films prepared, e.g. their optical properties, silver release and ageing behavior.

Chapter 5

Silver ion release in reactively sputtered Ag/TiO_x nanocomposites

In this chapter the silver ion release through 2D/3D silver/titania nanocomposite coatings with varied filling factors and barrier thicknesses by using different deposition parameters were investigated. Samples were then immersed in water for several time periods (40 min, 2 h, 1 d, 3 d and 7d) and the concentration of the silver ion released from the 2D/3D systems into the water was measured using the AAS technique. The study of the silver ion release property was performed by using SEM, TEM and XPS, and accompanied with a control of the nanocomposite morphology (Ag NPs concentration and distribution) to understand the mechanism.

5.1 Silver ion release property in 3D Ag/TiO_x nanocomposite thin films

Since silver based nanocomposites have received great research interest for their promising applications in the medical field, the use of these nanocomposites should be taken with caution. T. Hrkac et al. [210] stated that for silver containing composites the antibacterial effect is often accompanied by cytotoxicity to mammalian cells. The therapeutic window of high antimicrobial activity without concomitant cytotoxicity should be taken into account carefully. Thus, a controllable silver ion release rate from nanocomposites becomes the key issue for the usage of silver containing composites.

Because the oxidation of silver would cause the diffusion of silver atoms with oxygen ions to the surface due to the relatively lower surface energy of Ag oxide compared to the titanium oxide matrix, and because of the possible cytotoxicity of silver oxide to the mammalian cells, largely silver oxide forms should be avoided in the reactive sputtering process. Figure 5.1 shows the grazing incident X-ray diffraction patterns of 15% Ag-containing nanocomposites prepared at different total pressures. The titanium oxide matrix is always in an amorphous form and the silver NPs exhibit the face-centered cubic (fcc) lattice structure of metallic silver for both chosen total gas pressures. The different background intensities in the XRD measurements correspond to differences in surface roughness and density of the coatings prepared under different pressure conditions. The sample prepared at 1.17 Pa has a more precipitous variation due to its more rough and porous surface microstructure. In addition, since the intensity of the characteristic silver X-ray reflexes is rather low, some silver oxide formation is possible and the intensity of the typical silver oxide X-ray reflexes might be too low to be detected.

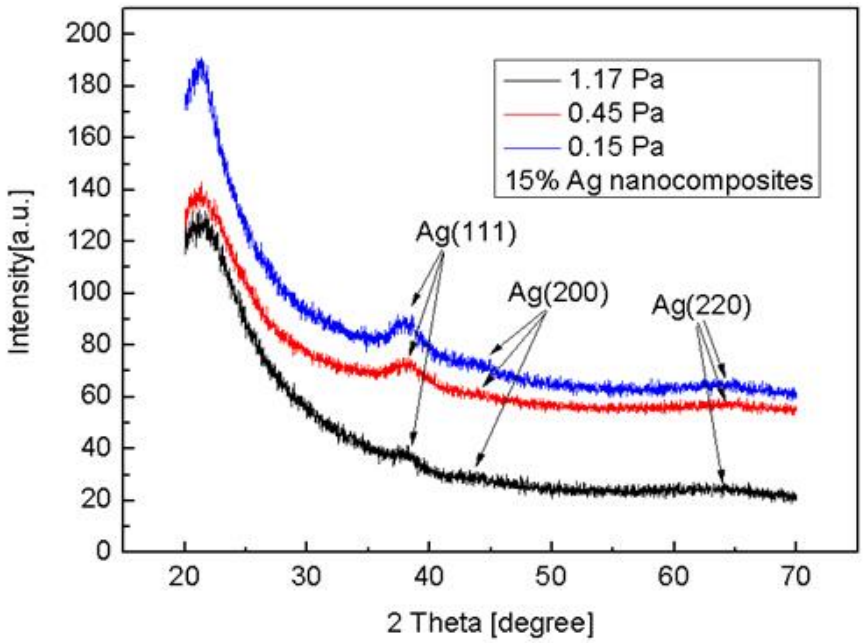

Figure 5.1 Grazing incident X-ray diffraction patterns of 15% Ag containing nanocomposite thin films prepared at different total pressure (0.15, 0.45, 1.17 Pa)

Figure 5.2 shows the cumulative concentration of silver ions released after an elapsed amount of time (40 min, 2 h, 1 d, 3 d and 7 d). One can see that the amount of silver ion release increased as the silver concentration increased. Furthermore, as shown in Fig 5.3, different barrier thicknesses were coated onto the different silver nanocomposites at 1.17 Pa. But it was observed that the silver ion release rate did not show a large decrease with a barrier coated on top, even with a barrier thickness of 60 nm. As we mentioned before, this can be ascribed to the large silver surface segregation phenomenon happening at high total pressure. The silver surface segregation could not be suppressed by coating the barrier here due to the porous structure of titanium oxide films.

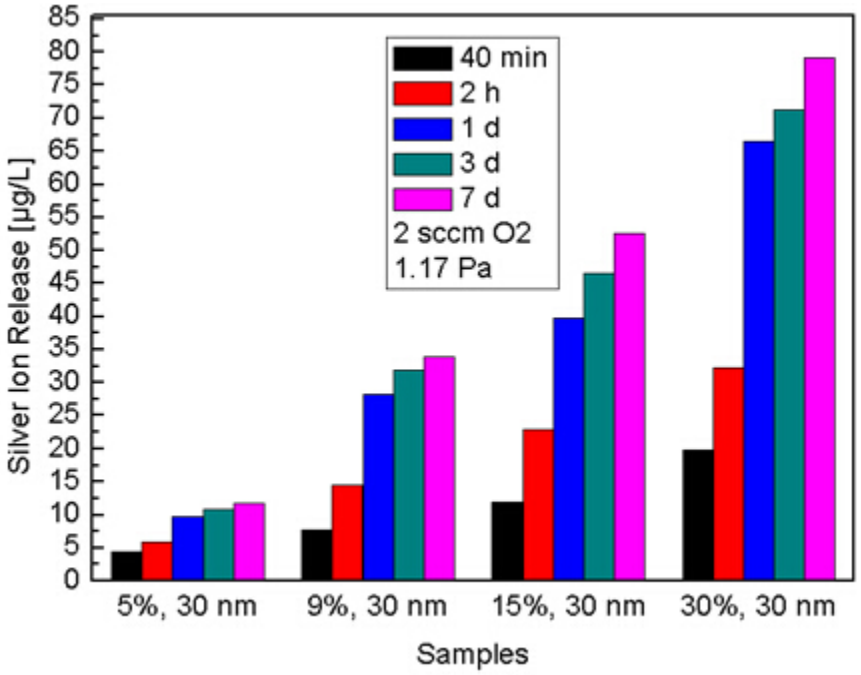

Figure 5.2 Relationship of the cumulative concentration of silver ion release to elapsed time. 30 nm barrier coated Ag nanocomposites were produced with different Ag filling factors at 1.17 Pa

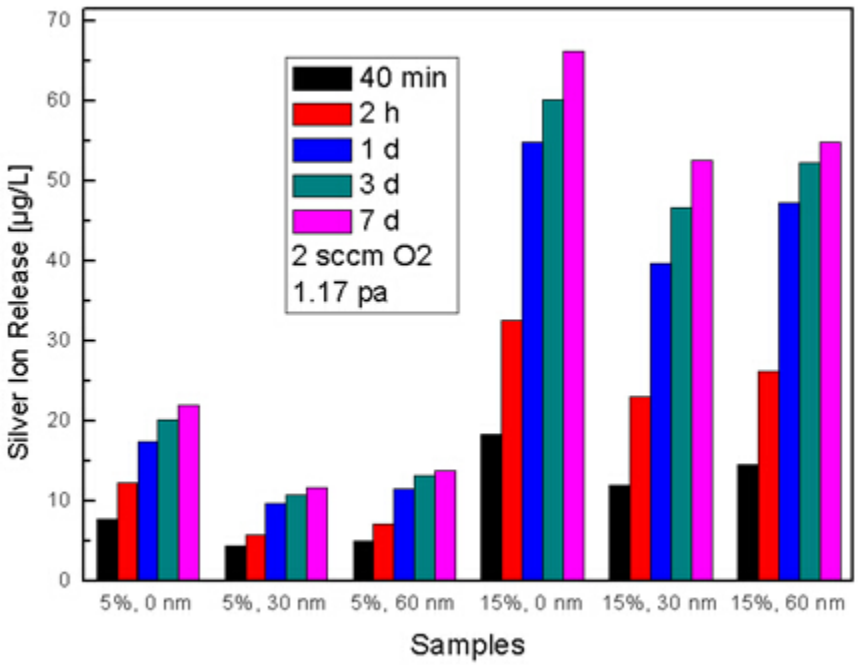

Figure 5.3 Relationship of the cumulative concentration of silver ion release to elapsed time. 5% and 15% Ag nanocomposites were produced with different barrier thicknesses at 1.17 Pa

Moreover, the influence of the oxygen amount on the silver ion release was also investigated here. As depicted in Figure 5.4(a), the cumulative concentration of silver ions released was compared between two coatings which were prepared at different oxygen flow rates. One can see that the total silver ion amount released does not show a big difference after 7 days of exposure to water; however, we can find in Figure 5.4(b) that the coating prepared with a higher oxygen flow rate has a higher release potential at the initial stage but a lower increase after 1 day in water compared with the coating prepared with lower oxygen flow rate. This may be caused by a more severe surface segregation happening when more oxygen was used and more silver atoms accumulated on the surface and are released at the initial stage.

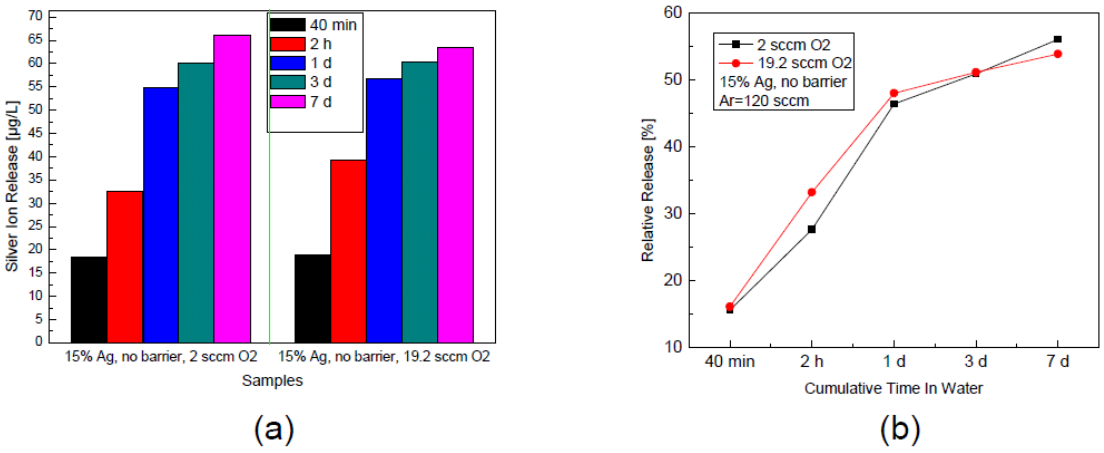

Figure 5.4 (a) The cumulative concentration of silver ion release (b) and % relative silver release to elapsed time. 15% Ag nanocomposites were produced with different oxygen flow rates

Figure 5.5 presents the silver ion release behavior of nanocomposite coatings prepared at different total pressures (1.17 Pa, 0.45 Pa and 0.15 Pa). One can find the sharp decrease of silver ion release after the total gas pressure was reduced from 1.17 Pa to 0.15 Pa as shown in Figure 5.5(a). The amount of silver ion release decreased to a very low level when the total gas pressure was lowered to 0.15 Pa. Figure 5.5(b) shows the relative silver release after 7 days for the coatings prepared at different total pressures. The thin film prepared at 1.17 Pa has a very large release rate at the initial stage; nearly 50% silver is released into the water in the first day. After that, the silver ions are released at a very slow rate and only around 5% silver ions are released into the water from the 1st day to the 7th day. However, for the coatings prepared at lower total pressures (0.45 Pa and 0.15 Pa), a slower but more stable release was observed during the whole immersion period and only around 20 % silver is released into the water after 7 days for the sample produced at 0.15 Pa, indicating that the samples deposited at lower total pressures could offer a promising long-lasting stable silver ion release property.

This can be explained from two aspects. Firstly, a higher total gas pressure results in a more open and porous structure which allows the silver NPs to release to the surface and release more silver ions at the initial stage. Secondly, the total gas pressure has a strong effect on the hydrophilic property of titanium oxide; the hydrophilic property can be improved by increasing the total pressure. The main factors influencing the hydrophilic property of titanium oxide are the crystal structure and surface roughness. Since here the titanium oxide exhibits an amorphous structure, the rougher surface at high total pressure plays a key role in increasing the hydrophilic property due to a greater surface area and more voids inside the layer [215,216] .

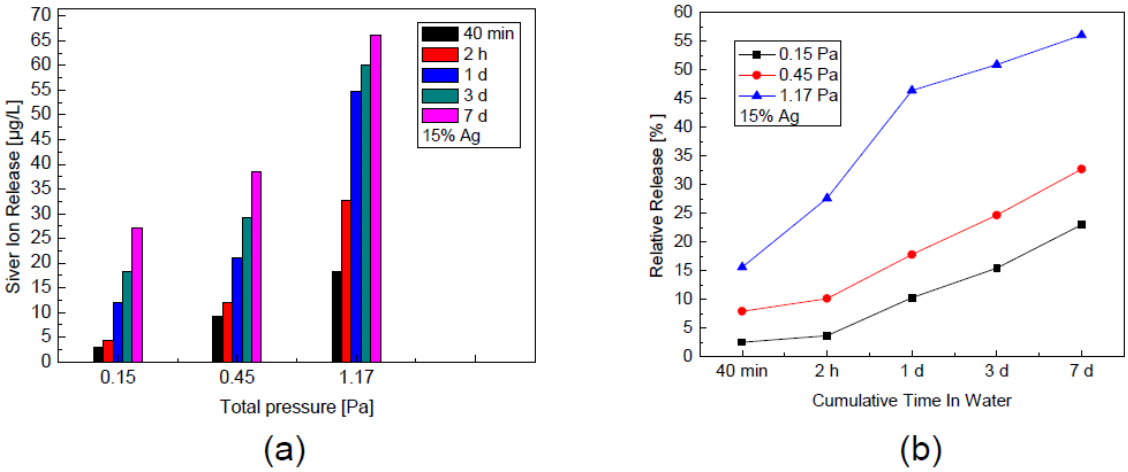

Figure 5.5 (a) The cumulative concentration of silver ion release and (b) % relative silver release to elapsed time. 15% Ag containing nanocomposites were produced at different total pressures of 0.15, 0.45 and 1.17 Pa

Figure 5.6 shows the TEM images of the coatings with 15% Ag inside deposited at different total pressures of 0.15, 0.45 and 1.17 Pa, respectively. Ag NPs contacted each other and agglomeration happened everywhere in the sample prepared at 1.17 Pa due to the porous structure of TiO_x matrix as shown in Fig. 5.6 (a). Thus more silver ions are released at the beginning after exposure to water. However, no silver agglomeration was observed when the total pressure was reduced to 0.45 or even 0.15 Pa as presented in Fig. 5.6 (b) and (c), respectively. The silver NPs are well distributed in the matrix, and a smaller size and more regular round particle shape can

be found when the total pressure is further decreased to 0.15 Pa. This can be ascribed to the more dense and rigid TiO_x matrix that is deposited at lower total pressure largely reducing the silver mobility promoted by the admixed oxygen.

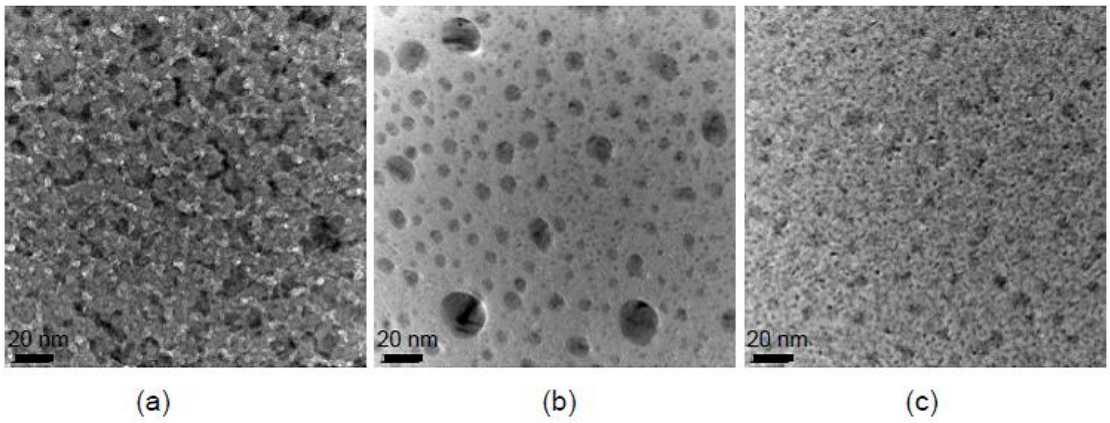

Figure 5.6 BF-TEM images of Ag NPs size distribution in the matrix with of 15% Ag without barrier produced at different total pressures. (a) 1.17 Pa; (b) 0.45 Pa; (c) 015 Pa

The surface morphology changes to the 15% Ag containing nanocomposite prepared at 0.45 Pa after 7 days exposure to water is shown in Figure 5.7 (a) and (b). One can see that the density of Ag NPs on the surface only shows a slight decrease and most of Ag NPs remain stable in size after 7 days immersion in water, while Ag NPs with a smaller size were found on the surface. Considering the slow but long-lasting silver ion release from the coating, more silver ions are expected to be released from the bulk.

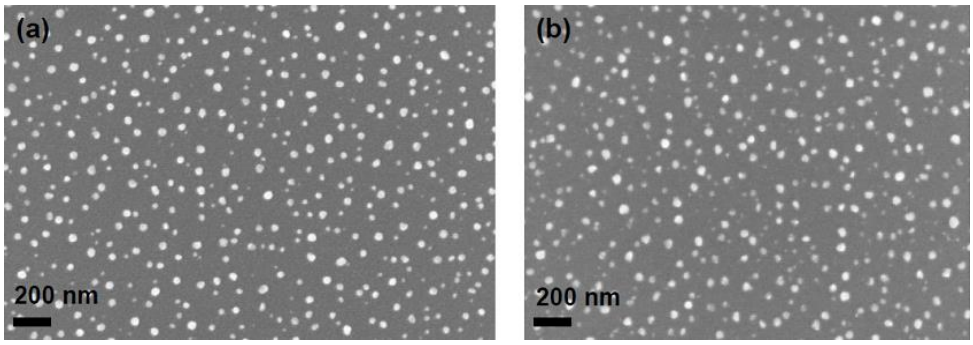

Figure 5.7 SEM images of the surface morphology evolution of 15% Ag nanocomposites without a barrier deposited at 0.45 Pa before immersion in water (a) and after 7 days in water (b)

TEM measurements were also done after 7 days of immersion of the sample deposited on the TEM grid in water. Figures 5.8 (a) and (b) show changes in the morphology of 15% Ag containing nanocomposite before and after immersion in water. The density of silver NPs in the matrix becomes smaller after 7 days in water and most of the Ag NPs with smaller size disappear due to silver ion release, which is more favorable from smaller Ag NPs [94]. Note that some silver NPs on the surface may undergo the Ostwald ripening process because larger NPs may form by resorption of silver atoms.

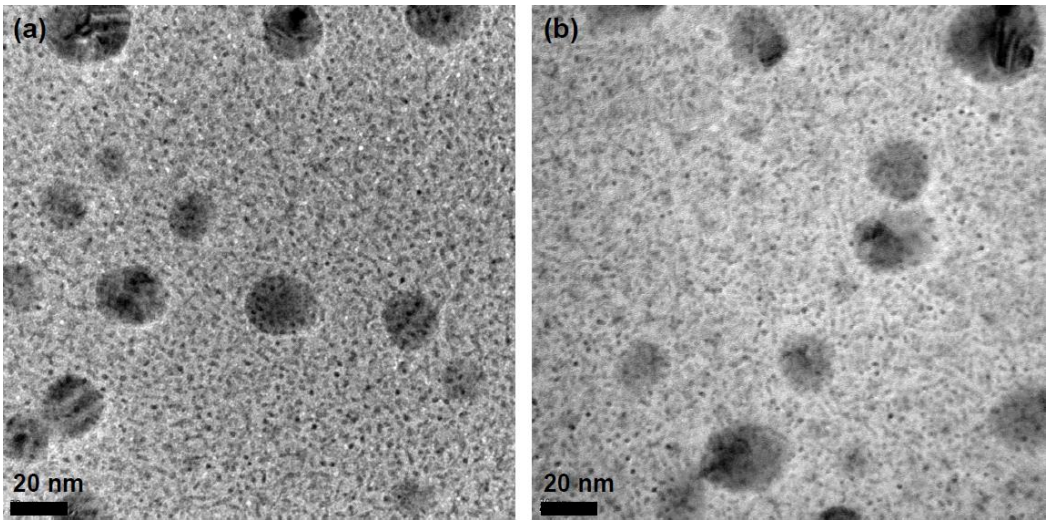

Figure 5.8 BF-TEM images of the surface morphology evolution of 15% Ag nanocomposites without a barrier deposited at 0.45 Pa before immersion in water (a) and after 7 days in water (b)

Fig. 5.9 (a)-(b) show the HAADF-STEM images of the coating with 15% silver containing nanocomposite produced at 0.45 Pa before and after immersion in water. Note that some bigger silver NPs on the surface with growing size and distance between each other may undergo the Ostwald ripening process after immersion in water as presented in Fig. 5.9 (b). The larger Ag NPs on the surface are formed by resorption of new silver atoms depleted from the smaller Ag NPs in the bulk. The kinetics of Ostwald ripening depend on two separate factors: the free energy instability of the particles and the relative concentration of larger size particles [217]. The rate of particle reformation can be significantly sped up by increasing the relative

amount of larger spherical particles, i.e. the case in the bulk. After immersion in water, some silver ions that desorbed from the smaller NPs in the bulk have a high probability to resorb onto the larger and more-stable spherical particles nearby, inducing Ostwald ripening on the surface. The production of new, smaller silver NPs by the transfer of ions from larger silver NPs may be thought to increase the free energy of the system due to increased surface energy of smaller ones. However, the specific interaction between the silver NPs and surface, the low temperature combined with lasting ion release from the bulk, and the absence of relative larger silver NPs may contribute to the stability of these new particles.

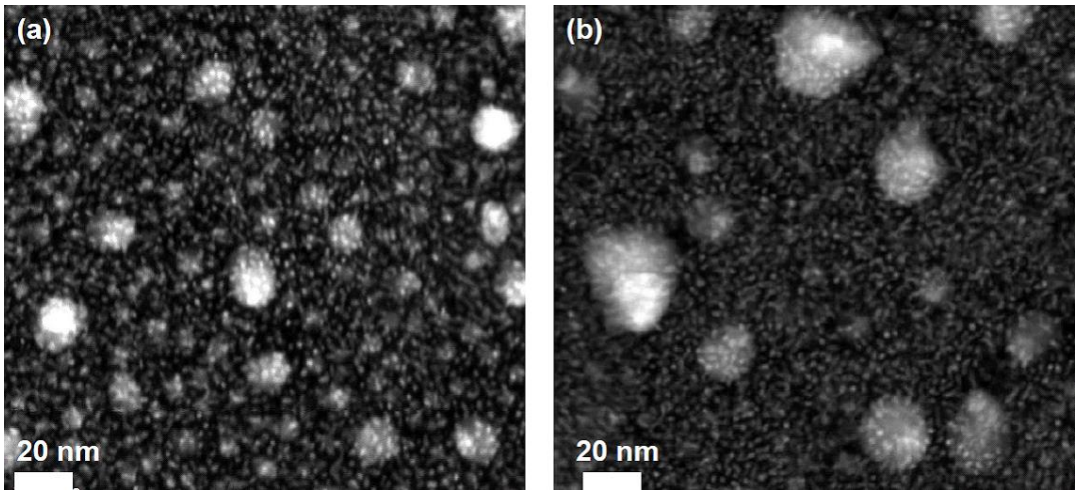

Figure 5.9 HAADF-STEM images of the surface morphology evolution of 15% Ag nanocomposites without a barrier deposited at 0.45 Pa before immersion in water (a) and after 7 days in water (b)

Figure 5.10 presents the silver ion release behavior of nanocomposite coatings with a 30 nm barrier prepared at different total pressure (1.17 Pa, 0.45 Pa and 0.15 Pa). One can see that the amount of silver ion release for the coatings prepared at 0.15 Pa and 0.45 Pa were all reduced to a very low level in Figure 5.10 (a). Less than 5 μg/L silver ions were released after 7 days exposure to water. However, the amount of silver ions released for the thin film prepared at 1.17 Pa still shows a high release potential. Figure 5.10 (b) presents the relative silver release (%) during 7 days of the

coatings with 30 nm barriers prepared at different total pressure. It is surprising to find that after 7 days only around 10 % of the silver had been released into the water for the coatings prepared at 0.15 Pa and 0.45 Pa, while more than 40 % of the silver was released into the water for the sample prepared at 1.17 Pa during this period.

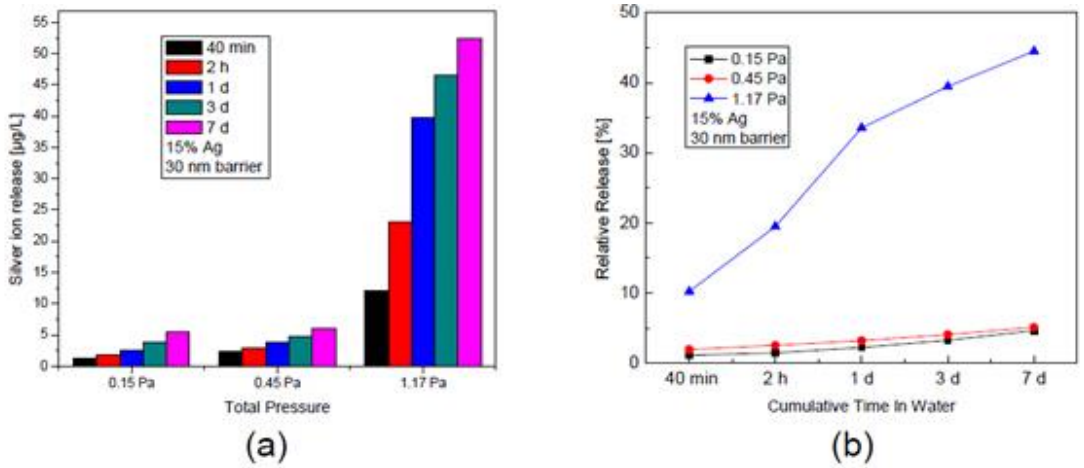

Figure 5.10 (a) The cumulative concentration of silver ion release and (b) % relative silver release to elapsed time. 15% Ag containing-nanocomposites with 30 nm barrier were produced with different total pressures of 0.15, 0.45 and 1.17 Pa

Figure 5.11 shows the SEM images of barrier layer effect to the controlling surface segregation of the nanocomposite coatings. It can be surprisingly found that the capping layer has no effect on suppressing the silver surface segregation under 1.17 Pa, and still a large amount of silver NPs existed on the surface. It can be assumed that the oxygen induced by the reactive plasma resulted in the diffusion of Ag atoms when the titanium oxide barrier has a porous and loose structure. This is also the reason for the substantially higher silver ion release for the coating prepared at higher total pressure. However, no silver NPs diffused onto the surface after adding barrier layers when the total pressure was decreased to 0.45 and 0.15 Pa. This can be ascribed to the rigid and compact microstructure of the titanium oxide barrier at these conditions.

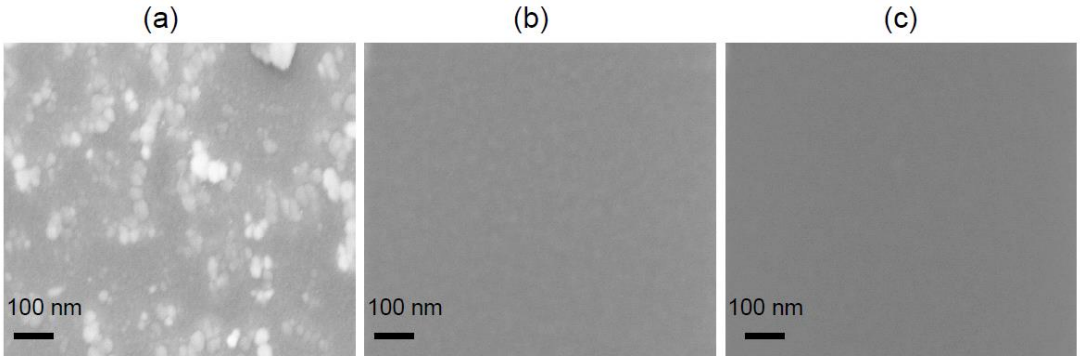

Figure 5.11 SEM images of the surface morphology evolution of nanocomposites with 30 nm barrier produced with decreasing total pressures of 1.17 Pa (a), 0.45 Pa (b) and 0.15 Pa (c)

The coatings with different silver concentration prepared at lower total pressure (0.45 Pa) show a similar release behavior compared with the samples produced at higher total pressure (1.17 Pa) as depicted in Figure 5.12, the silver ion release increased as the silver concentration was increased. The influence of barrier thickness was investigated for the samples prepared at lower total pressure (0.45 Pa), as shown in Figure 5.13; the silver ion release from the 15% Ag containing nanocomposites can be sharply suppressed after coating a 10 nm barrier. But the silver ion release cannot be further reduced when the barrier thickness is increased, even after a 50 nm barrier thickness has been coated.

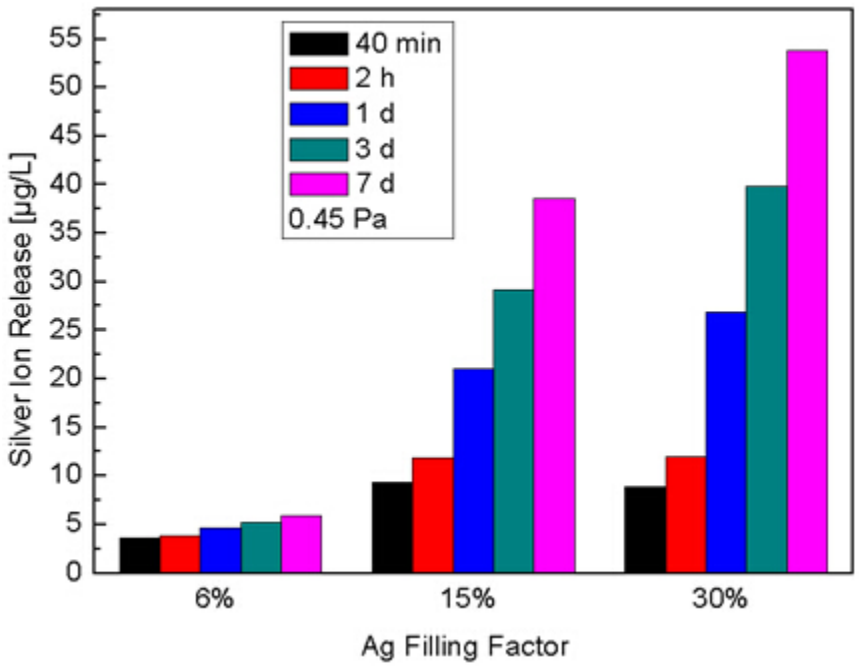

Figure 5.12 The cumulative concentration of silver ions release to elapsed time. Ag containing-nanocomposites were produced with different Ag filling factor at 0.45 Pa

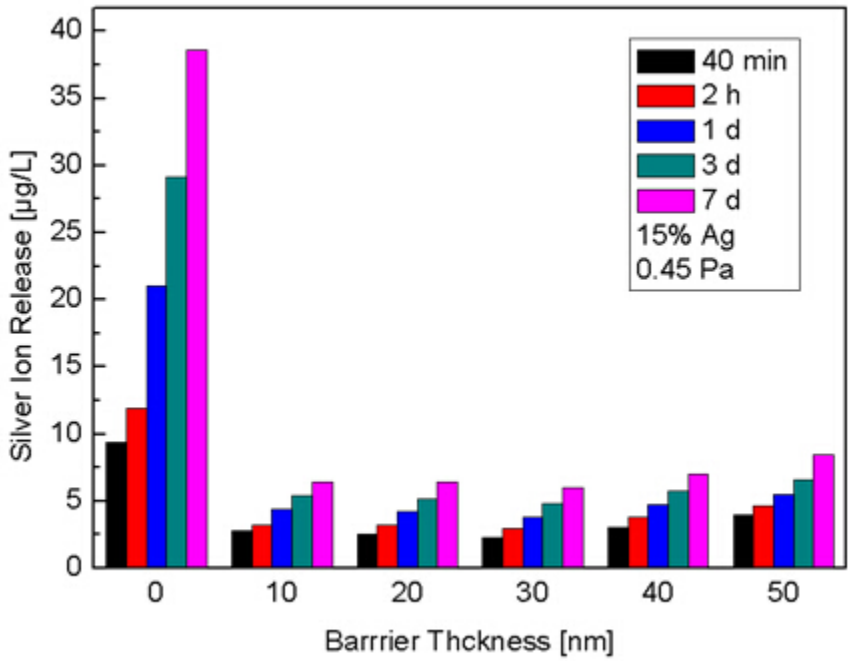

Figure 5.13 The cumulative concentration of silver ions release to elapsed time. 15% Ag containing-nanocomposites were produced with different barrier thickness at 0.45 Pa

The lower silver ion release ability after coating barriers can be explained by the evolution of the surface morphology. Figure 5.14 presents the XPS results of 30% silver containing nanocomposites with different barrier thickness prepared at 0.45 Pa. One can easily find that a very strong silver signal on the surface is observed when no capping layer was coated onto the 30% Ag containing coatings at 0.45 Pa. The silver signal is dramatically reduced when a titanium oxide barrier is coated on top. There, no silver signal is detected when a 20 nm or thicker barrier layer has been deposited, which indicates a perfect suppressing effect for the Ag surface segregation at lower total pressure.

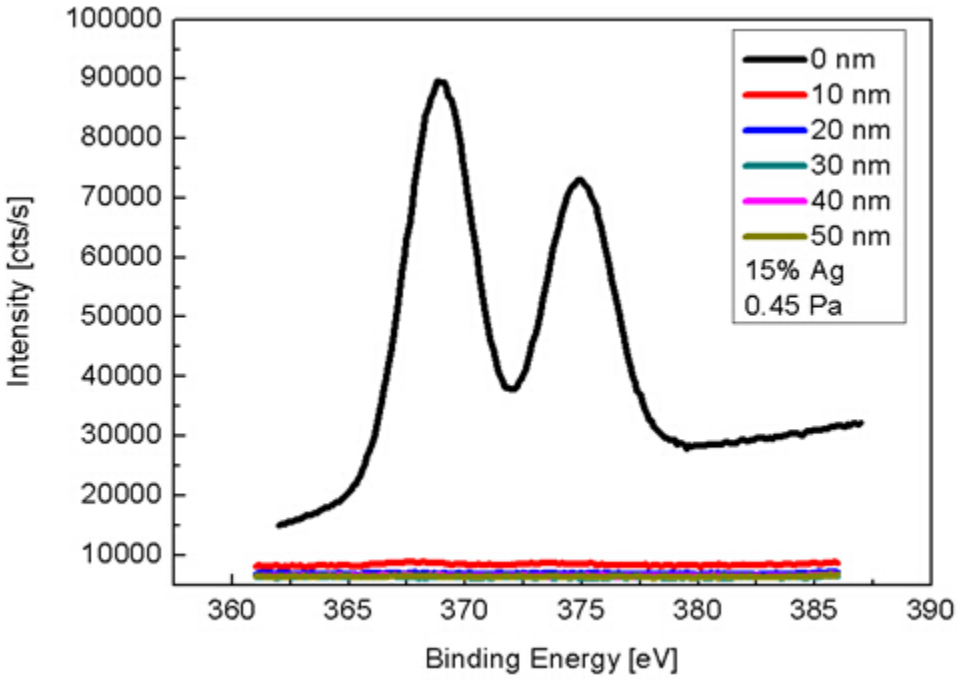

Figure 5.14 X-ray photoelectron spectra of the evolution of Ag 3d core levels depending on the barrier thickness during deposition at the surface using 15 % Ag filling factor and 0.45 Pa

Silver ion release from the composites is a very complex process, not only related to the silver NP size, shape and distribution, but also related to the water uptake, matrix properties, and even to the substrate. The silver ion release from the nanocomposites can be divided into three steps: (1) the water molecules diffuse into the bulk; (2) the surface of silver NPs become oxidized in the presence of oxygen and water, generating silver ions and desorb from the surface; (3) silver ions release from the bulk. Since the oxidation of silver NPs is quite a fast process in the water, the transfer of water molecules in the bulk is the key point influencing the release rate.

Figure 5.15 shows the SEM images of the surface morphology evolution for the 15% Ag nanocomposites with a 50 nm barrier deposited at 0.45 Pa before and after 7 days of exposure to water. One can find that a 'channel' several micrometers in size was presented after 7 days of exposure to water. This hole formed by an impurity can

be the reason why the silver ion release is not gradually reduced after increasing barrier thickness.

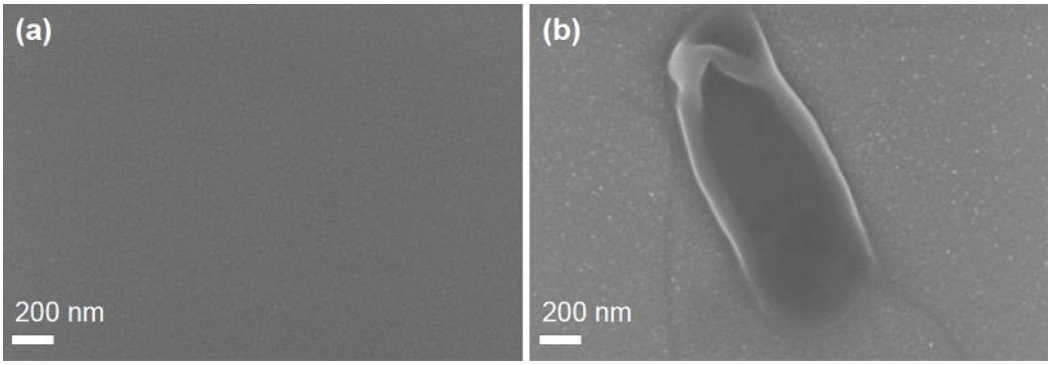

Figure 5.15 SEM images of the surface morphology evolution of 15% Ag nanocomposites with 50 nm deposited at 0.45 Pa before and after 7 d of exposure to water. (a) before water; (b) after 7 d in water

The forming of this channel on the surface should be related to the nature of the titanium oxide amorphous structure. Fig. 5.16 shows the HAADF-STEM image of the morphology of 15% Ag nanocomposites with a 20 nm barrier deposited at 0.45 Pa. One can find that lots of 'nano-pores' are formed in the nanocomposite, and this would facilitate the water diffusion into the bulk at a fast rate. The difference of barrier thickness could be negligible when such a nanocomposite film is exposed to water, resulting in a similar release rate for the samples coated with barriers of different thickness. The silver ion release rate is then only related to the silver concentration in the nanocomposites and not to the barrier thickness.

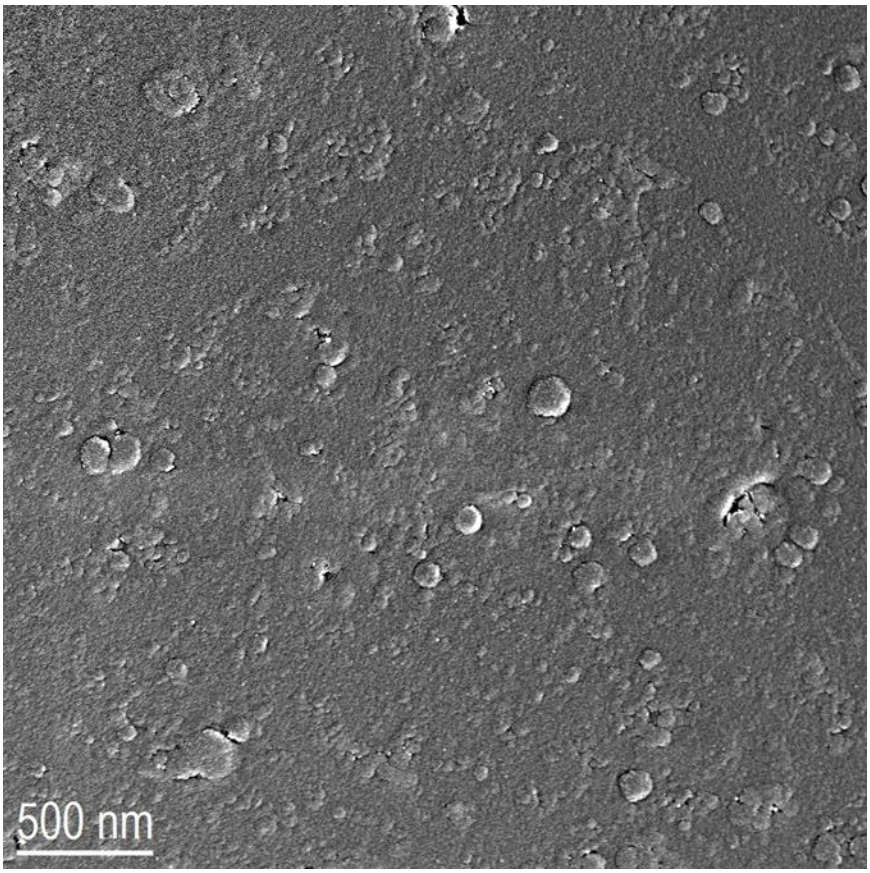

Figure 5.16 HAADF-STEM image of the morphology of 15% Ag nanocomposites with 20 nm barrier deposited at 0.45 Pa

In addition, the influence of the barrier deposition rate to the silver ion release property was also investigated here. As depicted in Figure 5.17 (a), 6% silver containing nanocomposites with a 30 nm barrier deposited at different rates were prepared, and the coating with a high barrier deposition rate shows a lower silver ion release after 7 days in water compared with the film with lower barrier deposition rate. The relative silver release (%) was plotted in Figure 5.17 (b). One can find that the sample with a higher barrier deposition rate shows a stable release during a period of 7 days, while the sample with a lower barrier deposition rate has a very low release potential after 1 day in water. This is due to the larger nuclei formation rate at higher deposition rates, leading to a continuous film favorable for suppressing the surface segregation effect.

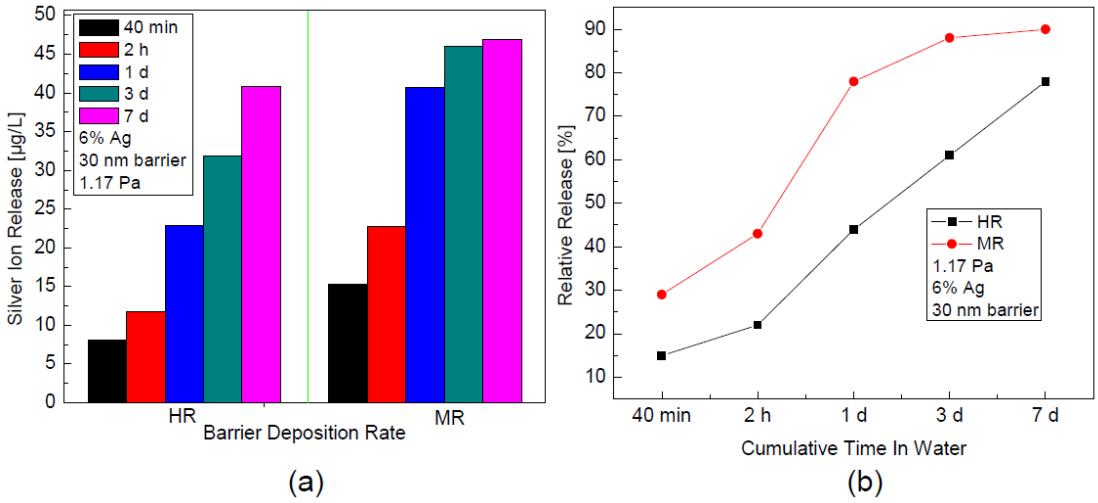

Figure 5.17 (a) The cumulative concentration of silver ion release and (b) % relative silver release to elapsed time. 6% Ag containing-nanocomposites with 30 nm barrier were produced at different barrier deposition rates at 1.17 Pa

5.2 Silver ion release property in 2D Ag/TiO_x nanocomposite thin films

To better understand the mechanism of silver ion release under different conditions, 2D model systems were prepared. A set of samples with a Ag nanoparticle layer of 2 nm nominal thickness deposited onto a 10 nm TiO_x buffer layer was produced at 1.17 Pa and 0.45 Pa. TiO_x capping layers with varying thickness were deposited on top with the same moderate rate (around 6 nm/min) as used for the TiO_x buffer layer. As shown in Figure 5.18, the samples coated with a 10-50 nm barrier thickness only present a slight decrease in the silver ion release rate compared with a film without a barrier, indicating a similar silver ion release behavior as shown by the 3D nanocomposites prepared at 1.17 Pa. This can be attributed to a large surface segregation effect occurring and the loose and porous structure of the TiO_x barrier layers.

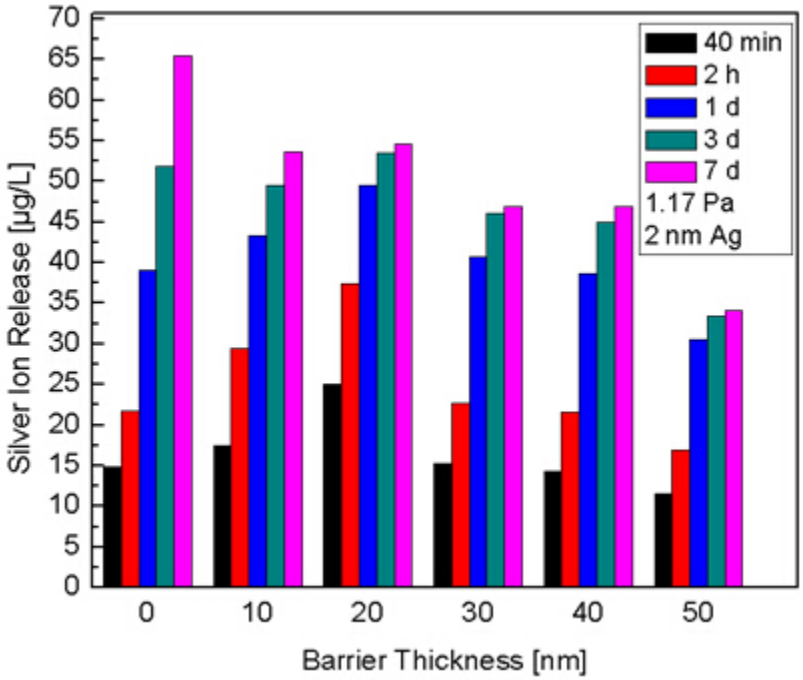

Figure 5.18 The cumulative concentration of silver ion release after certain elapsed times. 2 nm nominal Ag layer nanocomposites were produced with different barrier thickness at 1.17 Pa

However, the silver ion release rate shows a substantial decreasing tendency after coating barrier layers for the 2D nanocomposites when the total pressure was decreased to 0.45 Pa as depicted in Figure 5.19. The amounts of silver ion released for the samples coated with 10-30 nm were all reduced sharply and suppressed to a extremely low level, which is totally different from the similar samples prepared at high total pressure. It means a more dense and rigid TiO_x barrier layer could work very well for suppressing surface segregation and silver ion release.

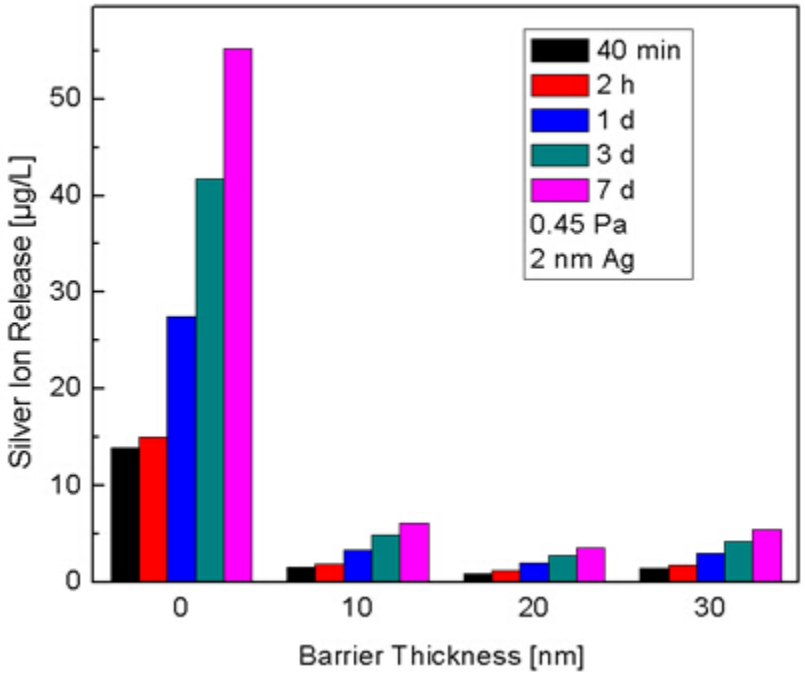

Figure 5.19 The cumulative concentration of silver ion release to elapsed time. 2 nm nominal Ag layer nanocomposites were produced with different barrier thickness at 0.45 Pa

Additionally, the influence of barrier deposition rate on the silver ion release rate at high total pressure was also investigated. 20 nm barriers with different deposition rates were deposited on 2 nm nominal silver layers which coated onto 10 nm TiO_x buffer layer. Figure 5.20 (a) shows the cumulative concentration of silver ions released during a 7 day releasing period. One can see that the total amount of released silver ions for the coatings prepared at different barrier deposition rates show no

difference after immersion for 7 days in water. The release behavior observed here is quite different during this period for these two different sets of samples. As shown in Figure 5.20 (b), the samples coated at a moderate barrier deposition rate only show a fast release in the initial stage, and nearly no release after 1 day in water, while the sample coated with a high deposition rate has a very slow but stable release during the whole period and still shows very high release potential after 7 days in water. This is consistent with the results observed for the 3D nanocomposite system. The more continuous film formed by larger nucleation rate at the high deposition rate suppressed the surface segregation and thus leads to a long-lasting release behavior.

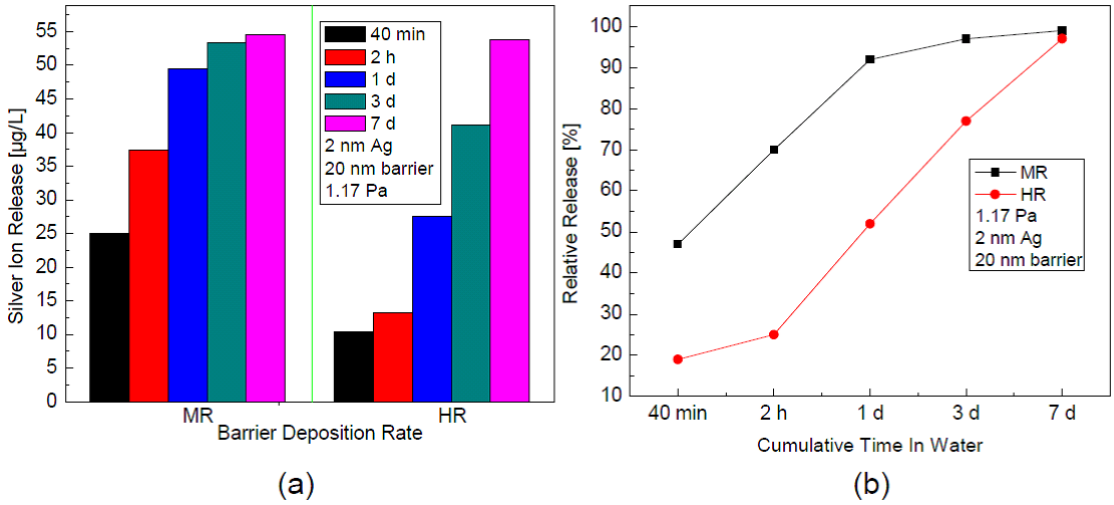

Figure 5.20 (a) The cumulative concentration of silver ion release and (b)% relative silver release to elapsed time. 2 nm Ag layer nanocomposites with 20 nm barriers were produced with different barrier deposition rates at 1.17 Pa

5.3 Conclusions

The silver ion release kinetics of 2D/3D silver/titania nanocomposite coatings were investigated. The morphology and microstructure of TiO_x matrixes and barriers were varied by adjusting the total gas pressure, oxygen flow rate, barrier deposition rate and thickness and the characteristic of silver NPs were varied as well.

It was observed that the silver ion release rate decreased as total gas pressure was reduced, and the 3D silver containing nanocomposite thin films prepared under 0.15 Pa present a lower but long-lasting stable release behavior. It was attributed to a reduction of the hydrophilic property by decreasing the total pressure. It was observed that at high total pressure the oxygen flow rate has little effect on the silver ion release, due to the large surface segregation effect and the more porous structure of titanium oxide produced at high total pressure.

Results showed that the silver ion release behavior has a significant change after varying the barrier deposition rate; a slower release at the initial stage but faster ion release can be achieved after that in both 2D and 3D structures. It is believed that the larger nuclei formation rate at higher deposition rates leads to a more continuous film which has a favorable suppressing effect for silver surface segregation, thus smaller silver NPs are formed inside the matrix and present a different release behavior.

More importantly, the difference in particle density change between the surface and bulk indicates that silver ions were released mainly from the bulk and not from the segregated Ag NPs on the surface. Smaller Ag NPs with larger surface area can facilitate faster dissolution and release of silver ions compared with bigger NPs segregating on the surface, thus inducing more silver ion release from the bulk. After immersion in water, some silver ions that desorbed from the smaller NPs in the bulk have a high probability to resorb onto the larger and more-stable spherical particles nearby, inducing Ostwald ripening on the surface.

In addition, the influence of the thickness of the barrier was also investigated here. The silver ion release could not be further reduced by increasing the barrier thickness due to the nature of the amorphous titanium oxide structure whose defects and voids lead to formation of pores allowing rapid transfer of water into the bulk. The channels formed on the surface by removing impurities in water could be another possible reason. Moreover, different silver ion release behavior is observed in a 7 day period. Nanocomposites produced under these conditions show a controllable and sufficiently high silver ion release for applications as antibacterial coatings.

Chapter 6

Summary and outlook

2D/3D Ag/TiO_x nanocomposites were prepared by reactive sputtering processes in home-made deposition chambers under high vacuum conditions. In 3D Ag/TiO_x nanocomposites system, the silver NPs were embedded into the titanium oxide matrix by a co-sputtering process at different concentrations in order to figure out their interfacial structure and surface evolution. For a better understanding of the silver mobility during the reactive sputtering process and subsequent changes of surface segregation and silver ion release properties, 2D Ag/TiO_x nanocomposites were developed. Morphology, chemical state, composition and silver ion release properties of 2D/3D Ag/TiO_x nanocomposites were studied. Various surface-sensitive characterization methods, such as SEM, XPS, XRD and TEM were intensively applied to the analysis of the nanocomposite coatings and the potential of the silver ion release of the coatings after exposure to water for different periods of time. AAS was used to measure the concentration of silver ions in water.

In chapter 4, different filling factors of silver were embedded into the titanium oxide matrix under varying total gas pressures and oxygen gas flow rates. Strong Ag segregation on the surface was observed everywhere due to the large stress associated with the embedding process. All the silver NPs presented a metallic state and fcc structure even if a high oxygen flow rate (19.2 sccm) was introduced. No silver oxide was detected. It is clearly evident that silver surface segregation can be hardly avoided even with the use of a barrier (60 nm) when a high total pressure (1.17 Pa) is used in the sputtering process. At high pressure the silver surface segregation can be only slightly reduced by the use of barrier layers. Under these conditions the silver segregation is influenced by the deposition rate used for the deposition of the barrier layers and is much reduced for higher deposition rates. An effective decrease of silver

surface segregation is only achieved when the total pressure during sputtering is reduced to 0.45 Pa or even 0.15 Pa. Here, the silver surface segregation can already be completely suppressed using a capping layer of 30 nm thickness. This is believed to be caused by a much more densely packed TiO_x layer formed at lower total sputtering pressure, whereas at higher total pressures, loose and porous TiO_x layers are always formed, facilitating the silver atoms fast diffusion onto the surface. In addition, elimination of the surface segregation by coating with a 50 nm barrier results in a much more homogenous size distribution of the silver NPs in the nanocomposite film giving rise to a much narrower plasmon absorption band with a blue shifted absorption peak maximum. A comparative study of 2D nanocomposite systems was also performed to study the mechanism of silver surface segregation. The results indicate that the Ag surface segregation is a plasma-assisted oxygen-induced process and occurs as soon as the sample is exposed to activated oxygen. These results indicated that the deposition conditions used for the preparation of reactively sputtered silver titania nanocomposite thin films have a strong influence on the surface segregation behavior of the silver and thus on the morphology of the thin films produced.

In chapter 5, the influence of sputter parameters on the surface morphology and subsequent silver ion release properties of reactively sputtered silver/TiO_x nanocomposites was investigated. Silver-containing titanium oxide nanocomposite coatings with tunable ion-release properties were successfully deposited by reactive sputtering at different total gas pressures of 0.15, 0.45 and 1.17 Pa. All of the silver NPs embedded in the nanocomposites were confirmed to be in a metallic state and have an fcc structure. The silver ion release property shows a clear tendency to decrease with reducing the total gas pressure during the deposition. Such dependence of the ion release behavior appears to be mainly correlated with the microstructure of the titanium oxide and the surface hydrophilic property, a more open and porous structure and more hydrophilic property, which allows an easier silver ion release for the coatings deposited at high total pressure. In addition, barriers can prevent silver ion release effectively to a extremely low rate especially for the samples prepared under low total pressures. However, increasing the barrier thickness does not show a

larger suppression of the silver release effect due to the nature of the amorphous titanium oxide matrix, where defects and void pores formed, facilitating rapid water transfer into the bulk and thus fast interaction with the silver NPs. Additionally, for the samples produced at high total pressure with high release potential in the initial stage, a more stable long-lasting silver release rate can be achieved by depositing barriers at a high rate in both 2D/3D nanocomposites. These results indicate that the Ag/TiO_x nanocomposites produced by the reactive sputtering process can be considered as promising antibacterial coatings with perfect silver ion release tuning effects.

Although surface segregation of silver in Ag/TiO_x nanocomposites has been observed regularly by many others, this phenomenon has not been investigated systematically. Here we show under which conditions of the reactive sputtering process silver surface segregation occurs and how it can be controlled to obtain silver/titania nanocomposites with a defined morphology. Moreover, the silver ion release property can be tailored by adjusting the deposition parameter and different silver ion release behavior can be achieved for short and long term use.

However, the changes in the silver ion release properties of the 2D/3D nanocomposites resulting from the changes of barrier thickness is an interesting point to investigate not only by using SEM and TEM but also by using electrochemical impedance spectroscopy (EIS), where the capacitance change of the thin films together with water uptake can be estimated at high frequency values.

The antibacterial ability and biocompatibility of the Ag/ TiO_x nanocomposite coatings should be studied for their real use in the medical field as biomaterials. Considering that our silver-release measurements were all performed in pure water, the silver ion release in other water-based solutions similar to blood and body fluids should be tested and thus more reliable data could be provided for long-term medical applications.

Additionally, since our samples can lock silver NPs in the bulk with extremely small silver release rates in the water, the Ag/ TiO_x nancomposite coatings can be further developed for the self-purification of waste water and enhanced photocatalyst use.

Bibliography

[1] Guo L, Yuan W, Lu Z and Li C M, "Polymer/nanosilver composite coatings for antibacterial applications," *Colloids and Surfaces A: Physicochemical and Engineering Aspects*, 439, 69–83 (**2013**)

[2] Mauter M S, Wang Y, Okemgbo K C, Osuji C O, Giannelis E P and Elimelech M, "Antifouling ultrafiltration membranes via post-fabrication grafting of biocidal nanomaterials," *ACS applied materials & interfaces*, 3, 2861–8 (**2011**)

[3] Eby D M, Luckarift H R and Johnson G R, "Hybrid antimicrobial enzyme and silver nanoparticle coatings for medical instruments," *ACS applied materials & interfaces*, 1, 1553–60 (**2009**)

[4] Page K, Palgrave R G, Parkin I P, Wilson M, Savin S L P and Chadwick A V, "Titania and silver-titania composite films on glass-potent antimicrobial coatings," *Journal of Materials Chemistry*, 17, 95 (**2007**)

[5] Cao H, Liu X, Meng F and Chu P K, "Biological actions of silver nanoparticles embedded in titanium controlled by micro-galvanic effects," *Biomaterials*, 32, 693–705 (**2011**)

[6] Adochite R C, Munteanu D, Torrell M, Cunha L, Alves E, Barradas N P, Cavaleiro a., Riviere J P, Le Bourhis E, Eyidi D and Vaz F, "The influence of annealing treatments on the properties of Ag:TiO_2 nanocomposite films prepared by magnetron sputtering," *Applied Surface Science*, 258, 4028–34 (**2012**)

[7] Ye G-X, Michely T, Weidenhof V, Friedrich I and Wuttig M, "Nucleation, Growth, and Aggregation of Ag Clusters on Liquid Surfaces," *Physical Review Letters*, 81, 622–5 (**1998**)

[8] Kibis L S, Stadnichenko a. I, Pajetnov E M, Koscheev S V, Zaykovskii V I and Boronin A I, "The investigation of oxidized silver nanoparticles prepared by thermal evaporation and radio-frequency sputtering of metallic silver under oxygen," *Applied Surface Science*, 257, 404–13 (**2010**)

[9] Armelao L, Barreca D, Bottaro G, Gasparotto A, Gross S, Maragno C and Tondello E, "Recent trends on nanocomposites based on Cu , Ag and Au clusters : A closer look," *Coordination Chemistry Reviews*, 250, 1294–314 (**2006**)

[10] Perkas N, Lipovsky A, Amirian G, Nitzan Y and Gedanken A, "Biocidal properties of TiO_2 powder modified with Ag nanoparticles," *Journal of Materials Chemistry B*, 1, 5309–16 (**2013**)

[11] Sellappan R, Nielsen M G, González-Posada F, Vesborg P C K, Chorkendorff I and Chakarov D, "Effects of plasmon excitation on photocatalytic activity of Ag/TiO_2 and Au/TiO_2 nanocomposites," *Journal of Catalysis*, 307, 214–21 (**2013**)

[12] Liu X, Liu Z, Lu J, Wu X, Xu B and Chu W, "Electrodeposition preparation of Ag nanoparticles loaded TiO_2 nanotube arrays with enhanced photocatalytic performance," *Applied Surface Science*, 288, 513–7 (**2014**)

[13] Khan M M, Ansari S A, Lee J and Cho M H, "Novel $Ag@TiO_2$ nanocomposite synthesized by electrochemically active biofilm for nonenzymatic hydrogen peroxide sensor," *Materials Science & Engineering C: Materials for biological applications*, 33, 4692–9 (**2013**)

[14] Lu Q, Lu Z, Lu Y, Lv L, Ning Y, Yu H, Hou Y and Yin Y, "Photocatalytic synthesis and photovoltaic application of $Ag\text{-}TiO_2$ nanorod composites," *Nano letters*, 13, 5698–702 (**2013**)

[15] Tan B and Wu Y, "Dye-sensitized solar cells based on anatase TiO_2 nanoparticle/nanowire composites," *The journal of physical chemistry B*, 110, 15932–8 (**2006**)

[16] Zhang W, Zhu S, Li Y and Wang F, "Photocatalytic Property of TiO_2 Films Deposited by Pulse DC Magnetron Sputtering," *Journal of Materials Science & Technology*, 20, 31–4 (**2004**)

[17] Chun H, Park S, You S, Kang G, Bae W, Kim K, Park J, Öztürk A and Shin D, "Preparation of a transparent hydrophilic TiO_2 thin film photocatalyst," *Journal of Ceramic Processing Research*, 10, 219–23 (**2009**)

[18] Lo C and Wu J C S, "Preparation and Characterization of TiO_2 -Coated Optical-Fiber in a Photo Reactor," *Journal of the Chinese Institute of Chemical Engineers*, 36, 119–25 (**2005**)

[19] Jeong S, Kim B, Lee B and Kim J, "Structural and Optical Properties of TiO_2 Films Prepared Using Reactive RF Magnetron Sputtering," *Journal of the Korean Physical Society*, 41, 67–72 (**2002**)

[20] Onifade A. and Kelly P J, "The influence of deposition parameters on the structure and properties of magnetron-sputtered titania coatings," *Thin Solid Films*, 494, 8–12 (**2006**)

[21] Pfaff G and Reynders P, "Angle-Dependent Optical Effects Deriving from Submicron Structures of Films and Pigments," *Chemical reviews*, 99, 1963–82 (**1999**)

[22] Smijs T G and Pavel S, "Titanium dioxide and zinc oxide nanoparticles in sunscreens : focus on their safety and effectiveness," *Nanotechnology Science and Applications*, 4, 95–112 (**2011**)

[23] Zallen R and Moret M P, "The optical absorption edge of brookite TiO_2," *Solid State Communications*, 137, 154–7 (**2006**)

[24] Park K J, Lee K U, Kim M H, Kwon O J and Kim J J, "Preparation of PS/TiO_2 as a white pigment for electrophoretic displays," *Current Applied Physics*, 13, 1231–6 (**2013**)

[25] Pawar S, "Fabrication of Nanocrystalline TiO_2 Thin Film Ammonia Vapor Sensor," *Journal of Sensor Technology*, 1, 9–16 (**2011**)

[26] Lu C-C, Huang Y-S, Huang J-W, Chang C-K and Wu S-P, "A macroporous TiO_2 oxygen sensor fabricated using anodic aluminium oxide as an etching mask," *Sensors*, 10, 670–83 (**2010**)

[27] Lee Y C, Hong Y P, Lee H Y, Kim H, Jung Y J, Ko K H, Jung H S and Hong K S, "Photocatalysis and hydrophilicity of doped TiO_2 thin films," *Journal of Colloid and Interface Science*, 267, 127–31 (**2003**)

[28] Hoang V V, Zung H and Trong N H B, "Structural properties of amorphous TiO_2 nanoparticles" *The European Physical Journal D*, 44, 515–24 (**2007**)

[29] Wang C-C, Yu C-Y, Kei C-C, Lee C-T and Perng T-P, "The formation of TiO_2 nanowires directly from nanoparticles," *Nanotechnology*, 20, 285601 (**2009**)

[30] Lu X, Wang G, Zhai T, Yu M, Gan J, Tong Y and Li Y, "Hydrogenated TiO_2 nanotube arrays for supercapacitors," *Nano letters*, 12, 1690–6 (**2012**)

[31] Yoo D, Kim I, Kim S, Hahn C H, Lee C and Cho S, "Effects of annealing temperature and method on structural and optical properties of TiO_2 films prepared by RF magnetron sputtering at room temperature," *Applied Surface Science*, 253, 3888–92 (**2007**)

[32] Zhao Z W and Tay B K, "Study of nanocrystal TiO_2 thin films by thermal annealing," *Journal of Electroceramics*, 16, 489–93 (**2006**)

[33] Hasan M M, Haseeb A S M A, Saidur R and Masjuki H H, "Effects of Annealing Treatment on Optical Properties of Anatase TiO_2 Thin Films," *International Journal of Chemical and Biological Engineering*, 1, 92–6 (**2008**)

[34] Yang G-J, Li C-J, Han F and Huang X-C, "Effects of annealing treatment on microstructure and photocatalytic performance of nanostructured TiO_2 coatings through flame spraying with liquid feedstocks," *Journal of Vacuum Science & Technology B: Microelectronics and Nanometer Structures*, 22, 2364 (**2004**)

[35] Borghols W J H, Lützenkirchen-Hecht D, Haake U, Chan W, Lafont U, Kelder E M, Van Eck E R H, Kentgens A P M, Mulder F M and Wagemaker M, "Lithium Storage in Amorphous TiO_2 Nanoparticles," *Journal of The Electrochemical Society*, 157, 582–8 (**2010**)

[36] Gao Y, Masuda Y and Koumoto K, "Light-excited superhydrophilicity of amorphous TiO_2 thin films deposited in an aqueous peroxotitanate solution," *Langmuir*, 20, 3188–94 (**2004**)

[37] Kakuta N, Oku T, Suzuki A, Kikuchi K and Kikuchi S, "Processing Research Effect of an amorphous TiO_2 addition on dye-sensitized solar cells with organic dyes," *Journal of Ceramic Processing Research*, 13, 28–31 (**2012**)

[38] Lee W G, Woo S I, Kim J C, Choi S H and Oh K H, "Preparation and properties of amorphous TiO_2 thin films by plasma enhanced chemical vapor deposition," *Thin Solid Films*, 237, 105–11 (**1994**)

[39] Lu H F, Li F, Liu G, Chen Z-G, Wang D-W, Fang H-T, Lu G Q, Jiang Z H and Cheng H-M, "Amorphous TiO_2 nanotube arrays for low-temperature oxygen sensors," *Nanotechnology*, 19, 405504 (**2008**)

[40] Shih W S, Young S J, Ji L W, Water W and Shiu H W, "TiO_2-Based Thin Film Transistors with Amorphous and Anatase Channel Layer," *Journal of The Electrochemical Society*, 158, 609–11 (**2011**)

[41] Prasai B, Cai B, Underwood M K, Lewis J P and Drabold D A, "Properties of amorphous and crystalline titanium dioxide from first principles," *Journal of Materials Science*, 47, 7515–21 (**2012**)

[42] Chao S, Wang W, Hsu M and Wang L, "Characteristics of ion-beam-sputtered high- refractive-index TiO_2 -SiO_2 mixed films," *Journal of the Optical Society of America A*, 16, 1477–83 (**1999**)

[43] Ozasa K, Nemoto S, Li Y, Hara M, Maeda M and Mochitate K, "Contact angle and biocompatibility of sol-gel prepared TiO_2 thin films for their use as semiconductor-based cell-viability sensors," *Surface and Interface Analysis*, 40, 579–83 (**2008**)

[44] Kajitvichyanukul P, Ananpattarachai J and Pongpom S, "Sol-gel preparation and properties study of TiO_2 thin film for photocatalytic reduction of

chromium (VI) in photocatalysis process," *Science and Technology of Advanced Materials*, 6, 352–8 (**2005**)

[45] Wen T, Gao J and Shen J, "Preparation and characterization of TiO_2 thin films by the sol-gel process," *Journal of Materials Science*, 6, 5923–6 (**2001**)

[46] Guo B, Liu Z, Hong L and Jiang H, "Sol-gel derived photocatalytic porous TiO_2 thin films," *Surface & Coatings Technology*, 198, 24–9 (**2005**)

[47] Besserguenev V G, Pereira R J F, Mateus M C, Khmelinskii I V, Nicula R C and Burkel E, "TiO_2 thin film synthesis from complex precursors by CVD: its physical and photocatalytic properties," *International Journal of Photoenergy*, 5, 99–105 (**2003**)

[48] Masuda Y, Jinbo Y and Koumoto K, "Room Temperature CVD of TiO_2 Thin Films and Their Electronic Properties," *Science of Advanced Materials*, 1, 138–43 (**2009**)

[49] Romero L and Binions R, "Effect of AC electric fields on the aerosol assisted chemical vapour deposition growth of titanium dioxide thin films," *Surface and Coatings Technology*, 230, 196–201 (**2013**)

[50] Kitano M, Mitsui R, Eddy D R, El-Bahy Z M A, Matsuoka M, Ueshima M and Anpo M, "Synthesis of Nanowire TiO_2 Thin Films by Hydrothermal Treatment and their Photoelectrochemical Properties," *Catalysis Letters*, 119, 217–21 (**2007**)

[51] Zhang S, Wen W, Jiang D, Zhao H, John R, Wilson G J and Will G D, "Photoelectrochemical characterisation of TiO_2 thin films derived from microwave hydrothermally processed nanocrystalline colloids," *Journal of Photochemistry and Photobiology A: Chemistry*, 179, 305–13 (**2006**)

[52] Vernardou D, Stratakis E, Kenanakis G, Yates H M, Couris S, Pemble M E, Koudoumas E and Katsarakis N, "One pot direct hydrothermal growth of photoactive TiO_2 films on glass," *Journal of Photochemistry and Photobiology A: Chemistry*, 202, 81–5 (**2009**)

[53] Moret M P, Zallen R, Vijay D P and Desu S B, "Brookite-rich titania flms made by pulsed laser deposition," *Thin Solid Films*, 366, 8–10 (**2000**)

[54] Liu X, Yin J, Liu Z G, Yin X B, Chen G X and Wang M, "Structural characterization of TiO_2 thin flms prepared by pulsed laser deposition on GaAs (1 0 0) substrates," *Applied Surface Science*, 174, 35–9 (**2001**)

[55] Choi G, Kim S K, Won S, Kim H J and Hwang C S, "Plasma-Enhanced Atomic Layer Deposition of TiO_2 and Al-Doped TiO_2 Films Using N_2 and O_2 Reactants," *Journal of The Electrochemical Society*, 156, 138–43 (**2009**)

[56] Aarik J, Aidla A, Uustare T and Kukli K, "Atomic layer deposition of TiO_2 thin films from TiI_4 and H_2O," *Applied Surface Science*, 193, 277–86 (**2002**)

[57] Kim Y and Kim D, "Atomic layer deposition of TiO_2 from tetrakis-dimethylamido-titanium and ozone," *Korean Journal of Chemical Engineering*, 29, 969–73 (**2012**)

[58] Ye Q, Liu P Y A, Tang Z F and Zhai L, "Hydrophilic properties of nano-TiO_2 thin films deposited by RF magnetron sputtering," *Vacuum*, 81, 627–31 (**2007**)

[59] Tanemura S, Miao L, Wunderlich W, Tanemura M, Mori Y, Toh S and Kaneko K, "Fabrication and characterization of anatase/rutile–TiO_2 thin films by magnetron sputtering: a review," *Science and Technology of Advanced Materials*, 6, 11–7 (**2005**)

[60] Boyadzhiev S, Georgieva V and Rassovska M, "Characterization of reactive sputtered TiO_2 thin films for gas sensor applications," *Journal of Physics: Conference Series*, 253, 012040 (**2010**)

[61] Zhang W, Li Y and Wang F, "Properites of TiO_2 Thin Films Prepared by Magnetron sputtering," *Journal of Materials Science and Technology*, 18, 101–7 (**2002**)

[62] Mohamed S H, Kappertz O, Leervad Pedersen T P, Drese R and Wuttig M, "Properties of TiO_x coatings prepared by dc magnetron sputtering," *Physica Status Solidi A*, 198, 224–37 (**2003**)

[63] Lrbl P, Huppertz M and Mergel D, "Nucleation and growth in TiO_2 films prepared by sputtering and evaporation," *Thin Solid Films*, 251, 72–9 (**1994**)

[64] Buranawong A, Witit-Anun N and Chaiyakun S, "Total Pressure and Annealing Temperature Effects on Structure and Photo-Induce Hydrophilicity of Reactive DC Sputtered TiO_2 Thin Films," *Engineering Journal*, 16, 79–90 (**2012**)

[65] Yamagishi M, "Thin film TiO_2 photocatalyst deposited by reactive magnetron sputtering," *Thin Solid Films*, 442, 227–31 (**2003**)

[66] Caballero A, Leinen D, Fernández A, Justo A, Espinós J P and González-Elipe A R, "Contribution of the x-ray absorption spectroscopy to study TiO_2 thin films prepared by ion beam induced chemical vapor deposition," *Journal of Applied Physics*, 77, 591–7 (**1995**)

[67] Vancoppenolle V, Jouan P-Y, Wautelet M, Dauchot J-P and Hecq M, "Glow discharge mass spectrometry study of the deposition of TiO_2 thin films by direct current reactive magnetron sputtering of a Ti target," *Journal of Vacuum Science & Technology A: Vacuum, Surfaces, and Films*, 17, 3317–21 (**1999**)

[68] Gouttebaron R, Cornelissen D, Snyders R, Dauchot J P, Wautelet M and Hecq M, "XPS study of TiO_x thin films prepared by d . c . magnetron sputtering in $Ar – O_2$ gas mixtures," *Surface And Interface Analysis*, 530, 527–30 (**2000**)

[69] Wang H, Wang T and Xu P, "Effects of substrate temperature on the microstructure and photocatalytic reactivity of TiO_2 films," *Journal of Materials Science: Materials in Electronics*, 9, 327–30 (**1998**)

[70] Peng T, Xiao X, Ren F, Xu J, Zhou X, Mei F and Jiang C, "Influence of annealing temperature on the properties of TiO_2 films annealed by ex situ and in situ TEM," *Journal of Wuhan University of Technology-Mater. Sci. Ed*, 27, 1014–9 (**2012**)

[71] Matsumoto Y, "Room-Temperature Ferromagnetism in Transparent Transition Metal-Doped Titanium Dioxide," *Science*, 291, 854–6 (**2001**)

[72] Piszczek P, Muchewicz Ż, Radtke A, Gryglas M, Dahm H and Różycki H, "CVD of TiO_2 and TiO_2/Ag antimicrobial layers: Deposition from the hexanuclear μ-oxo Ti(IV) complex as a precursor and the characterization," *Surface and Coatings Technology*, 222, 38–43 (**2013**)

[73] Gao Y, Fang P, Chen F, Liu Y, Liu Z, Wang D and Dai Y, "Enhancement of stability of N-doped TiO_2 photocatalysts with Ag loading," *Applied Surface Science*, 265, 796–801 (**2013**)

[74] Feng N, Wang Q, Zheng A, Zhang Z, Fan J, Liu S-B, Amoureux J-P and Deng F, "Understanding the high photocatalytic activity of (B, Ag)-codoped TiO_2 under solar-light irradiation with XPS, solid-state NMR, and DFT calculations,"*Journal of the American Chemical Society*, 135, 1607–16 (**2013**)

[75] Li G, Wang T, Zhu Y, Zhang S, Mao C, Wu J, Jin B and Tian Y, "Preparation and photoelectrochemical performance of Ag/graphene/TiO_2 composite film," *Applied Surface Science*, 257, 6568–72 (**2011**)

[76] Tomás S a., Luna-Resendis a., Cortés-Cuautli L C and Jacinto D, "Optical and morphological characterization of photocatalytic TiO_2 thin films doped with silver," *Thin Solid Films*, 518, 1337–40 (**2009**)

[77] Zhang F, Wolf G K, Wang X and Liu X, "Surface properties of silver doped titanium oxide films," *Surface and Coatings Technology*, 148, 65–70 (**2001**)

[78] Akhavan O, "Lasting antibacterial activities of Ag-TiO_2/Ag/a-TiO_2 nanocomposite thin film photocatalysts under solar light irradiation. *Journal of colloid and interface science*, 336, 117–24 (**2009**)

[79] Sun S, Sun B, Zhang W and Wang D, "Preparation and antibacterial activity of Ag – TiO_2 composite film by liquid phase deposition (LPD) method," *Bulletin of Materials Science*, 31, 61–6 (**2008**)

[80] Chang Y, Lai C and Hsu J, "Antibacterial properties and human gingival fibroblast cell compatibility of TiO_2 / Ag compound coatings and ZnO films on titanium-based material," *Clinical Oral Investigations*, 16, 95–100 (**2011**)

[81] Balachandran Y L, Girija S, Selvakumar R, Tongpim S, Gutleb A C and Suriyanarayanan S, "Differently environment stable bio-silver nanoparticles: study on their optical enhancing and antibacterial properties," *PloS One*, 8, e77043 (**2013**)

[82] Droghetti E, Nicoletti F P, Guandalini L, Bartolucci G and Smulevich G, "SERS detection of benzophenones on viologen functionalized Ag nanoparticles: application to breakfast cereals," *Journal of Raman Spectroscopy*, 44, 1428–34 (**2013**)

[83] Haes A J and Van Duyne R P, "A nanoscale optical biosensor: sensitivity and selectivity of an approach based on the localized surface plasmon resonance spectroscopy of triangular silver nanoparticles," *Journal of the American Chemical Society*, 124, 10596–604 (**2002**)

[84] Ashokkumar S, Ravi S and Velmurugan S, "Green synthesis of silver nanoparticles from Gloriosa superba L. leaf extract and their catalytic activity," *Spectrochimica acta. Part A, Molecular and biomolecular spectroscopy*, 115, 388–92 (**2013**)

[85] Awasthi K K, Awasthi A, Kumar N, Roy P, Awasthi K and John P J, "Silver nanoparticle induced cytotoxicity, oxidative stress, and DNA damage in CHO cells," *Journal of Nanoparticle Research*, 15, 1898 (**2013**)

[86] Rivero P J, Urrutia a., Goicoechea J, Matias I R and Arregui F J, "A Lossy Mode Resonance optical sensor using silver nanoparticles-loaded films for monitoring human breathing," *Sensors and Actuators B: Chemical*, 187, 40–4 (**2013**)

[87] Prasad R Y, McGee J K, Killius M G, Suarez D a, Blackman C F, DeMarini D M and Simmons S O, "Investigating oxidative stress and inflammatory responses elicited by silver nanoparticles using high-throughput reporter genes in $HepG_2$ cells: effect of size, surface coating and intracellular uptake," *Toxicology in vitro*, 27, 2013–21 (**2013**)

[88] Mirgorod Y a. and Borodina V G, "Preparation and bactericidal properties of silver nanoparticles in aqueous tea leaf extract," *Inorganic Materials*, 49, 980–3 (**2013**)

[89] Roe D, Karandikar B, Bonn-Savage N, Gibbins B and Roullet J-B, "Antimicrobial surface functionalization of plastic catheters by silver nanoparticles," *The Journal of antimicrobial chemotherapy*, 61, 869–76 (**2008**)

[90] Chen C-Y and Chiang C-L, "Preparation of cotton fibers with antibacterial silver nanoparticles," *Materials Letters*, 62, 3607–9 (**2008**)

[91] Liu J and Hurt R H, "Ion Release Kinetics and Particle Persistence in Aqueous Nano-Silver Colloids," *Environmental science & technology*, 44, 2169–75 (**2010**)

[92] Alissawi N, "*Ion release from silver / polymer nanocomposites,"* (**2013**)

[93] Behra R, Sigg L, Clift M J D, Herzog F, Minghetti M, Johnston B, Rothen-rutishauser B and Petri-fink A, "Bioavailability of silver nanoparticles and ions : from a chemical and biochemical perspective," *Journal of the Royal Society Interface*, 10, 20130396 (**2013**)

[94] Dobias J and Bernier-Latmani R, "Silver release from silver nanoparticles in natural waters," *Environmental science & technology*, 47, 4140–6 (**2013**)

[95] Choi O and Hu Z, "Size dependent and reactive oxygen species related nanosilver toxicity to nitrifying bacteria," *Environmental science & technology*, 42, 4583–8 (**2008**)

[96] Mudunkotuwa I a and Grassian V H. "The devil is in the details (or the surface): impact of surface structure and surface energetics on understanding the behavior of nanomaterials in the environment," *Journal of environmental monitoring*, 13, 1135–44 (**2011**)

[97] Raimondi F, Scherer G G, Kötz R and Wokaun A, "Nanoparticles in energy technology: examples from electrochemistry and catalysis," *Angewandte Chemie (International ed. in English)*, 44, 2190–209 (**2005**)

[98] Yang X, Gondikas A P, Marinakos S M, Auffan M, Liu J, Hsu-Kim H and Meyer J N, "Mechanism of silver nanoparticle toxicity is dependent on dissolved silver and surface coating in Caenorhabditis elegans," *Environmental science & technology*, 46, 1119–27 (**2012**)

[99] Yen H-J, Hsu S-H and Tsai C-L, "Cytotoxicity and immunological response of gold and silver nanoparticles of different sizes," *Small*, 5, 1553–61 (**2009**)

[100] Morones J R, Elechiguerra J L, Camacho A, Holt K, Kouri J B, Ramírez J T and Yacaman M J, "The bactericidal effect of silver nanoparticles," *Nanotechnology*, 16, 2346–53 (**2005**)

[101] Ma R, Levard C, Marinakos S M, Cheng Y, Liu J, Michel F M, Brown G E and Lowry G V, "Size-controlled dissolution of organic-coated silver nanoparticles," *Environmental science & technology*, 46, 752–9 (**2012**)

[102] Samoilova N a., Blagodatskikh I V., Kurskaya E a., Krayukhina M a., Vyshivannaya O V., Abramchuk S S, Askadskii a. a. and Yamskov I a, "Stabilization of silver nanoparticles with copolymers of maleic acid," *Colloid Journal*, 75, 409–20 (**2013**)

[103] Dong X, Ji X, Wu H, Zhao L, Li J and Yang W, "Shape Control of Silver Nanoparticles by Stepwise Citrate Reduction," *The Journal of Physical Chemistry C*, 113, 6573–6 (**2009**)

[104] Tejamaya M, Römer I, Merrifield R C and Lead J R, "Stability of citrate, PVP, and PEG coated silver nanoparticles in ecotoxicology media," *Environmental science & technology*, 46, 7011–7 (**2012**)

[105] Suresh A K, Pelletier D a, Wang W, Morrell-Falvey J L, Gu B and Doktycz M J, "Cytotoxicity induced by engineered silver nanocrystallites is dependent on surface coatings and cell types," *Langmuir*, 28, 2727–35 (**2012**)

[106] Chappell M A, Miller L F, George A J, Pettway B a, Price C L, Porter B E, Bednar A J, Seiter J M, Kennedy A J and Steevens J A, "Simultaneous dispersion-dissolution behavior of concentrated silver nanoparticle suspensions in the presence of model organic solutes," *Chemosphere*, 84, 1108–16 (**2011**)

[107] Navarro E, Piccapietra F, Wagner B, Marconi F, Kaegi R, Odzak N, Sigg L and Behra R, "Toxicity of silver nanoparticles to Chlamydomonas reinhardtii," *Environmental science & technology*, 42, 8959–64 (**2008**)

[108] Lowry G V, Gregory K B, Apte S C and Lead J R, "Guest comment: Transformations of nanomaterials in the environment focus issue," *Environmental science & technology*, 46, 6891–2 (**2012**)

[109] Piccapietra F, Allué C G, Sigg L and Behra R, "Intracellular silver accumulation in Chlamydomonas reinhardtii upon exposure to carbonate coated silver nanoparticles and silver nitrate," *Environmental science & technology*, 46, 7390–7 (**2012**)

[110] Liu J and Hurt R H, "Ion release kinetics and particle persistence in aqueous nano-silver colloids," *Environmental science & technology*, 44, 2169–75 (**2010**)

[111] Kittler S, Greulich C, Diendorf J, Köller M and Epple M, "Toxicity of Silver Nanoparticles Increases during Storage Because of Slow Dissolution under Release of Silver Ions," *Chemistry of Materials*, 22, 4548–54 (**2010**)

[112] Liu J, Wang Z, Liu F D, Kane A B and Hurt R H, "Chemical transformations of nanosilver in biological environments," *ACS nano*, 6, 9887–99 (**2012**)

[113] Khan S S, Mukherjee A and Chandrasekaran N, "Impact of exopolysaccharides on the stability of silver nanoparticles in water," *Water research*, 45, 5184–90 (**2011**)

[114] Stebounova L V, Guio E and Grassian V H, "Silver nanoparticles in simulated biological media: a study of aggregation, sedimentation, and dissolution," *Journal of Nanoparticle Research*, 13, 233–44 (**2010**)

[115] Suresh A K, Pelletier D a, Wang W, Morrell-Falvey J L, Gu B and Doktycz M J, "Cytotoxicity induced by engineered silver nanocrystallites is dependent on surface coatings and cell types," *Langmuir*, 28, 2727–35 (**2012**)

[116] Liu J, Sonshine D a, Shervani S and Hurt R H, "Controlled release of biologically active silver from nanosilver surfaces," *ACS nano*, 4, 6903–13 (**2010**)

[117] Nowack B, Krug H F and Height M, "120 Years of Nanosilver History: Implications for Policy Makers," *Environmental science & technology*, 45, 1177–83 (**2011**)

[118] Gondikas A P, Morris A, Reinsch B C, Marinakos S M, Lowry G V and Hsu-kim H, "Cysteine-Induced Modi fi cations of Zero-valent Silver Nanomaterials: Implications for Particle Surface Chemistry, Aggregation, Dissolution, and Silver Speciation," *Environmental science & technology*, 46, 7037–45 (**2012**)

[119] Glover R D, Miller J M and Hutchison J E, "Generation of metal nanoparticles from silver and copper objects: nanoparticle dynamics on surfaces and potential sources of nanoparticles in the environment," *ACS nano*, 5, 8950–7 (**2011**)

[120] Blaser S a, Scheringer M, Macleod M and Hungerbühler K, "Estimation of cumulative aquatic exposure and risk due to silver: contribution of nano-functionalized plastics and textiles," *The Science of the total environment*, 390, 396–409 (**2008**)

[121] Chen X and Schluesener H J, "Nanosilver: a nanoproduct in medical application," *Toxicology letters*, 176, 1–12 (**2008**)

[122] You C, Han C, Wang X, Zheng Y, Li Q, Hu X and Sun H, "The progress of silver nanoparticles in the antibacterial mechanism, clinical application and cytotoxicity," *Molecular biology reports*, 39, 9193–201 (**2012**)

[123] Marambio-Jones C and Hoek E M V, "A review of the antibacterial effects of silver nanomaterials and potential implications for human health and the environment," *Journal of Nanoparticle Research*, 12, 1531–51 (**2010**)

[124] Braydich-Stolle L, Hussain S, Schlager J J and Hofmann M-C, "In vitro cytotoxicity of nanoparticles in mammalian germline stem cells," *Toxicological sciences*, 88, 412–9 (**2005**)

[125] Kvitek L, Panacek a, Prucek R, Soukupova J, Vanickova M, Kolar M and Zboril R, "Antibacterial activity and toxicity of silver – nanosilver versus ionic silver," *Journal of Physics: Conference Series*, 304, 012029 (**2011**)

[126] Egger S, Lehmann R P, Height M J, Loessner M J and Schuppler M, "Antimicrobial properties of a novel silver-silica nanocomposite material," *Applied and environmental microbiology*, 75, 2973–6 (**2009**)

[127] Song D-H, Uhm S-H, Lee S-B, Han J-G and Kim K-N, "Antimicrobial silver-containing titanium oxide nanocomposite coatings by a reactive magnetron sputtering," *Thin Solid Films*, 519, 7079–85 (**2011**)

[128] Akhavan O, "Lasting antibacterial activities of Ag-TiO_2/Ag/a-TiO_2 nanocomposite thin film photocatalysts under solar light irradiation," *Journal of colloid and interface science*, 336, 117–24 (**2009**)

[129] Wei M-J, Zhou J, Lu X, Zhu Y, Liu W, Lu L and Zhang L, "Diffusion of water molecules confined in slits of rutile TiO_2(110) and graphite(0001)," *Fluid Phase Equilibria*, 302, 316–20 (**2011**)

[130] Wei M-J, Zhang L, Lu L, Zhu Y, Gubbins K E and Lu X, "Molecular behavior of water in TiO_2 nano-slits with varying coverages of carbon: a molecular dynamics simulation study," *Physical chemistry chemical physics*, 14, 16536–43 (**2012**)

[131] Lee D, Cohen R E and Rubner M F, Antibacterial properties of Ag nanoparticle loaded multilayers and formation of magnetically directed antibacterial microparticles," *Langmuir*, 21, 9651–9 (**2005**)

[132] C. Rehren, M. Muhle, X. Bao, R. Schlögl G E , "The Interaction of Silver with Oxygen : An Inverstigation with Thermal Desorption and Photoelectron Spectroscopy," *Zeitschrift für Physikalische Chemie*, 52, 11–53 (**1991**)

[133] Chen Z Y, Liang D, Ma G, Frankel G S, Allen H C and Kelly R G, "Influence of UV irradiation and ozone on atmospheric corrosion of bare silver," *Corrosion Engineering, Science and Technology*, 45, 169–80 (**2010**)

[134] Rooij A De, "Exposure of Silver to Atomic Oxygen," *The European Corrosion Congress* (**2010**)

[135] Rooij A De, "The Oxidation of Silver by Atomic Oxygen," *ESA Journal*, 13, 363–82 (**1989**)

[136] Ivanova O S and Zamborini F P, "Size-dependent electrochemical oxidation of silver nanoparticles," *Journal of the American Chemical Society*, 132, 70–2 (**2010**)

[137] Park K, Lee D, Rai a, Mukherjee D and Zachariah M R, "Size-resolved kinetic measurements of aluminum nanoparticle oxidation with single particle mass spectrometry," *The journal of physical chemistry B*, 109, 7290–9 (**2005**)

[138] Qi H, Alexson D, Glembocki O and Prokes S M, "The effect of size and size distribution on the oxidation kinetics and plasmonics of nanoscale Ag particles," *Nanotechnology*, 21, 215706 (**2010**)

[139] Yang D-Q, Gillet J-N, Meunier M and Sacher E, "Room temperature oxidation kinetics of Si nanoparticles in air, determined by x-ray photoelectron spectroscopy," *Journal of Applied Physics*, 97, 024303 1–6 (**2005**)

[140] Lok C, Ho C, Chen R, He Q, Yu W, Sun H, "Silver nanoparticles : partial oxidation and antibacterial activities," *Journal of Biological Inorganic Chemistry*, 12, 527–34 (**2007**)

[141] Rai M, Yadav A and Gade A, "Silver nanoparticles as a new generation of antimicrobials," *Biotechnology advances*, 27, 76–83 (**2009**)

[142] Kvı L, Soukupova J, Vec R, Prucek R, Holecova M and Zbor R, "Effect of Surfactants and Polymers on Stability and Antibacterial Activity of Silver Nanoparticles (NPs)," *The Journal of Physical Chemistry C*, 112, 5825–34 (**2008**)

[143] Billaud P, Marhaba S, Grillet N, Cottancin E, Bonnet C, Lerm é J, Vialle J-L, Broyer M and Pellarin M, "Absolute optical extinction measurements of single nano-objects by spatial modulation spectroscopy using a white lamp," *The Review of scientific instruments*, 81, 043101 1–12 (**2010**)

[144] Yin Y, Li Z-Y, Zhong Z, Gates B, Xia Y and Venkateswaran S, "Synthesis and characterization of stable aqueous dispersions of silver nanoparticles through the Tollens process," *Journal of Materials Chemistry*, 12, 522–7 (**2002**)

[145] Erol M, Han Y, Stanley S K, Stafford C M, Du H and Sukhishvili S, "SERS not to be taken for granted in the presence of oxygen," *Journal of the American Chemical Society*, 131, 7480–1 (**2009**)

[146] Battie Y, Destouches N, Bois L, Chassagneux F, Tishchenko A, Boukenter A and Lyon C B, "Growth Mechanisms and Kinetics of Photoinduced Silver Nanoparticles in Mesostructured Hybrid Silica Films under UV and Visible Illumination," *The Journal of Physical Chemistry C*, 114, 8679–87 (**2010**)

[147] Li W, Seal S, Megan E, Ramsdell J, Scammon K, Lelong G, Lachal L and Richardson K A, "Physical and optical properties of sol-gel nano-silver doped silica film on glass substrate as a function of heat-treatment temperature," *Journal of Applied Physics*, 93, 9553–61 (**2003**)

[148] Bi H, Cai W, Kan C, Zhang L, Martin D and Träger F, "Optical study of redox process of Ag nanoparticles at high temperature," *Journal of Applied Physics*, 92, 7491–7 (**2002**)

[149] Bi H, Cai W, Zhang L, Martin D and Trager F, "Annealing-induced reversible change in optical absorption of Ag nanoparticles," *The Journal of Chemical Physics*, 81, 5222–4 (**2002**)

[150] Pal S and De G, "Reversible transformations of silver oxide and metallic silver nanoparticles inside SiO_2 films," *Materials Research Bulletin*, 44, 355–9 (**2009**)

[151] Cai W, Hofmeister H and Rainer T, "Surface effect on the size evolution of surface plasmon resonances of Ag and Au nanoparticles dispersed within mesoporous silica," *Physica E-low-dimensional Systems & Nanostructures*, 11, 339–44 (**2001**)

[152] Cai W, Zhang Y, Jia J and Zhang L, "Semiconducting optical properties of silver/silica mesoporous composite," *Applied Physics Letters*, 73, 2709 (**1998**)

[153] Grillet N, Manchon D, Cottancin E, Bertorelle F, Bonnet C, Broyer M, Lerme J, Pellarin M, Lyon U De, Lyon U and Spectrome L De, "Photo-Oxidation of Individual Silver Nanoparticles : A Real-Time Tracking of Optical and Morphological Changes," *The Journal of Physical Chemistry C*, 117, 2274–82 (**2013**)

[154] Ashkarran A, Iraji zad A, Ahadian M M and Hormozi Nezhad M R, "Stability, size and optical properties of colloidal silver nanoparticles prepared by electrical arc discharge in water," *The European Physical Journal Applied Physics*, 48, 10601 (**2009**)

[155] Baida H, Billaud P, Marhaba S, Christofilos D, Cottancin E, Crut a, Lermé J, Maioli P, Pellarin M, Broyer M, Del Fatti N, Vallée F, Sánchez-Iglesias a,

Pastoriza-Santos I and Liz-Marzán L M, "Quantitative determination of the size dependence of surface plasmon resonance damping in single Ag@SiO_2 nanoparticles," *Nano letters*, 9, 3463–9 (**2009**)

[156] Lai X, Clair T P S and Goodman D W, "Oxygen-induced morphological changes of Ag nanoclusters supported on TiO (110)," *Faraday Discussions*, 279–84 (**2000**)

[157] Zuo J, Keil P and Grundmeier G, "Synthesis and characterization of photochromic Ag-embedded TiO_2 nanocomposite thin films by non-reactive RF-magnetron sputter deposition," *Applied Surface Science*, 258, 7231–7 (**2012**)

[158] Ngaruiya J M, Kappertz O, Mohamed S H and Wuttig M, "Structure formation upon reactive direct current magnetron sputtering of transition metal oxide films," *Applied Physics Letters*, 85, 748–50 (**2004**)

[159] Okumu J, Köhl D, Sprafke a., Von Plessen G and Wuttig M, "Formation mechanism of noble metal nanoparticles in reactively sputtered TiO_2 films," *Journal of Applied Physics*, 108, 063529 (**2010**)

[160] Okumu J, Dahmen C, Sprafke a. N, Luysberg M, Von Plessen G and Wuttig M, "Photochromic silver nanoparticles fabricated by sputter deposition," *Journal of Applied Physics*, 97, 094305 (**2005**)

[161] Mráz S and Schneider J M, "Influence of the negative oxygen ions on the structure evolution of transition metal oxide thin films," *Journal of Applied Physics*, 100, 023503 (**2006**)

[162] Cao Z X, "Equilibrium segregation of sulfur to the free surface of single crystalline titanium," *Journal of Physics: Condensed Matter*, 13, 7923–35 (**2001**)

[163] Gibbs J W, "*The Collected Works of J. Willard Gibbs (Yale University Press, New Haven, Conn.),"* (**1948**)

[164] Harries D R and Marwick A D, "Non-Equilibrium Segregation in Metals and Alloys," *Phil. Trans. R. Soc. Lond. A*, 295, 197–207 (**1980**)

[165] Smith T, Sputter Cleaning and Etching of Crystal Surfaces (Ti,W,Si) Monitored by Auger Spectroscopy, Ellipsometry and Work Function Change *Surface Science*, 27, 45–59 (**1971**)

[166] Khan I, "Surface segregation in titanium as monitored by auger electron spectroscopy," *Surface Science*, 40, 723–7 (**1973**)

[167] Alonso M, "*Fundamental University Physics VOLUME II (London: Addison-Wesley),"* (**1973**)

[168] Cao Z X, "Equilibrium segregation of sulfur to the free surface of single crystalline titanium," *Journal of Physics: Condensed Matter*, 13, 7923–35 (**2001**)

[169] Erichsen J, Kanzow J, Schurmann U, Dolgner K, Gunther S K, Strunskus T, Zaporojtchenko V and Faupel F, "Investigation of the surface glass transition temperature by embedding of nobel metal nanoclusters into monodisperse polystyrenes*"Macromolecules, 37, 1831-38* (**2004**)

[170] Chakravadhanula V S K, Kübel C, Hrkac T, Zaporojtchenko V, Strunskus T, Faupel F and Kienle L, "Surface segregation in TiO_2-based nanocomposite thin films," *Nanotechnology*, 23, 495701 (**2012**)

[171] Koenig, H R, Maissel L, "Application of RF Discharges to Sputtering *IBM," Journal of Research and Development*, 14, 168 (**1970**)

[172] Este G, Westwoog W, "A quasi-direct-current sputtering technique for the deposition of dielectrics at enhanced rates," *Journal of Vacuum Science & Technology A: Vacuum, Surfaces, and Films*, 6, 1845–8 (**1988**)

[173] Furuya A and Hirono S, "Target magnetic-field effects on deposition rate in rf magnetron sputtering," *Journal of Applied Physics*, 68, 304–10 (**1990**)

[174] Penning F M, USA Paten 2 146, 0251(939) (**1935**)

[175] Mcleod P S and Hartsough L D, "High rate sputtering of aluminum for metallization of integrated circuits," *Journal of Vacuum Science and Technology*, 263-265, **(1977**)

[176] Waits R K, "Planar magnetron sputtering," *Journal of Vacuum Science and Technology*, 15, 179–87 (**1978**)

[177] Window B, "Charged particle fluxes from planar magnetron sputtering sources," *Journal of Vacuum Science & Technology A: Vacuum, Surfaces, and Films*, 4, 196–202 (**1986**)

[178] Window B, "Unbalanced dc magnetrons as sources of high ion fluxes," *Journal of Vacuum Science & Technology A: Vacuum, Surfaces, and Films*, 4, 453–6 (**1986**)

[179] Savvides N, "Unbalanced magnetron ion-assisted deposition and property modification of thin films," *Journal of Vacuum Science & Technology A: Vacuum, Surfaces, and Films*, 4, 504–8 (**1986**)

[180] Teer D G, "Technical Note: A Magnetron Sputter Ion-Plating System," *Surface and Coatings Technology*, 39, 565–71 (**1989**)

[181] Sproul W D, Rudnik P J, Graham M E and Rohde S L, "High rate reactive sputtering in an opposed cathode closed-field unbalanced magnetron sputtering system," *Surface and Coatings Technology*, 43-44, 270–8 (**1990**)

[182] Svadkovski I V, Golosov D A and Zavatskiy S M, "Characterisation parameters for unbalanced magnetron sputtering systems," *Vacuum*, 68, 283–90 (**2003**)

[183] Nyaiesh A R, "The Characteristics of A Planar Magnetron Operated at A High-Power Input," *Thin Solid Films*, 86, 267–77 (**1981**)

[184] Sproul W D, "High-rate reactive DC magnetron sputtering of oxide and nitride superlattice coatings," *Vacuum*, 51, 641–6 (**1998**)

[185] Howson R P, Jafer H A S A, "Substrate effects from an unbalanced magnetron," *Thin Solid Films*, 193/194, 127–37 (**1990**)

[186] Berg S and Nyberg T, "Fundamental understanding and modeling of reactive sputtering processes," *Thin Solid Films*, 476, 215–30 (**2005**)

[187] Sproul W D, Christie D J, Carter D C, Industries A E, Collins F, Berg S and Nyberg T, "Control of the Reactive Sputtering Process Using Two Reactive Gases," *46th Annual Technical Conference Proceedings*, pp 98–103 (**2003**)

[188] Schiller S, Heisig U, Steinfelder K, Strompfel J, Voigt R, Fendler R, Teschner G and Diego S, "On the investigation of d.c. plasmatron discharges by optical emission spectrometry," *Thin Solid Films*, 96, 235–40 (**1982**)

[189] Affinito J, "Mechanisms of voltage controlled, reactive, planar magnetron sputtering of Al in Ar/N_2 and Ar/O_2 atmospheres," *Journal of Vacuum Science & Technology A: Vacuum, Surfaces, and Films*, 2, 1275–84 (**1984**)

[190] Sproul W, Christie D and Carter D, "Control of reactive sputtering processes," *Thin Solid Films*, 491, 1–17 (**2005**)

[191] Lewis M A, Glocker D A, Jorne J, "Measurements of secondary electron emission in reactive sputtering of aluminum and titanium nitride," *Journal of Vacuum Science & Technology A: Vacuum, Surfaces, and Films*, 7, 1019–24 (**1989**)

[192] Solidfilms T, Okamoto A and Serikawa T, "Reactive Sputtering $Ar-N_2$ Mixture," *Thin Solid Films*, 137, 143–51 (**1986**)

[193] Nyberg T, Berg S, Helmersson U and Hartig K, "Eliminating the hysteresis effect for reactive sputtering processes," *Applied Physics Letters*, 86, 164106 (**2005**)

[194] Poelman H, Tomaszewski H, Poelman D, Depla D and De Gryse R, "Effect of the oxygen deficiency of ceramic TiO_{2-x} targets on the deposition of TiO_2 thin films by DC magnetron sputtering," *Surface and Interface Analysis*, 36, 1167–70 (**2004**)

[195] Sonoda T and Kato M, "Formation of Ti/O compositional gradient film on Ti–6Al–4V alloy by reactive DC sputtering," *Surface Science*, 402-404, 241–4 (**1998**)

[196] Fadley C, "Instrumentation for surface studies: XPS angular distributions," *Journal of Electron Spectroscopy and Related Phenomena*, 5, 725–54 (**1974**)

[197] Mouder J F, Stickle W F, Sobol P E and Bomben K D, "*Handbook of X-ray Photoelectron Spectroscopy,"* (**1992**)

[198] Suryanarayana C and Norton M G, "*X-Ray Diffraction: A Practical Approach,"* (**1998**)

[199] Alissawi N, Zaporojtchenko V, Strunskus T, Hrkac T, Kocabas I, Erkartal B, Chakravadhanula V S K, Kienle L, Grundmeier G, Garbe-Schönberg D and Faupel F, "Tuning of the ion release properties of silver nanoparticles buried under a hydrophobic polymer barrier," *Journal of Nanoparticle Research*, 14, 928 (**2012**)

[200] Padovani S, D'Acapito F, Cattaruzza E, De Lorenzi a., Gonella F, Mattei G, Maurizio C, Mazzoldi P, Montagna M, Ronchin S, Tosello C and Ferrari M, "Metal nanocluster formation in silica films prepared by rf-sputtering: an experimental study," *The European Physical Journal B - Condensed Matter*, 25, 11–7 (**2002**)

[201] Paital S R and Dahotre N B, "Calcium phosphate coatings for bio-implant applications: Materials, performance factors, and methodologies," *Materials Science and Engineering: Reports*, 66, 1–70 (**2009**)

[202] Kelly P J, Beevers C F, Henderson P S, Arnell R D, Bradley J W and Bäcker H, "A comparison of the properties of titanium-based films produced by pulsed and continuous DC magnetron sputtering," *Surface and Coatings Technology*, 174-175, 795–800 (**2003**)

[203] Zeman P and Takabayashi S, "Effect of total and oxygen partial pressures on structure of photocatalytic TiO_2 films sputtered on unheated substrate," *Surface & Coatings Technology*, 153, 93–9 (**2002**)

[204] D.R.Gaskell, "*Introduction To The Thermodynamics of Materials,"* (**2008**)

[205] Lai X, Clair T P S and Goodman D W, "Oxygen-induced morphological changes of Ag nanoclusters supported on TiO (110)," *Faraday Discuss.*, 114, 279–84 (**1999**)

[206] Okumu J, Köhl D, Sprafke A, Von Plessen G and Wuttig M, "Formation mechanism of noble metal nanoparticles in reactively sputtered TiO_2 films," *Journal of Applied Physics*, 108, 063529 (**2010**)

[207] Okumu J, Dahmen C, Sprafke a. N, Luysberg M, Von Plessen G and Wuttig M, "Photochromic silver nanoparticles fabricated by sputter deposition," *Journal of Applied Physics*, 97, 094305 (**2005**)

[208] Ngaruiya J M, Kappertz O, Mohamed S H and Wuttig M, "Structure formation upon reactive direct current magnetron sputtering of transition metal oxide films," *Applied Physics Letters*, 85, 748 (**2004**)

[209] Chakravadhanula V S K, Kübel C, Hrkac T, Zaporojtchenko V, Strunskus T, Faupel F and Kienle L, "Surface segregation in TiO_2-based nanocomposite thin films," *Nanotechnology*, 23, 495701 (**2012**)

[210] Hrkac T, Röhl C, Podschun R, Zaporojtchenko V, Strunskus T, Papavlassopoulos H, Garbe-Schönberg D and Faupel F, "Huge increase of therapeutic window at a bioactive silver/titania nanocomposite coating surface compared to solution," *Materials science & engineering. C*, 33, 2367–75 (**2013**)

[211] Ohring M, "*The Materials Science of Thin Films,"* (**1992**)

[212] Zuo J, Keil P and Grundmeier G, "Synthesis and characterization of photochromic Ag-embedded TiO_2 nanocomposite thin films by non-reactive RF-magnetron sputter deposition," *Applied Surface Science*, 258, 7231–7 (**2012**)

[213] Okumu J, Köhl D, Sprafke A, Von Plessen G and Wuttig M, "Formation mechanism of noble metal nanoparticles in reactively sputtered TiO_2 films," *Journal of Applied Physics*, 108, 063529 (**2010**)

[214] Romanyuk A and Oelhafen P, "Formation and electronic structure of TiO_2–Ag interface," *Solar Energy Materials and Solar Cells*, 91, 1051–4 (**2007**)

[215] Chaiyakun S, Buranawong a., Deelert T and Witit-anun N, "The Influence of Total and Oxygen Partial Pressures on Structure and Hydrophilic Property of TiO_2 Thin Films Deposited by Reactive DC Magnetron Sputtering," *Advanced Materials Research*, 55-57, 465–8 (**2008**)

[216] Buranawong A, Witit-Anun N and Chaiyakun S, "Total Pressure and Annealing Temperature Effects on Structure and Photo-Induce Hydrophilicity of Reactive DC Sputtered TiO_2 Thin Films," *Engineering Journal*, 16, 79–90 (**2012**)

[217] Gentry S T, Kendra S F and Bezpalko M W, "Ostwald Ripening in Metallic Nanoparticles: Stochastic Kinetics," *The Journal of Physical Chemistry C*, 115, 12736–41 (**2011**)